Electronic Thesis and Dissertation Repository

12-12-2017 2:30 PM

A Method for the Geometric Analysis of Rugose Coral Growth Ridges as Paleoenvironmental Indicators in the Middle Devonian Hungry Hollow Member of Widder Formation, Michigan Basin

Andrew Thomson
The University of Western Ontario

Supervisor
Tstujia, Cameron J.,
The University of Western Ontario Co-Supervisor
McCausland, Philip, J.A.,
The University of Western Ontario

Graduate Program in Geology
A thesis submitted in partial fulfillment of the requirements for the degree in Master of Science
© Andrew Thomson 2017

Abstract

Skeletons of Devonian rugose corals feature submillimetre-scale growth ridges on their outer surface (epitheca) that record the successive positions of the coral polyp during longitudinal corallite growth. Specimens of rugose corals Eridophyllum and Cystiphylloides from the Hungry Hollow Member of the Middle Devonian Widder Formation were sectioned longitudinally and imaged by SEM, and image processing techniques were applied to extract a line representing the epithecal surface. Local extrema found through peak detection allowed growth ridges to be represented as simplified triangles, so that geometric measurements (area, length) could be related to coral growth and analyzed in reference to possible paleoenvironmental cycles. This research has produced an objective method for the extraction of growth ridge data from a two-dimensional coral slice, although slice location was found to influence results. Results show potential sub-monthly bundles of ~15-17 ridges, not previously observed, which suggest a lunar/tidal influence on coral growth.

Keywords: Devonian, growth ridges, image processing, lunar periodicity, rugose coral

"You miss 100% of the shots you don't take.
- Wayne Gretzky
- Michael Scott"

- Andrew Thomson

Acknowledgements

Firstly, I could not have completed this thesis without the continued support of my supervisors, Dr. Cameron Tsujita and Phil McCausland. I am grateful to them for not giving up on me when it was seemingly one thing after another interfering with my progress. A few people's technical expertise was essential for the completion of this thesis: Steve Wood, UWO, for creating the coral thin sections, Dr. Andrew Nelson, of Sustainable Archaeology, UWO, for assistance with Micro-CT scanning, as well as Dr. Desmond Moser and Ivan Barker, of ZAPLab, UWO for performing the SEM imaging. James Hughes provided coding help, particularly during the image stitching and point grouping phases.

I am forever grateful to my family members who were always supportive and a positive influence on my life. I couldn't have done any of this without them; my grandparents for always helping out whenever needed; my Aunt Edna, who supported everything I did and ultimately provided me opportunites I'd never imagined possible; my sister, Torie for always being there when I needed her (and distracting me once in a while); and most importantly my Mom, has provided me with everything I have ever needed, always kept me safe, remained a positive role model no matter what, and always emphasized education – except for art, that is...

To all the friends I've made throughout my eight years at Western (Kienan, Sam, Lindsey, Chelsea, Krista, Joe, Simon, Freddie, Matea, James, Joelle, Lindsay, Shaun, Kendra, Sid, Ronan, Jacob, Mark, and Holly) as well as the friends that have put up with me even longer (TJ, Alex, and Lorilee) I thank you for keeping me entertained, dragging me out once in a while, and listening to me talk about cars and electronics for hours on end and glad that I made these life-long friendships.

I'd also like to specifically mention Sam, Lindsey, Chelsea, and Kienan for helping me through difficult times throughout school – I know it wasn't easy – without them, I'm not sure I would have made it through undergrad, let alone finish a Master's. Also, the ARL – you know who you are – for reminding me to take a video game break once in a while and that goats always climb trees...

I'm grateful that Buick decided to turbocharge and black-out a plain old Regal in the 80's – that car has provided me with so much enjoyment and wonderful source of relaxation throughout my time at Western.

Finally, it is important for me to acknowledge how far I've come, particularly over the last three years. My tibial plateau fracture in March 2015 – six months after beginning this thesis – threw a wrench into life as it was. It's been a long road, with two surgeries, long-term physio, and in general, interfering with my overall health. That, plus, other outside issues greatly impacted my life, many times I considered quitting grad school, but stuck with it – with everyone's support, of course – and finished. Looking back, I feel that these have positively impacted my outlook on life and in the end, am grateful that they happened when they did. I've learned so much about myself over these past three years and really started to work towards being the best I can be. I can finally say, for the first time in my life, I'm proud of everything I've accomplished. I'm finally in control and I'm only heading upward.

Contents

List of Figures

List of Tables

List of Appendices

Glossary of terms

Lunar day time for the Moon to rotate once on its own axis, as well as complete one orbit around Earth.

Solar day time for Earth to rotate once on its own axis; completion of one light-dark cycle. Number per year has decreased over geologic time due to tidal friction decreasing Earth's rotational energy.

Lunar month time from new Moon to new Moon. At new Moon, no moonlight is reflected; moonlight gradually increases as more of the Moon is visible, up to maximum light during full Moon at halfway point. Moonlight then decreases until it reaches zero during next new Moon phase.

Earth year time for Earth to complete one rotation around the Sun.

Epitheca sheet-like calcium carbonate 'skin', encloses the coral skeleton and records previous growth locations; changes in growth rate are reflected as changes in skeletal diameter

Epithecal edge line a cross-sectional view of the epitheca, the outer surface of the coral

Extrema local maxima and minima, found using peak detection methods applied to the epithecal edge line

Detected peak local maxima detected within epithecal edge line, representing local maximum polyp expansion and skeletal diameter.

Detected trough local minima detected within epithecal edge line, representing local maximum polyp constriction and skeletal diameter. Line represents coral resting state.

Detected ridge set of three consecutive detected trough-peak-trough points, representing an interval of growth where the polyp transitioned from maximum constriction, to maximum expansion, then returned to maximum constriction.

Ridge area area (μm^2) of a trough-peak-trough triangle representation of a growth ridge. A quantifiable measure of coral growth for a particular growth interval.

Ridge length distance (μm) from trough-trough, for a given ridge, beginning at and returning to maximum polyp constriction for a growth interval

Ridge height distance (μm) from peak to trough-trough centre point, for a given ridge, representing growth along the longitudinal axis for a given growth interval.

Ridge ratio Proportionality of ridge height to ridge length (ridge height / ridge length)

Base growth length length (μm) of line connecting all trough points, for a given image section. Records maximum coral polyp constriction for for growth intervals and may represent a continuous record of daily vertical growth

Epithecal length actual length (μm) of the epithecal edge line extracted from an image section

Growth ratio Total deviation from maximum constriction (trough-trough line), potentially representing growth from a polyp's daily resting state (base growth length / epithecal length)

Section length Total coral specimen SEM image length (mm).

Growth direction growth parallel to the longitudinal axis of the coral (upwards). Signified by an arrow in figures within this thesis

Chapter 1

Introduction

1.1   Purpose and scope of investigation

The fossil skeletons of Paleozoic rugose corals feature micron-scale growth ridges on their outer surface (epitheca) that record the successive positions of the coral polyp during longitudinal corallite growth. Epithecal ridges and intervening troughs represent short-term increases (radial polyp expansion) and decreases (radial polyp constriction) in polyp size (Barnes, 1972). These ridges have been claimed to show annual, lunar monthly, and daily growth cycles (Figure 1.1) (Scrutton, 1964; Wells, 1963). To date, research has been limited to counts of growth ridges within assumed annual growth cycles using optical microscopy. Counting by hand introduces human error, either by missing or double-counting ridges and little progress has been made with regards to the development of an automated process (Comboul et al., 2014).

In a review of Middle Devonian orbital patterns, Brosche and Sündermann (1978) noted that Earth's rotational speed was increased, leading to more rotations on its own axis during one solar orbit. This resulted in an increased number of shorter days per year (~396 vs. 365 today). Day length is inversely proportional to Earth's rotation rate. Rotational speed has con-

1
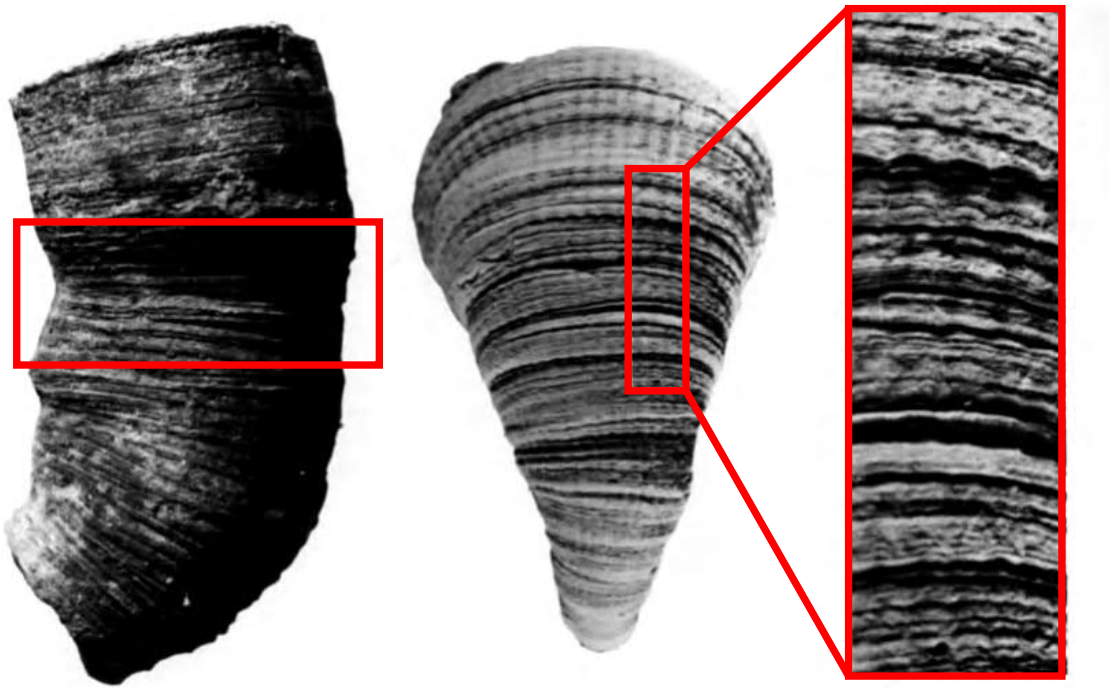
Figure 1.1: Composite figure showing scales of growth cycles preserved on the epitheca of a rugose coral, mofifdified after Scrutton (1978).

sistently decreased over time as Earth's energy dissipates through friction between ocean water and oceanic crust. The Moon was closer to Earth during this time as well, which resulted in more orbits (lunar months) around Earth per year (~13 vs 12) (Brosche and Sündermann, 1978).

The purpose of this study is to measure and find patterns within smaller subannual cycles. These patterns could help determine Devonian storm frequency, changes in coral growth conditions, and potentially detect astronomical cycles like Earth's rotation rate and tidal periodicity.

1.2   Rationale

Organisms, particularly those with carbonate components, have been used as indicators of paleoenvironment, typically as paleothermometers through isotopic analysis. Corals seem to show a cyclic growth pattern, as seen in growth ridges on the outer surface and density bands internally, which are believed to represent changes in annual, lunar monthly, and daily (tidal/diurnal) growth (Scrutton, 1964; Wells, 1963). As corals calcify quickly, they record paleoenvironmental changes at a higher resolution (daily) than other proxies such as ice cores or tree rings, with less averaging of values over time. They could provide a relative, daily complement to absolute dating methods (Jakubowicz et al., 2015; Wells, 1963). This thesis developed an objective, repeatable method for analyzing growth increments by:

1. Determining the environmental factors influencing coral growth rates in modern coral species, to use as possible analogues to fossil coral species.

2. Developing a method for measuring and quantifying the dimensions of coral growth ridges, relative to each other and to larger cycles.

3. Measuring, counting, and determining the cyclicity of growth ridges, relating such cycles, if detected, to paleoenvironmental and/or astronomical cycles.

1.3   Study area

Rugose coral specimens were collected by Dr. Cameron Tsujita from the Ausable River

outcrop of the Hungry Hollow Member of the Widder Formation (Middle Devonian Hamilton

Group) at quarry and riverbank exposures in Arkona, Ontario, approximately 50 kilometres

west of London, Ontario (Figure 1.2). A more comprehensive description of the study area

and its geological setting appears in Chapter 3.
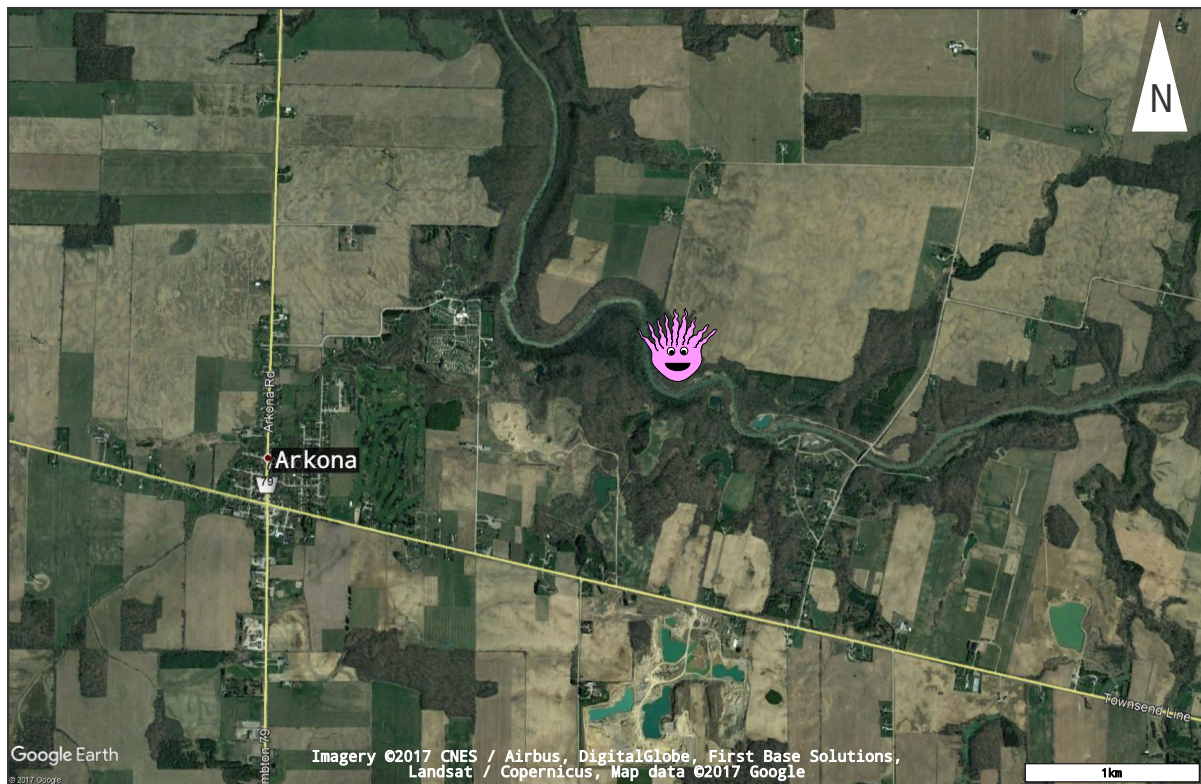
Figure 1.2: Satellite image of study area, with Ausable River outcrop collection site marked by Paul
the coral polyp, located near Arkona, Ontario, (Google Earth, 2017).

1.4   Methods

Coral specimens, selected for external growth ridge preservation quality by optical microscopy, were thoroughly scrubbed with a toothbrush, and further cleaned in an ultrasonic bath overnight, rinsed in tap water, and air-dried. Selected specimens were scanned using Micro-CT to obtain a record of the three-dimensional structure and to provide information on internal structures. The specimens were then sliced longitudinally along the approximate growth axis, mounted in epoxy on thin sections, before the epithecal edge was imaged using backscatter scanning electron (BSE) microscopy, to examine growth ridges in cross-section. An edge line was extracted using various image processing techniques and was then exported as a set of X,Y coordinates to allow for standard data analysis to be applied. More detail on Methods used in this work can be found in Chapter 4.

1.5   Previous work

Growth features in coral skeletons were first linked to seasonal variation in environmental factors by Ma (1934), who suggested that cyclic skeletal density variations were linked to changes in water temperature. Growth ridges, on the external surface of coral epitheca were first linked to daily growth increments within larger monthly sub-bundles and annual bundles by Wells (1963), who suggested that the relative records in fossil corals may complement absolute dating methods, by providing a higher resolution view of the environmental conditions during daily calcification. Similar growth banding has been observed in stromatoporoids, molluscs, and brachiopods (Clark, 1974; Young and Kershaw, 2005). These growth ridges, which have a density of approximately 200 ridges per cm, were originally counted

by hand to estimate the number of days in a Devonian year. A range of 385 to 410 ridges per year was obtained, similar to the 396 day value obtained through radiometric and astronomical methods. These methods use absolute ages established through the use of radioisotopes and an estimated slowdown of Earth's rotation by two seconds per 100 000 years to determine the number of days per year for a point in time. This difference is believed to be a result of Earth's rotational speed decreasing as its energy is dissipated through tidal friction (Wells, 1963).

Scrutton (1964) first examined periodicity in these growth ridges, tying them to daily (diurnal), lunar monthly (tidal), and annual (orbital) cycles. By dividing the astronomical prediction of 399 days per Devonian year by the average number of growth cycles per sample, it was approximated that a year consisted of 13 lunar months, each 30.5 days long. He suggested that growth ridges are most likely influenced by lunar cycles which trigger a metabolic preoccupation with breeding, slowing growth during spawning periods as energy is diverted from skeletal growth to reproduction (Scrutton, 1964).

The research covered in this thesis will involve imaging Devonian fossil coral specimens, then counting and measuring the daily growth ridges. An attempt will then be made to quantify coral growth and consider the possible influences of astronomical or paleoenvironmental cycles on coral growth patterns. Research in this field, even in modern corals, has been limited. Winter and Sammarco (2010), examined the modern scleractinian coral, *Montastraea faveolata*, from 1961-1991 and found similar annual, monthly, and daily growth bands. They stated that the number of sub-bundles of ridges was tied to the number of lunar months, but that it can also be influenced by water temperature. In cooler temperatures, these monthly bands may not be recorded. Using X-radiography, they found that the number of horizontal

'floors', or dissepiments, per annual growth band within the coral skeleton ranged from 11 to 14, which is in agreement with the number of lunar months. Zhang (2010) counted daily and lunar monthly growth ridges of Carboniferous and Devonian corals and found an average of 12.7 lunar months and 407 days per Devonian year. He also examined seasonal banding and suggested that there were still four seasons in the Devonian year, though winter was shorter and summer was longer than present (Zhang, 2009). Berkowski and Belka (2008) studied the isotopic compositions of seasonal bands, finding that the denser, dark bands were formed during seasons of higher environmental stresses, such as a higher temperature and sedimentation rate, whereas the less dense, lighter bands represented cooler seasons. One pair of light and dark bands is believed to represent one year.

Sun et al. (2002) proposed an analytical method for examining paleoenvironmental records, such as coral growth bands, stalagmites, and tree rings. The first step is digital image acquisition, using various techniques, such as X-ray, infrared photography and microscopy, dependent on the type of proxy record being studied. The layers are then marked/measured along the direction of growth. The images must then be analyzed in order to identify individual layers and calculate the growth rate. Finally, this information must be related to environmental factors that may affect coral growth. This has been one of the few attempts made to quantify coral growth rate and may be applicable to fossil corals as well.

Scanning electron microscopy (SEM) has been used to observe modern aragonitic coral skeletons in an attempt to link skeletal microstructures to environmental factors. Seasonal variations were observed in detrital material trapped within the coral matrix, as well as carbon and oxygen isotopic concentrations (Naqvi, 1994). Barnes (1972) found that external features do not directly correspond with internal structures, as external ridges are formed first,

then aragonite layers are deposited behind. A subsequent study using time-lapse photography

clearly showed a daily cyclicity within the ridges (Barnes and Crossland, 1980). Pol (2014)

studied the efficacy of various imaging methods on rugose corals: SEM, three-dimensional

white light scanning, and Micro-X-ray Computer Tomography (Micro-CT). Based on their

resolutions, 3D white light scanning and Micro-CT were best suited for imaging bundles (an-

nual) and sub-bundles (monthly), whereas SEM was found to be the best method for imaging

the fine-scale ridges.

Chapter 2

Geologic setting

Coral specimens were collected from the 'coral unit' of the Hungry Hollow member of the Widder Formation at the site of a former clay quarry near Hungry Hollow in the Arkona area of Ontario. The Widder Formation is a part of the Middle Devonian (Givetian) Hamilton Group, located in the Chatham Sag (Figure 2.1). This is a local saddle-like area of subsidence bordered by the Michigan Basin to the west, the Appalachian Basin to the east, and the Findlay and Algonquin arches to the south and north, respectively (Figure 2.2) (Bartholomew and Brett, 2007; Edinger et al., 2002).
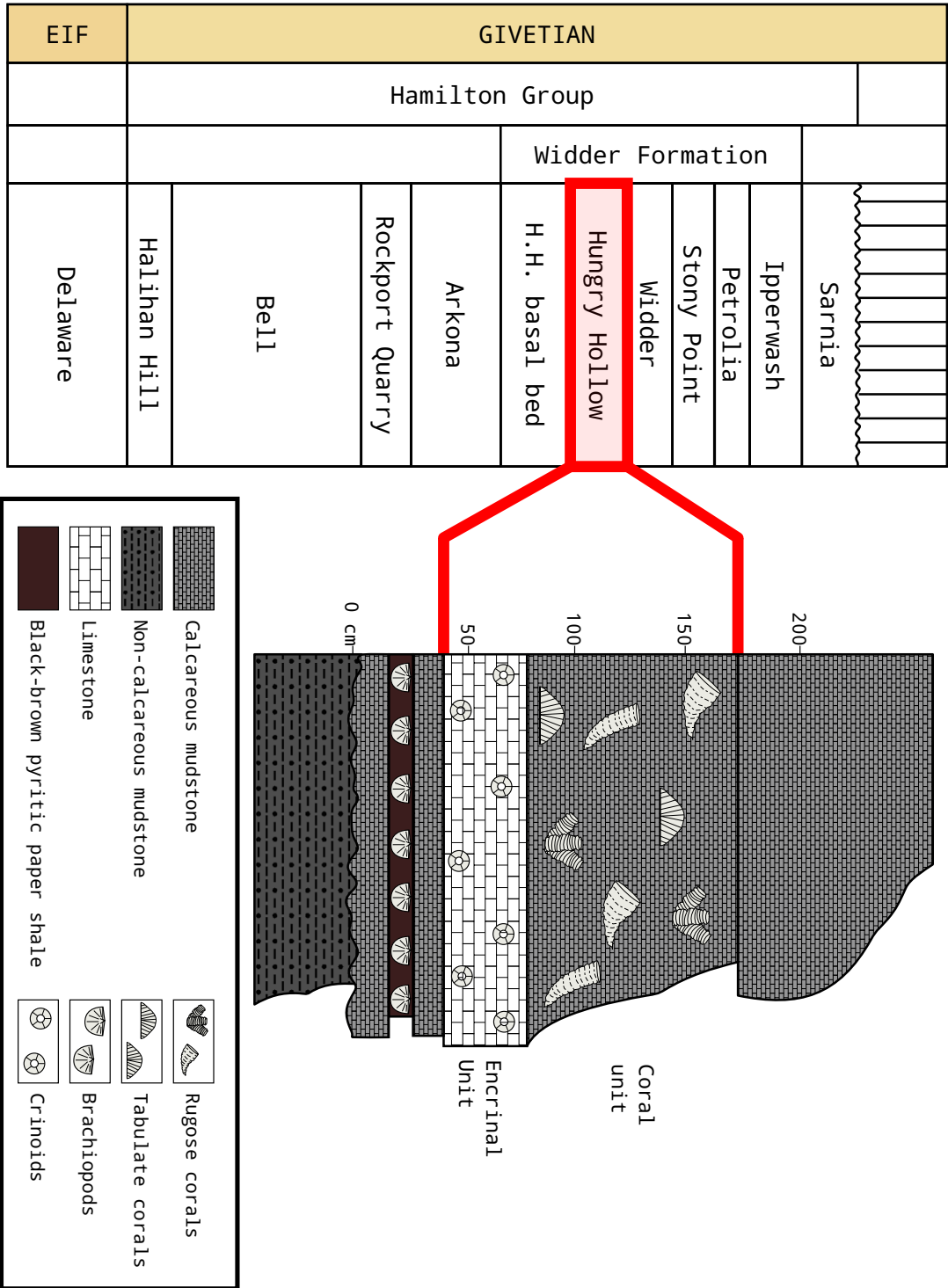
Figure 2.1: Middle Devonian stratigraphy, Chatham Sag region, modified after Brett et al. (2011); Flude (2005).
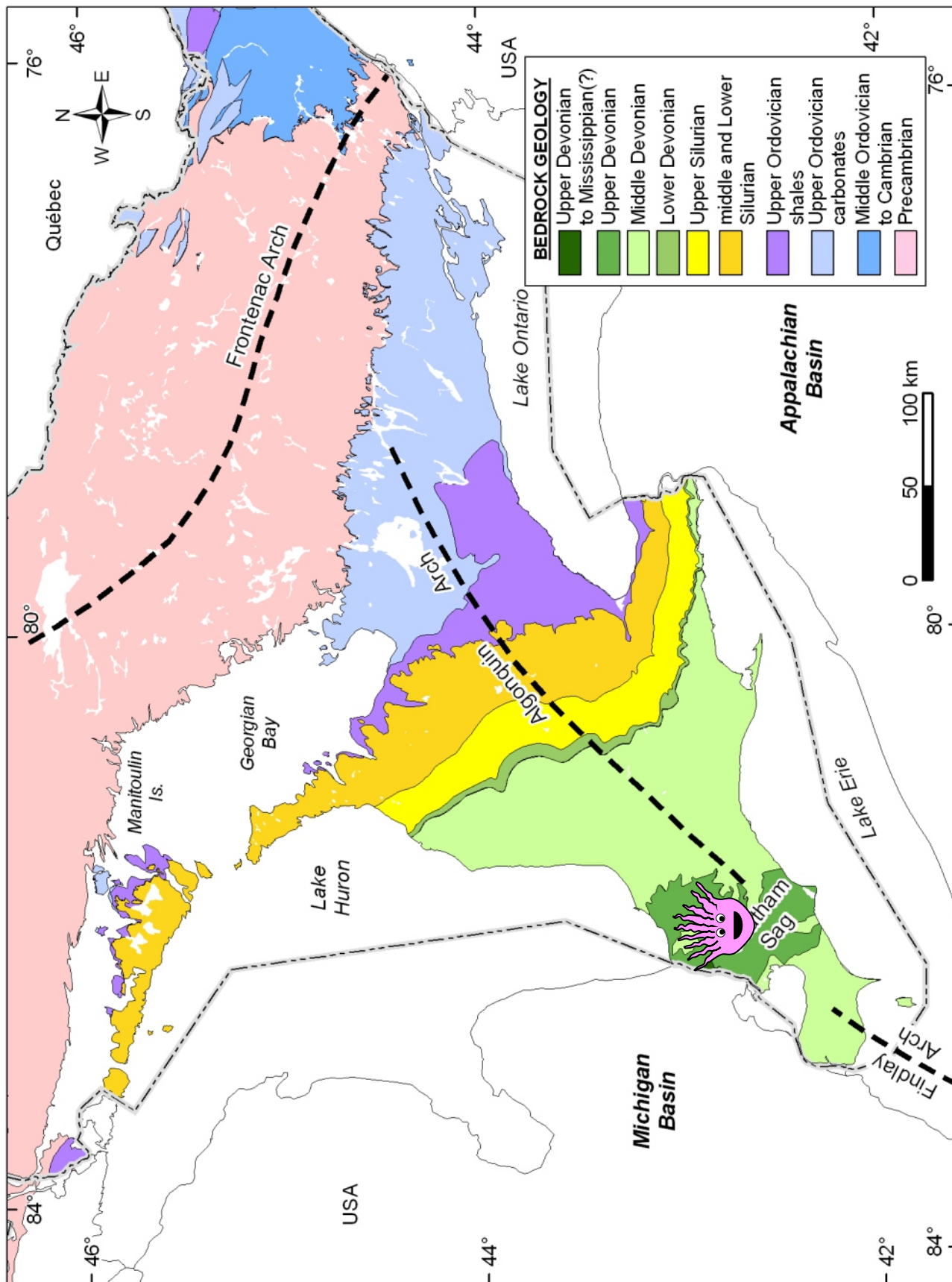
Figure 2.2: Bedrock geology of Southwestern Ontario, with Chatham Sag study area marked by Paul the coral polyp, modified after Armstrong and Carter (2010).

2.1   Basin development

The Michigan Basin is a circular intracratonic sedimentary basin centred in Michigan, extending into southwestern Ontario (Howell and van der Pluijm, 1990). It is bordered by the Wisconsin Highland to the west and the Canadian Shield to the east and north. It is 400 kilometres in diameter, nearly 5 kilometres deep, covers approximately 198,000 km^2, and includes Lake Michigan and Lake Huron. The basin overlies a failed Precambrian rift system, with sedimentary strata ranging from Cambrian to Jurassic in age and dominated by carbonates and evaporites. Subsidence was initiated in the Middle Cambrian, concurrent with the adjacent Illinois Basin; however, due to its inconsistent rate of subsidence (Figure 2.3), the cause remains uncertain (Burgess, 2008).
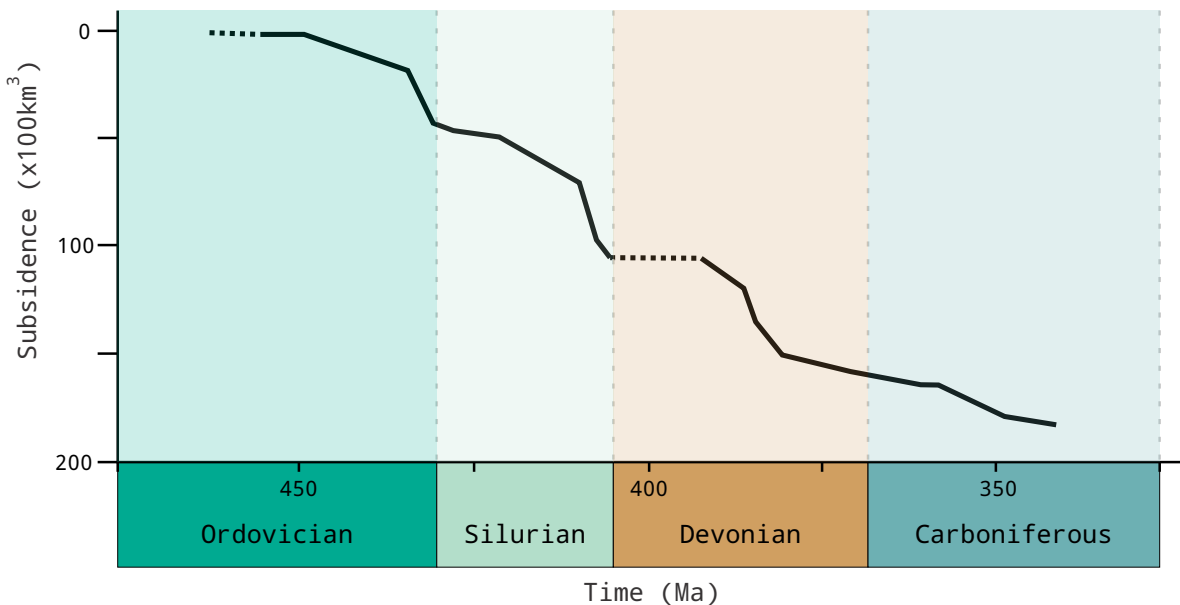
Figure 2.3: Michigan Basin subsidence history, marked by multiple phases, each driven by different mechanisms, modified after Fisher et al. (1988).

Various mechanisms have been proposed for the origins of the Michigan Basin, such as the reactivation of Precambrian basement faults during the Appalachian orogeny, thermal contraction over a continental hot spot, crustal phase changes, thermal convection, and lithospheric stretching (Howell and van der Pluijm, 1990; Sloss, 1988). Ahern and Dikeou (1989) proposed that a single Cambrian thermal event initiated subsidence and that the absence of fault blocks suggested that it could not have formed as a result of lithospheric stretching alone. This fails to explain the multiple changes in the rate of subsidence, however. In an attempt to explain the inconsistent rate of subsidence, Howell and van der Pluijm (1999) described multiple phases, organized into seven structural sequences, each representing a different pattern and cause of subsidence. While this has been the most extensive explanation, these phases do not exactly match stratigraphic sequences described by other authors and therefore do not fully explain the origin and evolution of the basin.

Johnson et al. (1985) estimated a sea-level curve for the Devonian Euramerican continent and found a minimum of 14 eustatic transgressive-regressive cycles and suggested that the three dominant regressive phases may have been a result of submarine volcanism and thermal uplift most likely globally driven. Water depth ranged from 10-50 metres in the Middle Devonian Michigan Basin (Bartholomew and Brett, 2007). After tracing marker beds across eastern North America and finding similar sequences across the Michigan and Appalachian basins, Brett et al. (2011) revised this curve, suggesting that it was likely missing many smaller (fourth, fifth, sixth) order cycles as well (Figure 2.4). Similar sequences are found across North America, in basins with different mechanisms and sedimentation styles, suggesting that sea level change in Eastern North America was likely globally driven, but modified by local tectonism and geography. Biostratigraphic correlation, as well as erosion

patterns, suggest that the Michigan and Appalachian basins were connected during deposition and the Findlay arch developed later. Decreased sedimentation further from the Appalachian mountain clastic source may explain the increased carbonate productivity of the Hungry Hollow area compared to similar settings in the Appalachian Basin. (Bartholomew and Brett, 2007).
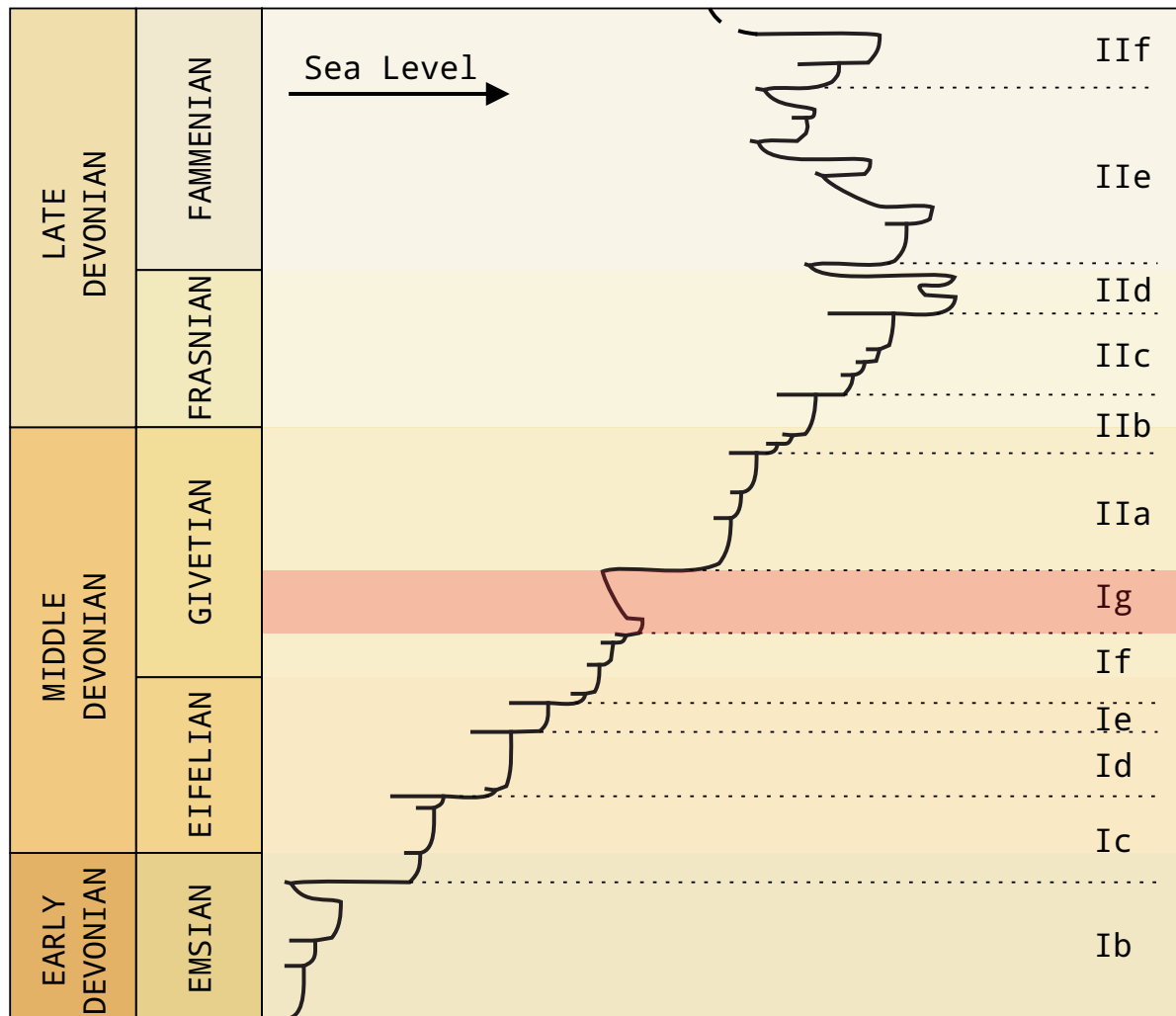
Figure 2.4: Devonian sea level curve, with low sea level during the Hungry Hollow depositional period highlighted, modified after Brett et al. (2011).

2.2 Stratigraphy

The Hungry Hollow member belongs to the Middle Devonian Widder Formation, of the Hamilton Group, which bridges the Michigan and Appalachian basins (Figure 2.6). The mixed siliciclastic-carbonate Hamilton Group marine succession records a series of transgressive-regressive cycles, manifested as stratal packages with abrupt changes between fossiliferous carbonate units (regressive) and underlying shaly units (transgressive), as the environment transitioned from dysoxic to highly productive conditions (Bartholomew et al., 2006). The Hungry Hollow member itself consists of two fossiliferous units: a lower 'encrinal unit' composed of crinoid-rich grey packstone, rich in crinoids, and the upper 'coral unit', consisting of a fine, grey carbonate mud packed with rugose and tabulate coral (Figures 2.6, 2.7) (Bartholomew and Brett, 2007; Donato, 2003; Wright and Wright, 1961). The coral unit is believed to represent minimum sea level during a small-order regression within a larger-scale, overall transgression (Bartholomew et al., 2006). Below, the Hungry Hollow encrinal unit has a sharp, erosive surface at its base (Figure 2.8), which marks the Hungry Hollow basal bed. This is a 5-10 cm thick black phosphatic, highly fissile shale with brachiopods (*Leiorhynchus*), believed to represent highest sea level before the small-order Hungry Hollow regression. This overlies the Arkona shale, a thick mudstone unit, deposited in a marine setting with low carbonate productivity (Bartholomew and Brett, 2007).
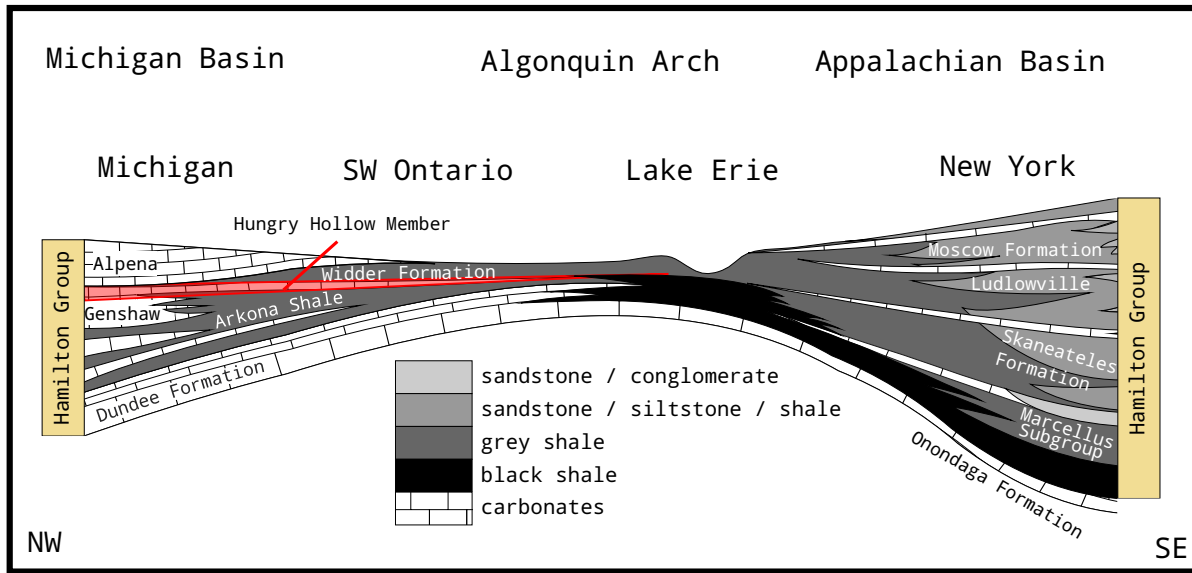
Figure 2.5: Michigan Basin cross-section, with Hungry Hollow Member study area highlighted in red, modified after Bartholomew et al. (2006); Flude (2005).
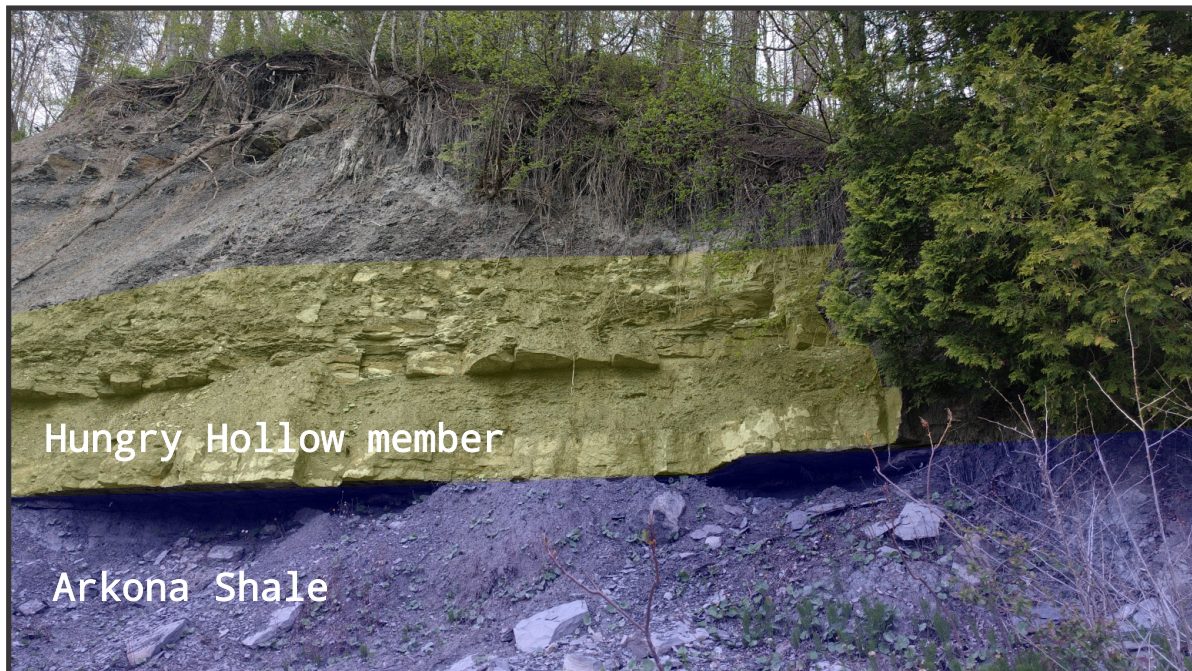
Figure 2.6: Ausable River outcrop near Arkona, Ontario. Hungry Hollow Member, shaded in yellow, ~1 m thick, taken May 13, 2016.

Figure 2.7: Hungry Hollow member sub-units, Ausable River, outcrop near Arkona, Ontario. Coral (green) and encrinal (yellow) units have a combined thickness of ~1 m, Hungry Hollow basal bed (orange) is ~8 cm thick, taken May 13, 2016.
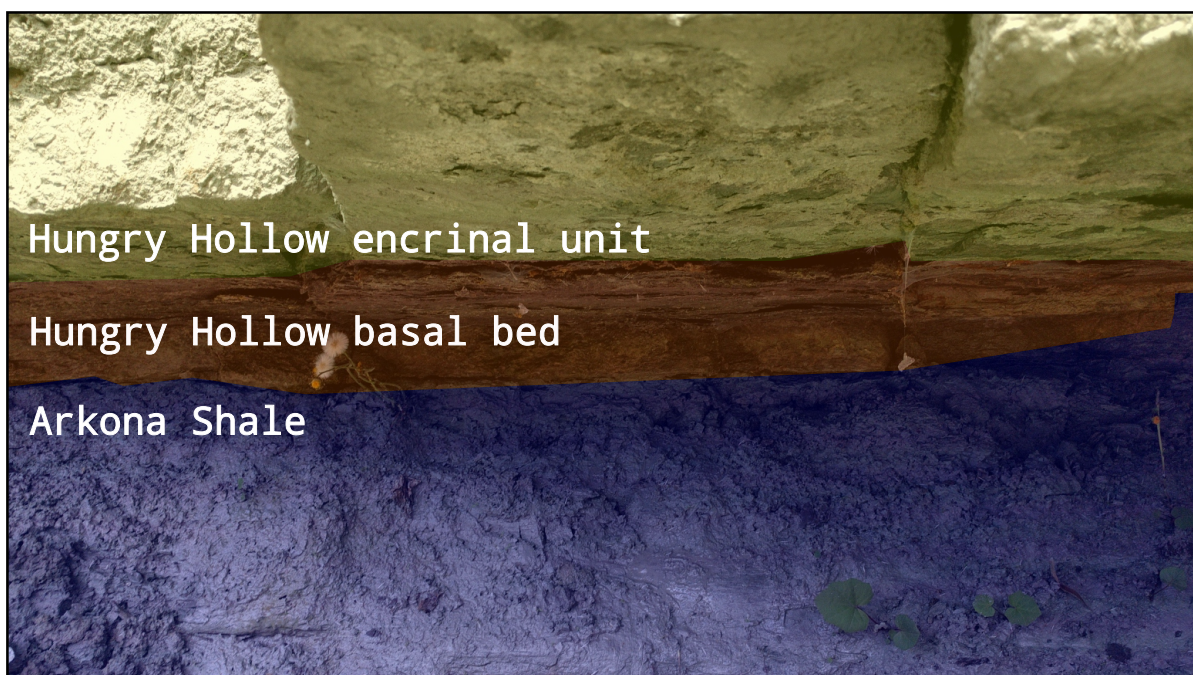
Figure 2.8: Hungry Hollow - Arkona Shale transition, Ausable River outcrop near Arkona, Ontario, taken May 13, 2016.

2.3   Paleoenvironment

During the Middle Devonian, the Chatham Sag area of the Michigan Basin was a warm,

shallow, subtropic $(30 - 35°S)$, epeiric sea environment (Figure 2.9).
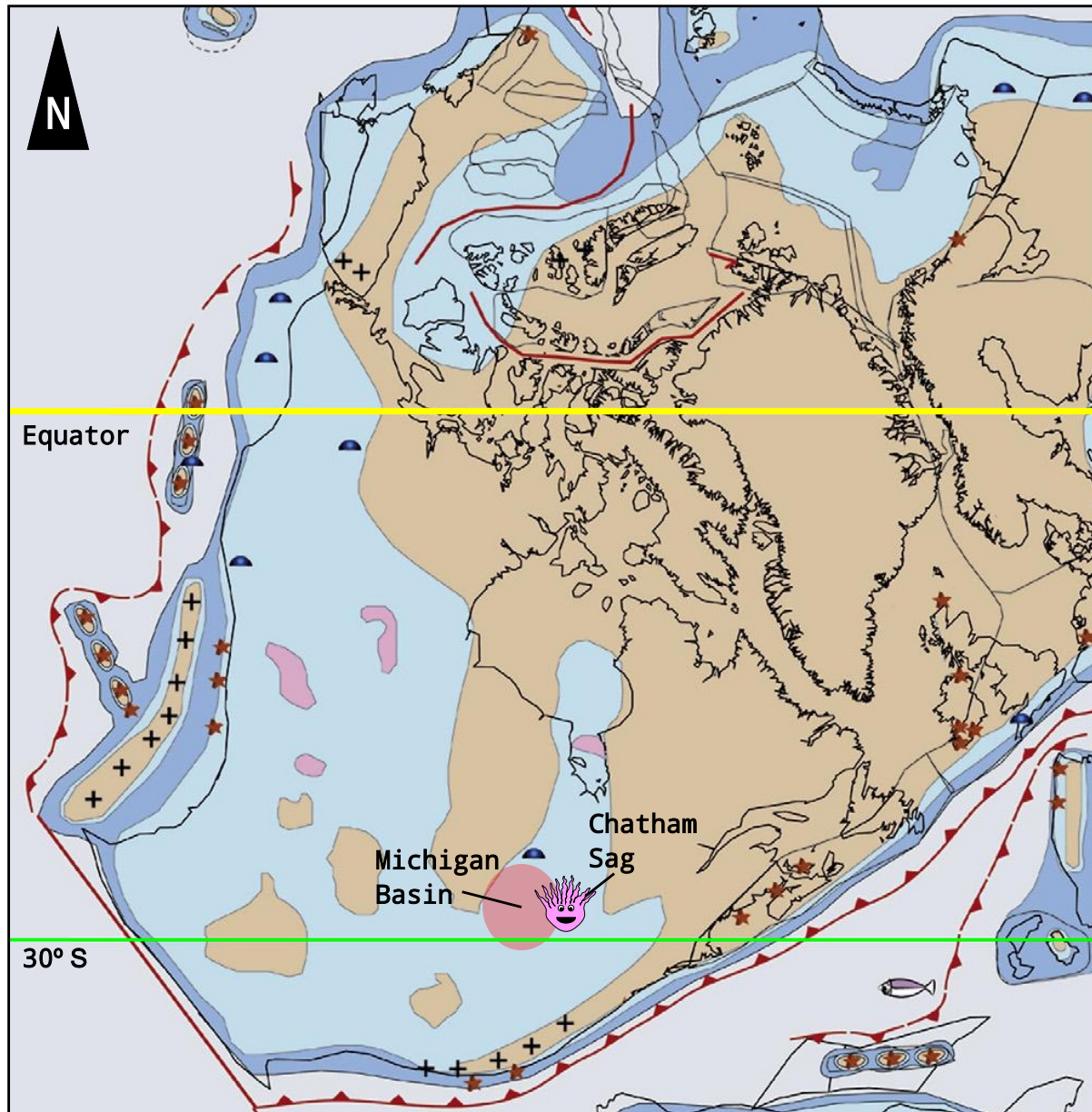
Figure 2.9: Middle Devonian (370 Ma) paleogeographic setting, with study area marked by Paul the
coral polyp, modified after Cocks and Torsvik (2011).

Edinger et al. (2002) described epeiric seas as well-mixed, with increased tidal ampli-
tudes and storm influence due to their shallow depth. As in the modern-day Persian Gulf, the
Middle Devonian Hungry Hollow area was a saline environment caused by anti-estuarine cir-
culation, where evaporation output exceeds combined precipitation and runoff input (Fig-
ure 2.10). Denser, saline waters sink, as oxygenated, nutrient-poor surface waters come from
deeper in the basin, where they are kept nutrient poor due to limited siliciclastic input. These
conditions favour more complex, slower-growing, carbonate buildups such as reefs and limit
organic-rich black shale deposition. Nutrient-rich waters promote eutrophication by simpler,
heterotrophic organisms, such as calcareous algae, bryozoans, and sponges, and encourage
black shale formation (Edinger et al., 2002). The limited siliciclastic input, combined with
high carbonate productivity led to the formation of a hard bed to which rugose and tabulate
corals could attach (Baird and Brett, 1983).
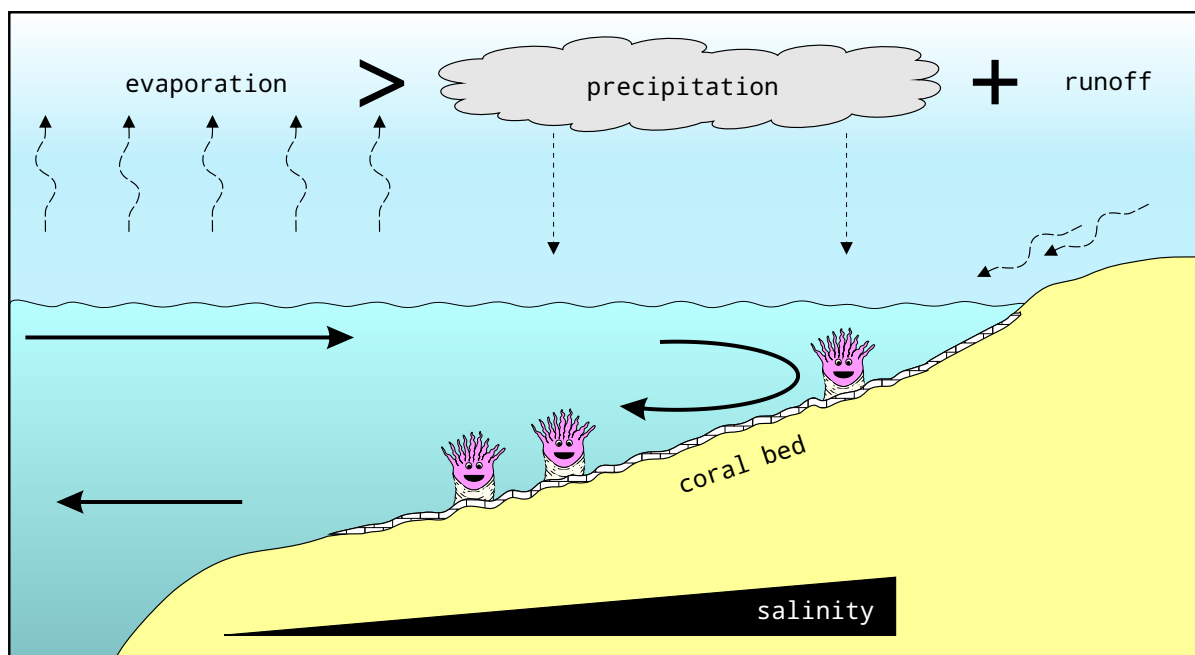
Figure 2.10: Anti-estuarine paleoenvironment of Hungry Hollow member, Widder Formation
biostrome (375 Ma); evaporation losses exceed combined runoff and precipitation influx,
increasing salinity and water temperature, modified after Edinger et al. (2002).

Chapter 3

Coral systematics, biology and skeletal growth

3.1 Evolution and classification of corals

Corals are a group of marine invertebrate animals (Class Anthozoa, Phylum Cnidaria). Though their form and arrangement of features may vary, a coral, in its simplest form, consists of a polyp housed in an acellular (non-living) calcium carbonate ($CaCO_3$) skeleton. The polyp is a double-walled sac with one opening (mouth). The living polyp rests in a cup shaped depression atop the coral skeleton (calice). The inner (endoderm) and outer (ectoderm) cell layers are separated by a jelly-like substance (mesoglea), which allows the coral to maintain its shape and also contains nerves and musculature for feeding, digestion, and response to stimuli (Clarkson, 1998). Layers of calcium carbonate are progressively laid down as the coral grows away from its original attachment point to form a skeleton. Calcification can only occur where the polyp is in direct contact with the skeleton, a differentiated part of the ectoderm, known as the calicoblastic layer (Figure 3.1) (Barnes, 1972).
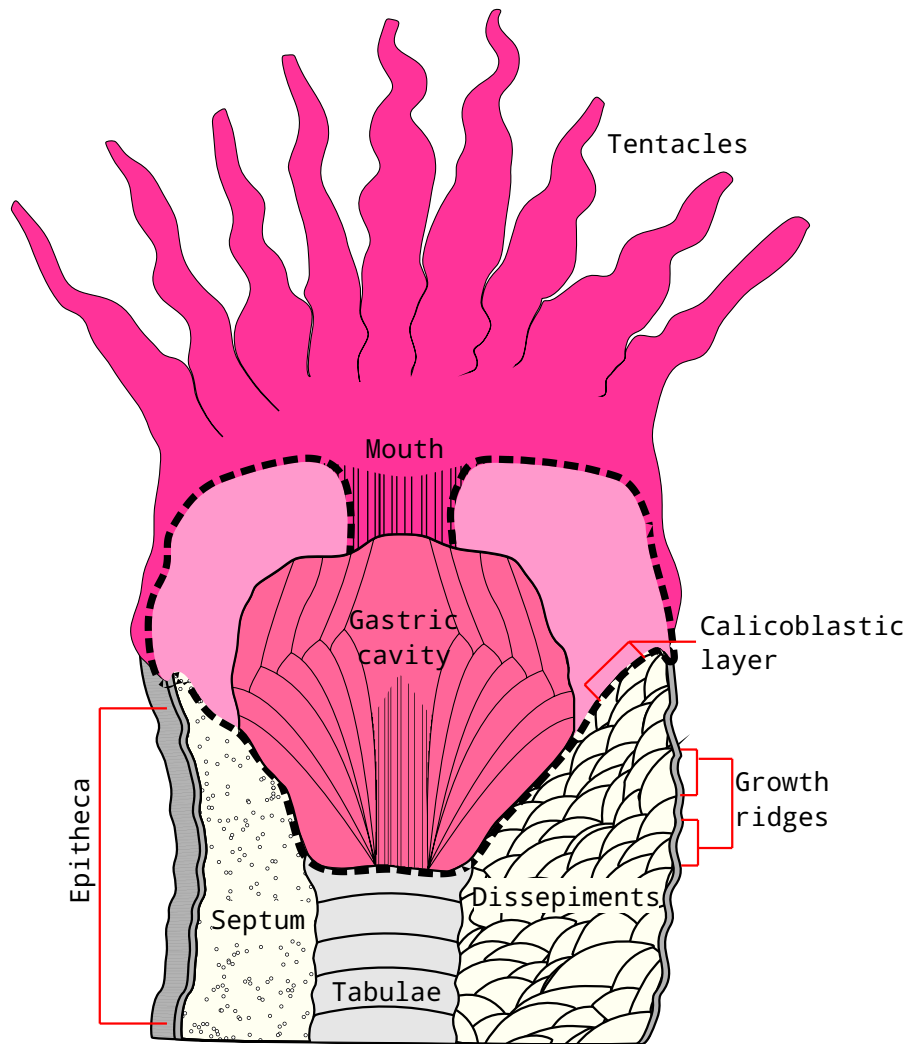
Figure 3.1: Rugose coral anatomy, inferred from fossil skeletal structure, modified after Scrutton (1978).

A coral polyp occupies only the top portion of its skeleton. The skeleton records previous growth positions, with a repeating set of features formed at each growth increment. These can be divided into major and minor structures (Figure 3.2). The epitheca, a sheet-like 'skin' of calcium carbonate, encloses the skeleton and records previous growth locations, with changes in growth rate reflected as changes in skeletal diameter. Continuous vertical plates (septa) radiate outwards from the centre and have distinct symmetry based on coral family. The polyp rests in the calice on a central horizontal plate (tabula). Concave dissepiments form out and upwards to the corallite lip, to create a cup, securing the polyp. The tabularium is a central

column formed as tabulae grow above one another, to create a spine-like structure parallel to the growth axis (Clarkson, 1998; Cohen and McConnaughey, 2003). The dissepimentarium forms the rest of the skeletal diameter and acts as a buffer zone for the coral. The size and frequency of dissepiments reflect the health of the polyp. When the coral is thriving, the dissepimentarium expands to increase size, stability on soft substrate, and support a larger polyp with additional tentacles for feeding. When conditions hinder growth, the dissepimentarium shrinks and the skeletal diameter becomes closer to that of the tabularium. As the corallite extends upwards, the polyp begins to lift off its basal dissepiment, and through a combination of mechanical and hydraulic pressures, deposits another for support. As a result, these internal convex supports are out of sync with cyclic external growth ridges (Berkowski, 2011).
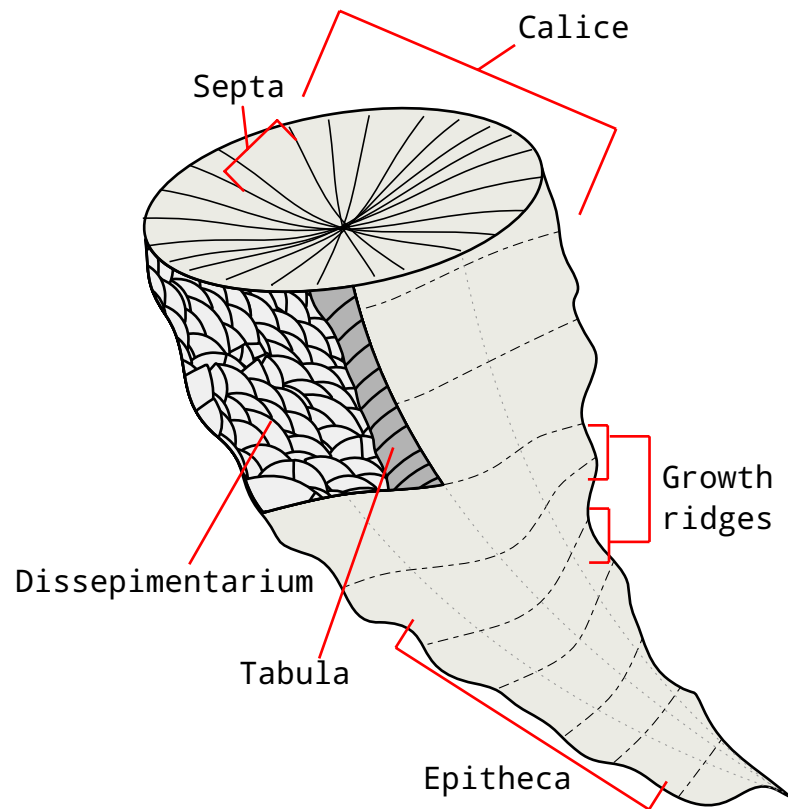
Figure 3.2: Rugose coral skeletal structure, modified after Clarkson (1998).

Covering approximately fifteen percent of all seabed shallower than fifteen metres to-

day (284 300 km^2), corals are typically found in tropic to sub-tropic latitudes (30°N - 30°S), though, cold, deep-water variants exist (Allemand et al., 2004; Pandolfi, 2011; Smith, 1978). Corals are microcarnivores, and use tentacles to draw in planktonic organisms and nutrients from seawater. Some corals share a symbiotic relationship with photosynthetic algae that live within the coral polyp. These provide additional nutrients to allow for a much higher growth rate (Dubinsky and Falkowski, 2011). They are believed to have evolved through the progressive addition of features and complexity, beginning with the development of a skeleton by an unknown species of anemone (Baars et al., 2013) The three dominant families of corals in the fossil record are: Tabulata, Rugosa, and Scleractinia (Figure 3.3). Tabulate and rugose corals, now extinct, excreted a calcite skeleton and dominated Paleozoic carbonate reefs until their extinction in the Middle Ordovician. Shortly after, aragonitic scleractinians have since become the major reef-builders, through present day. Originally considered to be descendants of the previously mentioned Paleozoic corals, it is now presumed that all three families are monophyletic (Baars et al., 2013; scr).
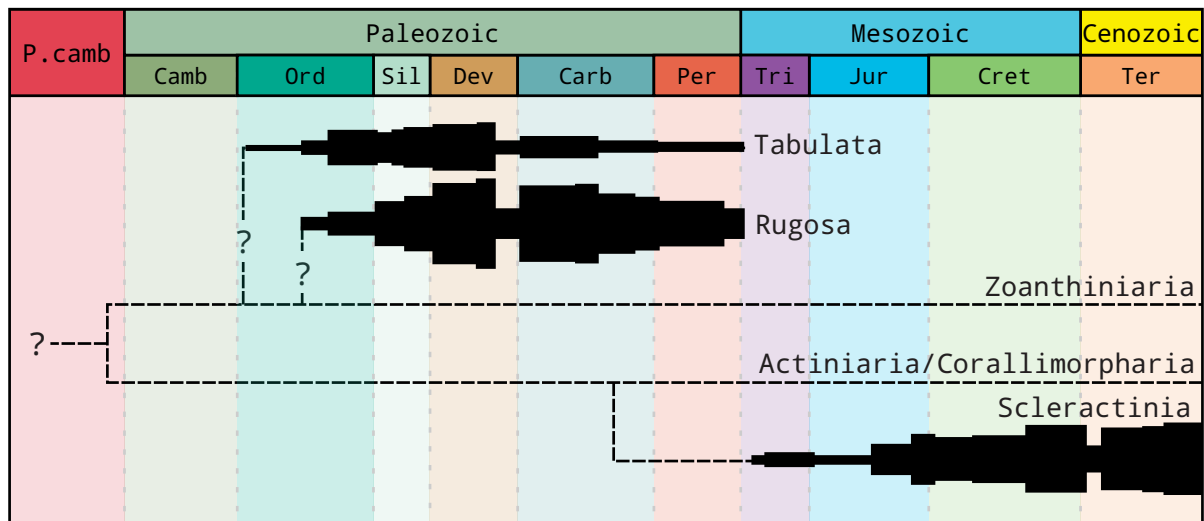
Figure 3.3: Paleozoic coral taxonomy, modified after scr.

.

3.1.1   Paleozoic corals

Tabulate corals

Tabulate corals, which first appeared in the Early Ordovician, were colonial organisms that formed massive calcite skeletons. A network of amural pores connected all individual polyps within a colony, allowing them to share oxygenated and nutrient-rich waters. Each corallite was fully integrated within the colony (corallum), enveloped within a continuous epitheca, with no clear divisions between individuals. They are distinguished from other massive colonial corals by the presence of continuous floor-like tabulae which run throughout the colony (Clarkson, 1998; Scrutton, 1997). This coral group went extinct by the end of the Permian Period.

Rugose corals

Rugose corals, commonly referred to as 'horn corals' due to their commonly horn-shaped skeletons (in solitary forms), first appeared in the Middle Ordovician (Scrutton, 1997; Baars et al., 2013). They feature bilateral symmetry, excreted a calcite skeleton with an outer wrinkled layer (epitheca) which records previous growth positions as 'growth ridges' (Wells, 1963; Scrutton, 1964, 1997). Rugose corals exhibited both solitary and colonial lifestyles. Colonial growth forms do not show signs of inter-connectivity between individual polyps as seen in tabulate corals. Each coral was its own entity only sharing growing space and nutrients within common seawater (Scrutton, 1998). Solitary rugose corals seem to have had a non-fixosessile lifestyle; that is, after initial gamete attachment, they rested freely on the sea floor, partially submerged in sediment, not directly fixed to a hard surface. They could rapidly

alter their growth direction to re-stabilize after a disruption event, such as a failed predation attempt or storm, with the ultimate determinant of survivability the dependent on the coral's ability to stay upright and stable on soft substrate (Neuman, 1988).

Taxonomic diversity of Paleozoic corals peaked during the Givetian Stage (mid-Devonian Period), when they were the major reef-builders, along with calcareous algae and stromatoporoids. Three dominant extinction events affected Devonian reef environments: end Frasnian, end Givetian, and finally mid-late Fammenian, by which time, corals dramatically declined in abundance and diversity, effectively ending Devonian reef production (Baars et al., 2013; Fagerstrom, 1994). By the end of the Permian Period, both rugose and tabulate corals were extinct.

3.1.2   Modern corals

Scleractinian corals appeared in the fossil record in the Middle Triassic, after the extinction of rugose and tabulate corals (Stanley and Helmle, 2010). Also known as stony corals, for the hard, stone-like skeleton they produce, these corals are the dominant reef builders today, in such areas as the Mediterranean Sea and off the northeastern coast of Australia (Great Barrier Reef). They commonly share a symbiotic relationship with photosynthetic algae, zooxanthellae, which live within the polyp, providing nutrients and oxygen (products of photosynthesis), in exchange for carbon dioxide (produced through respiration) and protection from predation (Clarkson, 1998; Allemand et al., 2004). Scleractinians have been successfully used as paleoclimate proxies, recording environmental changes since the industrial revolution (Abram et al., 2001; Kuhnert et al., 1999; Moyer and Grottoli, 2011; Nie et al., 1997).

As rugose corals are long extinct, with no clear descendants, modern Scleractinian corals must be used as an analogue, though their differences must be considered. The symbiotic relationship between modern coral and photosynthetic zooxanthellae drives growth and is sensitive to environmental changes, as seen in coral bleaching events in the Mediterranean Sea and Great Barrier Reef. The coral's environmental tolerances are effectively controlled by the zooxanthellae, which thrive within a narrow window of temperature and light availability (Rubio-Portillo et al., 2014). There is limited evidence of a symbiotic relationship in rugose corals, as examination of internal structure, life strategies, and development suggest they are quite different and rugose corals may be more closely related to Zoanthids, based on similarities in polyp layout (Rozhnov, 2014; scr; Sorauf, 2001).

3.2   Coral growth

Corals calcify more rapidly than most animals, at a rate of approximately one hundred times that of inorganic aragonite precipitation in seawater. Aragonite is laid down rapidly, in an unorganized fashion (Cohen and McConnaughey, 2003).The two main measures of growth in corals are linear extension and skeletal density (Baker and Weber, 1975). These two types of calcification follow a diurnal pattern; corals extend upwards at night by building a weak framework which is then strengthened through daytime infilling (Barnes, 1970; Cohen and McConnaughey, 2003). Calcification begins within folds in the calicoblastic layer, at nucleation sites referred to as calcification centres. Sr/Ca elemental ratios have shown that these sites form in the absence of photosynthetic symbionts. Fine, needle-like aragonite crystals grow outwards and upward like fingers from these sites to produce fan-like bundles (sclero-

dermites). As nucleation sites progressively develop upwards, sclerodermites grow upon one another to form a vertical column (trabeculae). Adjacent trabeculae grow into each other to form a wall (septum), the major vertical structure within coral skeletons (Figure 3.4). The mechanisms of calcification are the same in those with or without photosynthetic zooxanthellae, though the arrangement of these structures may vary based on coral family and the internal arrangement of the polyp (Cohen and McConnaughey, 2003). As the coral essentially lifts itself upwards, convex dissepiments are laid down underneath the polyp, sloping from the calice lip toward the tabula, potentially through a combination of mechanical and hydrostatic forces. They best reflect the growth conditions of the coral and are responsible for the majority of their skeletal diameter. As the coral grows upward, the calice steepens, increasing the difficulty of the coral remaining open, in contact with the corallite lip. These forces increase until a new basal plate (tabula) is deposited to support the increase in size (Berkowski, 2011).

The previous positions of the upper lip of the coral calice are recorded as 'growth ridges' in the outer epithecal surface, as cyclic deviations from an ideal skeleton with constant growth rate. To investigate the formation of growth ridges, Barnes (1972) dyed modern corals in alternating colours, then used optical microscopy to observe changes in skeletal colour to determine the timing of calcification. He described the formation of growth ridges in corals as a response to cyclic polyp expansion and contraction in response to some external factor. As the polyp rests in the calice, a small portion is in contact with the upper lip of the cup-shaped depression (lappet) and is responsible for the formation of the epitheca, the outer surface of the corallite. As the coral expands and contracts, the lappet folds and unfolds over the epithecal edge. When folded, calcification begins in the lappet canal, a fold within the calicoblastic
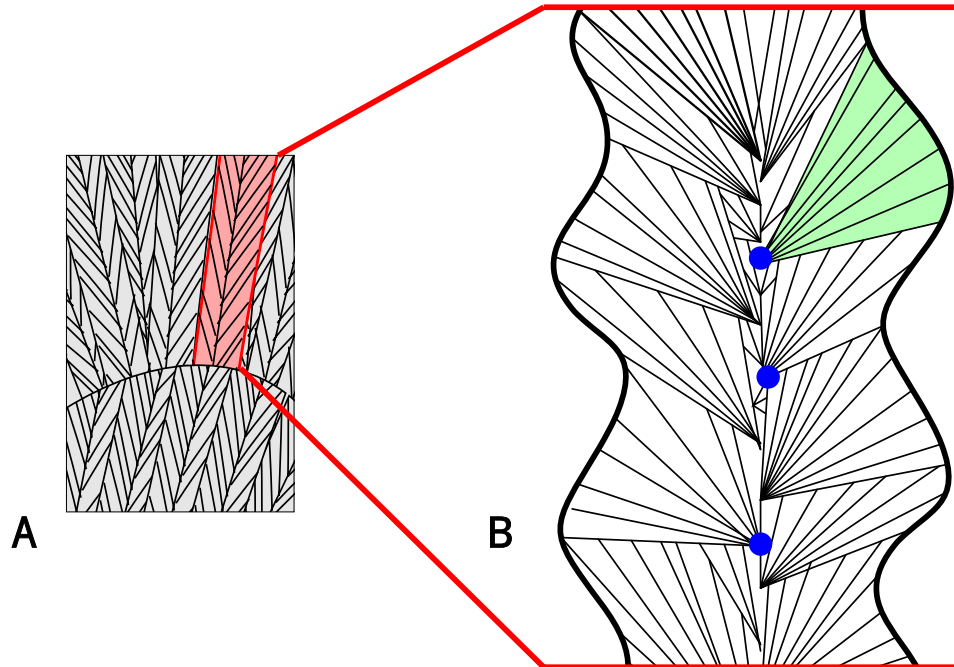
Figure 3.4: (A) Coral septal wall formed as adjacent trabeculae (red) grow into each other. (B) Trabecula consist of stacked sclerodermites (green), fan-like bundles of fine aragonite fibres, with each bundle developing from a common calcification centre (blue), modified after Cohen and McConnaughey (2003).

.

layer. Calcium carbonate is deposited as a new ridge at the top of the epitheca and strength-

ening layers behind lower, previous ridges (Figure 3.5). Barnes (1972) determined that these

external features are out of phase with internal structures such as density banding studied in

corals, as alternating stripes in the longitudinal cross-section confirmed that layers across the

diameter of the coral are deposited at different times. In cross section, the epitheca has a wavy

appearance, controlled by the shape of the lappet as it folds and unfolds over the previous

ridge. This leads to an overall wrinkled outer appearance.
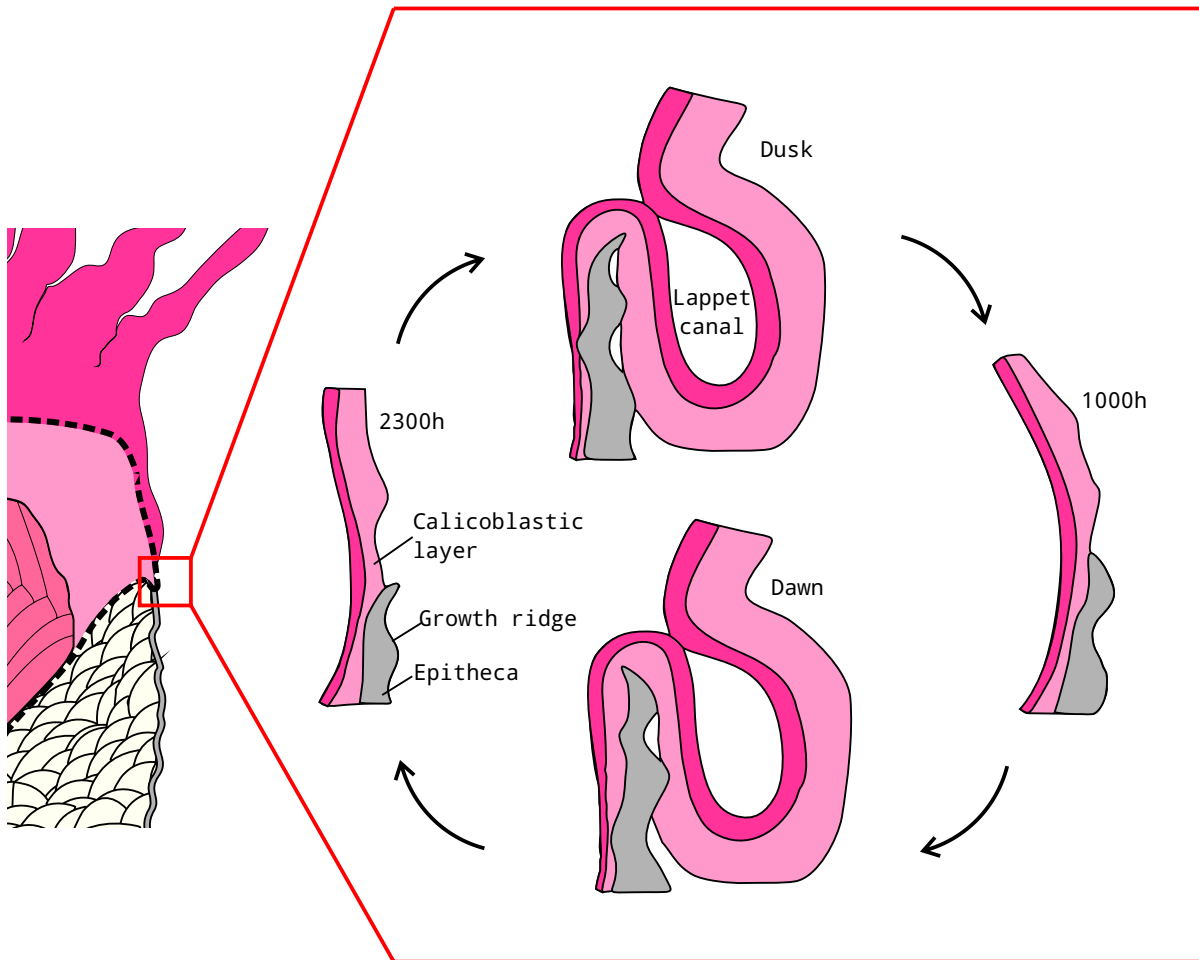
Figure 3.5: Growth ridge formation through cyclic lappet folding and unfolding, driven by polyp contraction and expansion modified after Barnes (1972); Scrutton (1978).

Barnes (1972) suggested that mechanism of formation appears to be the same in all organisms with similar epithecae-like features, such as sclerosponges, though the cyclic drivers may vary. In the case of the modern scleractinian coral, *Mancinia areolata*, ridge formation follows the diurnal light-dark cycle, appearing to be linked to opening and closing for feeding at night due to decreased photosynthetic algal activity. The deepwater coral, *Gardineria*, features similarly structured growth ridges; however, a diurnal cycle would imply a lifespan of a few months, in disagreement with individuals tens of years old. He then suggested that cyclic polyp expansion and contraction could be controlled by various external factors, though little

information was given on potential cyclic environmental drivers of that scale (Barnes, 1972).
It is possible, however, that in the case of *Gardineria*, growth rate is sufficiently slow enough,
to mask the smallest scale ridges, as they may be too fine to be detected and that the 'ridges'
observed were actually larger, perhaps seasonal growth intervals. Polyp constriction and ex-
pansion may also be less pronounced in non-photosynthetic corals, as they do not benefit
from a daily increased energy supply.

3.3   Environmental influences on growth

Growth rate is highly dependent on the living conditions of the coral's environment. Any
changes in factors such as tidal cycles (potentially influencing water depth, salinity and/or
possibly turbidity), nutrient supply, surface water temperature, water depth, lunar breed-
ing periodicity, available light, and sediment supply may be reflected in the coral skeleton
as metabolic energy is diverted away from growth (Scrutton, 1964). In modern photosyn-
thetic coral, light availability and water temperature are the main controls on coral growth
(Baker and Weber, 1975). Rosic et al. (2014) studied the effect of thermal and nutrient stress
on *Acropora aspera* and found that environmental stresses are quickly reflected as changes in
gene transcription to alter the metabolic processes of the coral, diverting energy away from
growth to enhance survival (Rosic et al., 2014). These factors may be reflected as changes
in skeletal diameter through metabolic reactions, such as altering calcium carbonate excre-
tion rate, or by directly affecting the polyp size, changing the surface area of the calicoblastic
layer, where calcification occurs.

Water temperature appears to be the most important environmental factor affecting mod-

ern coral growth, strongly correlated with calcification rate (Lough and Barnes, 2000; Nie et al., 1997). Not only is it difficult to determine the effects of a single environmental factor on coral growth, the presence of photosynthetic zooxanthellae may mask the mechanisms behind changes in growth. A decrease in skeletal diameter may reflect direct environmental stress upon the polyp, or a decrease in photosynthetic activity by symbiotic algae. This relationship clouds the interpretation of modern coral, as well as fossil specimens, which may or may not have shared this photosymbiotic relationship. Jacques et al. (1983) found that coral polyp cellular respiration rate remained fairly consistent within 11.5 - 23 °C, but quickly dropped off outside of that range. Corals from intertidal and backreef settings faired better in a wider range of temperatures than forereef corals, acclimated to consistent conditions. They suggested that corals have a thermal range and that photosymbionts may provide extra energy for coral growth (Jacques et al., 1983). Corals are sensitive to low temperatures, as Isern et al. (1996) found that in the case of modern corals in northeast Australia, growth rates are significantly decreased when sea surface temperatures are below 24 °C and Cohen and McConnaughey (2003) noted that photosynthetic corals are rarely found in water below 18 °C. As temperature decreases, there is a reduction in plankton population, on which coral prey, and as a result, less energy for the coral to allocate to growth, as well as a reduction in photosynthetic algae activity within the coral. Decreased temperature also decreases the rate of chemical reactions, thereby decreasing calcification rate. Seasonal variation appears to control the larger scale, annual bundles seen on coral epitheca, as well as skeletal density.

Coral growth is equally sensitive to high temperatures. Lough and Barnes (2000) examined the modern coral, *Porites*, and found that from 1800-1990, for every 1 °C increase in average yearly air temperature, average annual calcification increased by 4.5%. As seen in re-

cent coral bleaching events in the Great Barrier Reef and Mediterranean Sea, a small increase in temperature can have devastating effects on coral reefs, as Kushmaro et al. (1998) noted that coral growth rate dramatically decreases above 29 °C.

Tidal activity could be linked to variations in multiple controls within a coral's environment, such as water depth, nutrient supply, light availability, turbidity, and temperature, though changes appear to be minimal (Scrutton, 1964). Baker and Weber (1975) investigated the effect of water depth on modern coral *Montastraea annularis* growth and found that calcification occurs most rapidly at intermediate depths. Average corallite density increased with depth, whereas linear extension rate increased, until a threshold at 9 metres deep, at which point extension rate quickly decreases with depth, before dropping off at a critical depth of 18 metres, though daily rhythmic variation in calcification is more likely to be seen across an environmental gradient, rather than within an individual (Baker and Weber, 1975). Short-term fluctuations in nutrient supply are unlikely to affect coral growth on a daily scale, due to the slow digestion rate of plankton by coral (Scrutton, 1964).

Reproductive influences on coral growth

The reproductive patterns of many marine invertebrates are synchronized with the lunar cycle (Gorbunov and Falkowski, 2002). Corals begin growth after a larva (planula) settles on a surface, though there are two methods of sexual reproduction: broadcasting and brooding (Clarkson, 1998; Tanner, 1996). Broadcasting corals typically reproduce during an annual mass spawning event, marked by the synchronized release of sperm and egg cells among all individuals within the reef, for fertilization (Tanner, 1996). This commonly occurs in the early summer, but always within a week of a full moon. Brooding corals directly release ma-

ture larvae, with fertilization occurring within the parent polyp (Tanner, 1996).

In a review of the reproductive patterns of various species of modern corals, Airi et al. (2014) found that coral oocytes (female gametes) are commonly produced in correspondence with the lunar cycle, but may be broken down and resorbed as a source of energy within coral polyps before they can be expelled and/or fertilized. This suggests that lunar cycles may initiate the early stages of reproduction, when energy investment is low, but the energy requirement for gametocytes to reach maturity is sufficiently high that the coral must reach a peak energy surplus before their release (Airi et al., 2014). Temperature appears to be the other dominant control on the timing of coral spawning reproduction, perhaps by increasing photosynthetic productivity or the polyps metabolic rate, as there is a strong link between the timing of gamete release and elevated sea surface temperature. Scrutton (1964) suggested that the skeletal growth interruptions that bracket assumed monthly growth bands (sub-bundles of growth ridges) in rugose corals may be a result of the high energy requirement during the production of sex cells (gametogenesis), driven by lunar periodicity, perhaps triggered by moonlight or changing water pressures during spring tides. The organism would have diverted metabolic energy away from polyp expansion and skeletal growth, resulting in a marked constriction in corallite diameter and/or brief pause in skeletal secretion (Scrutton, 1964).

3.4   Coral response to environmental cues

Corals, both fossil and modern, show a strong ability to adapt to external stressors, through rapid constriction and subsequent rejuvenescence. Rejuvenescence is the process whereby a coral polyp returns to its normal growth form after rapid constriction due to some severe ex-

ternal event. Under normal growth conditions, polyp size will slowly adapt to gradual changes in temperature, narrowing in the colder, winter months and broadening in the summer. If the polyp is subjected to sudden stress, such as injury, extreme weather, sediment burial, or breeding it may rapidly shrink, which is reflected in the skeleton as constriction (narrowing), as the polyp must rapidly shrink to conserve energy to survive (Berkowski, 2011). If the coral survives the event, it returns to its normal growth form, a process known as rejuvenescence (Fedorowski, 1978). The shrunken polyp begins the formation of a new calice and subsequent growth ridges within the old one. Growth direction can remain constant (axial rejuvenescence) or deviate, forming a bend (lateral rejuvenescence), dependent on how the polyp reattaches after constriction (Figure 3.6) (Berkowski, 2011). Many rugose coral fossils show evidence of their ability to repair their skeleton when damaged, presumably after a failed predation attempt. Rugose corals could return to a normal growth form after damage, ranging from small chips in the calyx, to the loss of large pieces of the skeletal wall, by diverting energy to repair. This typically is observed as disordered, skeletal patching, followed by immediate constriction and subsequent rejuvenescence (Webb and Yancey, 2010).
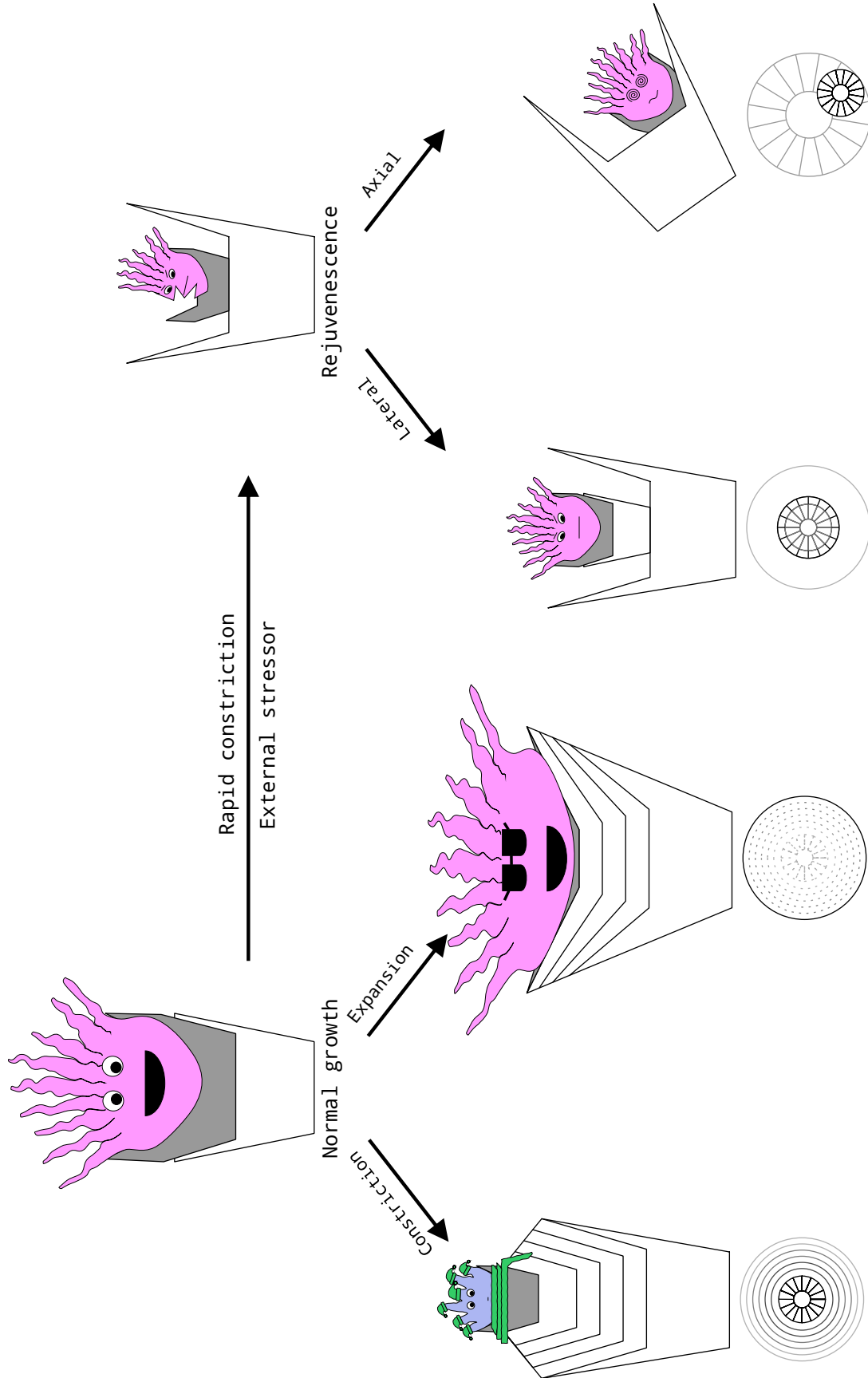
Figure 3.6: Coral polyp response to changes in environment, reflected in skeletal shape. (L) In normal growth, the polyp gradually contracts and expands based on seasonal temperature, maximum and minimum annual skeletal diameter occur in summer and winter, respectively. (R) Rapid constriction is brought on by sudden environmental stress, such as predation or toppling due to storms. The polyp retracts into the existing calice and can return to normal growth (rejuvenescence). Axial rejuvenescence maintains the original growth axis, whereas lateral rejuvenescence results in a change in growth direction, modified after Berkowski (2011).

Both modern and fossil corals show ecophenotypic variation, in which individuals of the same species exhibit different external growth forms along an environmental gradient, such as increasing depth outwards from a carbonate platform (Scrutton, 1996). This also occurs within a colony, as different regions are subjected to slight different water current, nutrient and light availability, and space. Corals will even commonly change growth form when transplanted to a different environment (Veron, 2011). This complicates the study of fossil specimens, and has potentially led to over-classification (Scrutton, 1996). These variations have been observed in a number of living Scleractinian corals, such as *Acropora*, *Porites*, and *Montastraea*. In extinct rugose corals, external curvature and basal broadness are believed to have been partially linked to water current and substrate stability, as they increased the polyp's ability to remain upright, similar to a snowshoe (Figure 3.7) (Scrutton, 1997; Sorauf, 2001).
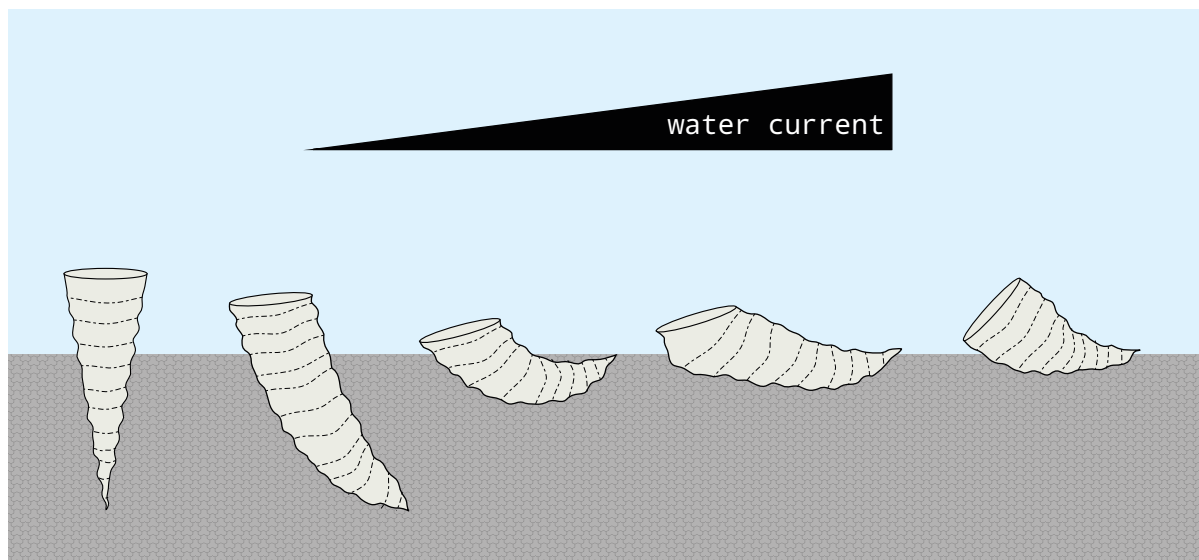
Figure 3.7: Rugose coral growth form is believed to have been controlled by water current, with the coral requiring increased curvature with current as the polyp strove for an upright orientation, modified after Scrutton (1997).

Growth rate also varies with coral lifestyle, with colonial corals growing much slower than solitary species (Figure 3.8). Not only do individuals within colonies have less access to nutrients than solitary species, the two main threats to corals are predation and strong currents, particularly during storms. Solitary corals tend to be larger and more robust to increase stability on soft sediment and guard against predators. Colonial corals tend to grow slower and have a more delicate structure, as they are protected by their massive colonial structure, which minimizes the importance of increased size for the individual. Colonial rugose corals commonly show a branching, fasciculate growth form, as new larvae attached to and cannibalized pre-existing coral skeletons (Scrutton, 1998). Additionally, differences in growth rates between species can influence the shape and definition of growth features. Slower growth will produce narrower, shorter ridges, while rapid growth will produce thicker ridges.
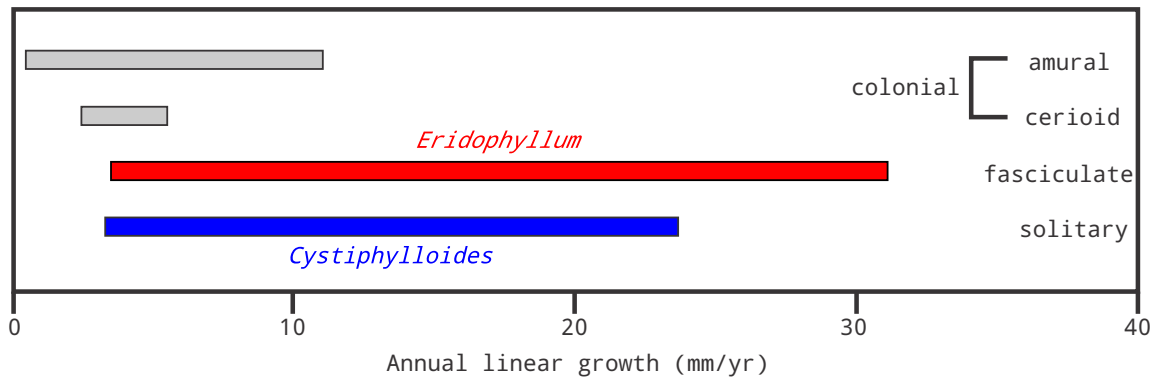
Figure 3.8: Coral growth rate varies with lifestyle. Larger corals have increased survivability; solitary species grow rapidly to achieve a large individual size, whereas the colonial species grow slowly as they are protected by their massive colony, modified after scr.

Chapter 4

Materials and methods

This chapter introduces the sampling and the methods used in this work, following a workflow model based on previous work by Sun et al. (2002), and outlines a general method for the analysis of digital images of paleoenvironmental records, such as coral growth bands and tree rings (Figure 4.1).

```
┌─────────────────┐   ┌─────────────────┐   ┌─────────────────┐
│     Sample      │   │     Image       │   │     Data        │
│ collection and  │   │  processing     │   │   analysis      │
│  preparation    │   │                 │   │                 │
└─────────────────┘   └─────────────────┘   └─────────────────┘
        │                     │                     │
┌─────────────────┐   ┌─────────────────┐   ┌─────────────────┐
│     Sample      │   │     Image       │   │ Coral-ate with  │
│   selection     │   │  Collection     │   │ paleoenvironment│
└─────────────────┘   └─────────────────┘   └─────────────────┘
```
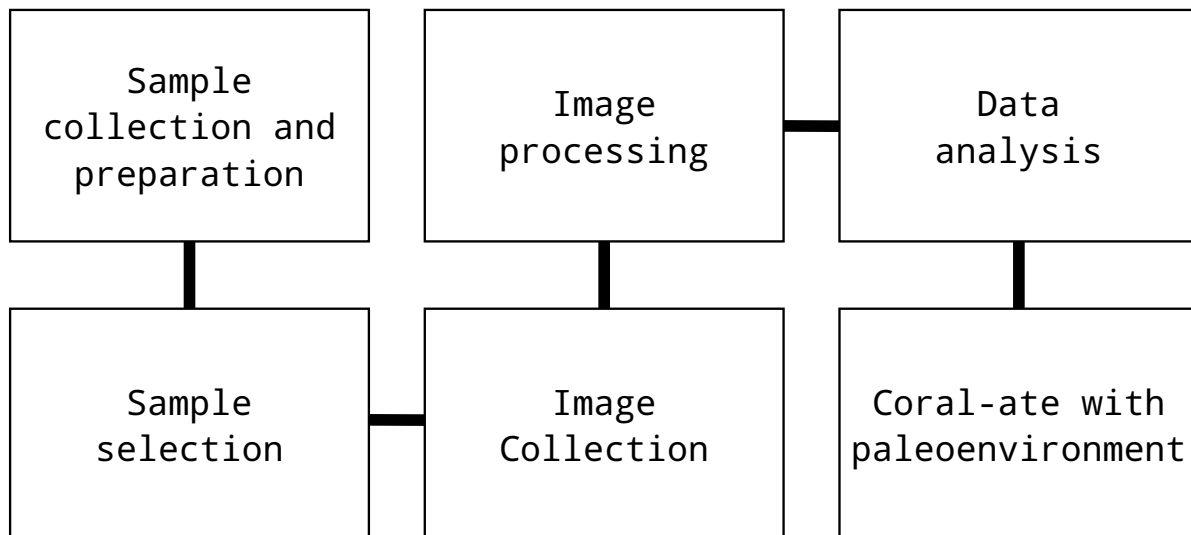
Figure 4.1: Investigation of coral growth ridges workflow, modified after Sun et al. (2002).

4.1   Sample selection and preparation

Specimens of rugose corals, *Eridophyllum subcaespitosum*, *Cystiphylloides americanum*, and *Heliophyllum halli* (Figure 4.2), were collected by Dr. Cameron Tsujita from the Ausable River outcrop of the Middle Devonian Hungry Hollow Member, Widder Formation, at quarry and riverbank exposures at Hungry Hollow (Arkona area), Ontario, approximately 50 kilometres west of London, Ontario. Specimens were selected for preservation quality of growth ridges in the epitheca, as the carbonate mud matrix limited analysis in the field. Specimens were lightly cleaned using a toothbrush, then placed in an ultrasonic bath to remove adhering matrix material.

Figure 4.2: Assorted Middle Devonian Hungry Hollow rugose coral specimens before cleaning. (A) *Eridophyllum subcaespitosum*; (B) *Cystiphylloides americanum*.

Optical microscopy was then used to select the samples based on preservation of the finest

scale growth ridges visible. In addition, growth curvature marked by geniculations (due to

changes in growth direction as a result of storm events), was avoided as it can lead to ridge

information loss (Flude, 2005). Specimens with few geniculations were chosen to allow for

the best approximation of growth axis and minimal loss of growth information, as well as to

allow for correlation between ridges across the diameter of the specimen. Samples of species

were chosen: the colonial *Eridophyllum*, and the solitary *Cystiphylloides* and *Heliophyllum*,

to study any potential impact of lifestyle on growth ridge formation (Figure 4.3).
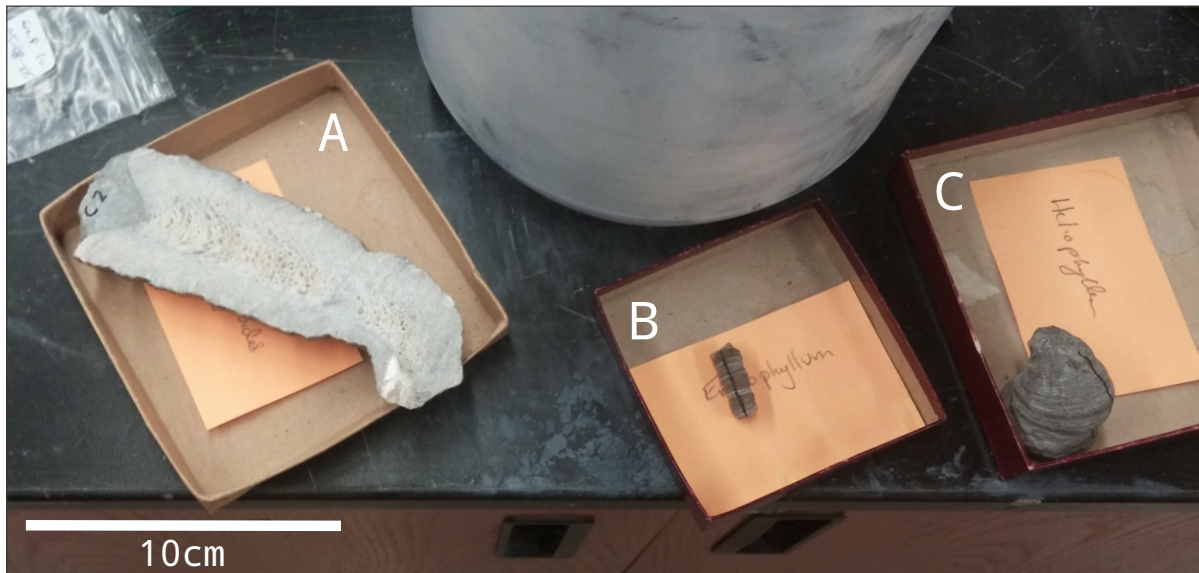
Figure 4.3: Cleaned rugose coral specimens selected for analysis. (A) *Cystiphylloides*; (B)
       Eridophyllum; (C) *Heliophyllum*.

4.2 Image acquisition

4.2.1 Micro-CT imaging

The two specimens with the most well-defined growth ridges observed by optical microscopy, (*Eridophyllum* and *Cystiphylloides*) were scanned using a Nikon XTH 225 ST Micro-CT scanner at 125kV (Figure 4.4), by Dr. Andrew Nelson (Sustainable Archaeology, The University of Western Ontario) to preserve the 3-dimensional structure before destruction with the creation of thin sections. Additional process information listed in Appendix A. This could potentially allow for correlation across the growth axis, as well as a correlation between internal features and the external growth ridges.

Figure 4.4: Nikon XTH 225 ST Micro-CT scanner, operated by Dr. Andrew Nelson (Sustainable Archaeology, The University of Western Ontario).

X-ray computed tomography (CT), commonly used in medicine, is a non-destructive imaging method used to produce a complete three-dimensional model reconstruction of an object. Micro-CT imaging uses the same principles to image a sample down to micron scale. The X-ray micro-CT instrument consists of an X-ray emitter, stage, and emission collector (Figure 4.5). The sample is placed on a rotating stage, with its long axis parallel to rotation,

and images are captured at set intervals as the specimen rotates (Stauber and Müller, 2008).
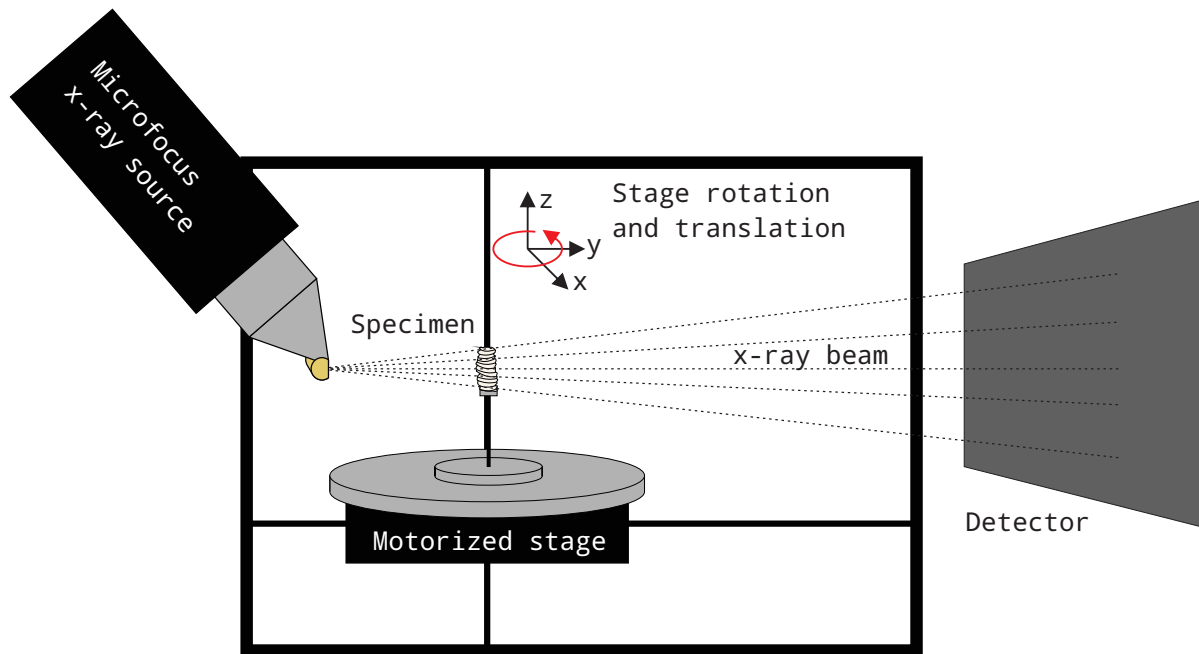
Figure 4.5: Schematic diagram of Micro-CT scanning. A motorized stage can move the specimen in three dimensions, optimizing output resolution, modified after (Stauber and Müller, 2008; Lee et al., 2003).

The output resolution is inversely proportional to the sample size, as the emitter and detector are stationary. The Nikon XTH 225 ST scanner features a motorized stage, which can move the specimen in three dimensions, to find the ideal distance from the detector, optimizing the output resolution for each sample. This produces a series of slices which are combined using computer software, typically proprietary and bundled with the scanner, to form a 3D model reconstruction (Figure 4.6). The process is operator-intensive; various parameters must be optimized to produce the best possible digital representation of the sample. X-ray energy level is an important factor in CT: lower energies provide higher contrast, whereas higher energies penetrate the sample further. There is also a trade-off between image quality and scan time: more image slices produce a higher quality image, but increase scan duration (Stauber and Müller, 2008).
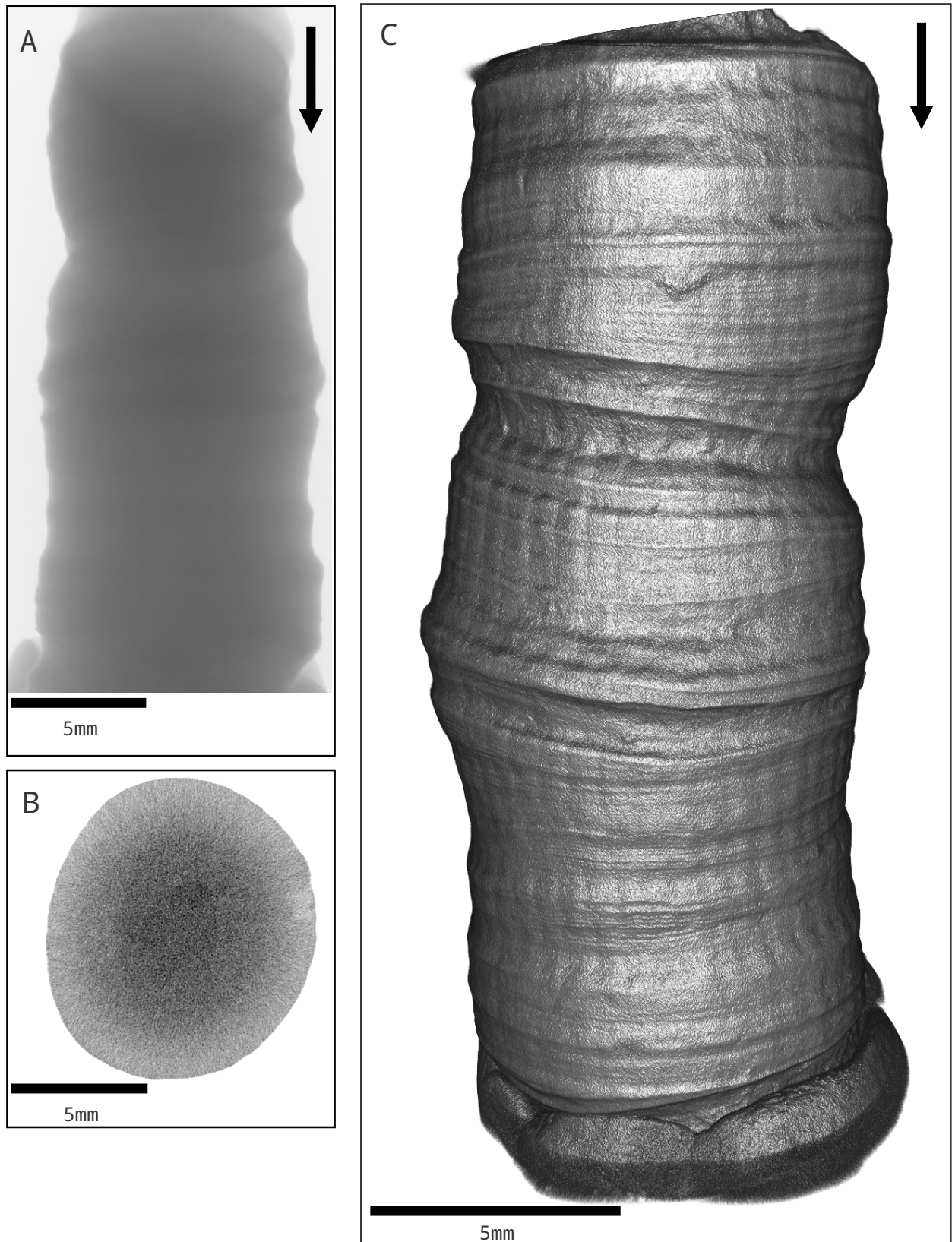
Figure 4.6: Micro-CT output, arrow indicates growth direction, consistent with scan orientation. (A) Original Micro-CT scan component image; (B) horizontal DICOM slice; (C) three-dimensional rendering of *Eridophyllum*.

4.2.2   SEM imaging

An approximate growth axis was marked by visually estimating a longitudinal slice through

the centre of the specimen, represented by a line slicing through the centre of the diameter at

each point to follow any bends or deformities. Thin sections were made by Steve Wood (The

University of Western Ontario), by slicing the samples longitudinally along that axis, mount-

ing the cut face down in epoxy, then grinding the top surface until flush. The samples were

then carbon-coated, in preparation for Scanning Electron Microscopy (SEM) imaging. SEM

uses an electron gun and a series of lenses to fire a precise targeted beam of electrons at a

specimen, which then interacts with its atomic structure, causing it to emit electrons (Figure

4.7). These can be collected to produced a digital image of the specimen, detailing topogra-

phy or chemical composition (Prior et al., 1999).
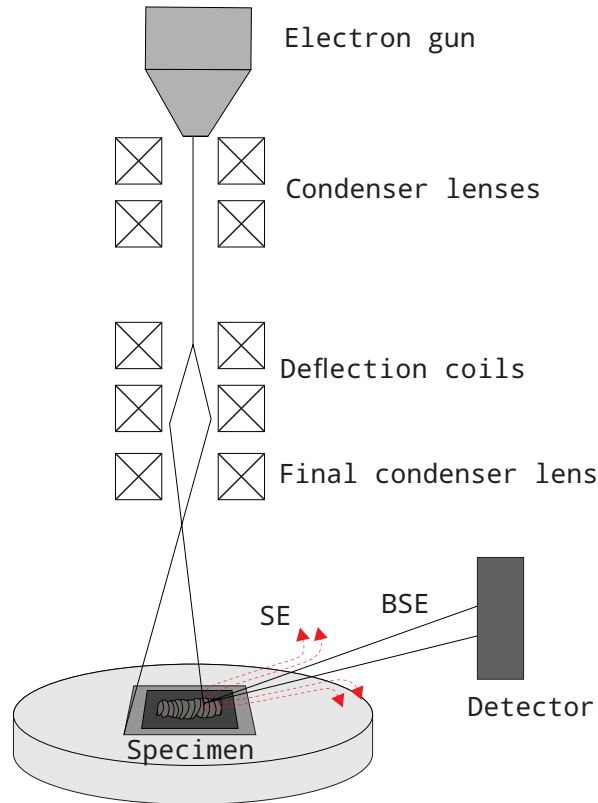
Figure 4.7: Scanning electron microscope schematic, modified after Postek (1997).

SEM can provide details on physical and chemical structure of a material, down to the nanometre scale. Two types of emitted electrons are collected: secondary and backscattered electrons. Secondary electrons (SE) are emitted at random angles from the specimen as the electron beam interacts with the outermost 10-50 nanometres of its surface. They have the potential to provide the highest resolution images, though the composite signal they produce can be difficult to decipher, as it is strongly influenced by composition and geometry. Backscattered electrons (BSE) are highly directional and travel in a relatively straight line from the primary beam at the surface of the specimen to the detector and provide a topographic image at 100-500x the resolution of standard optical microscopy as well as structural or chemical details (Postek, 1997, 1988).

The two best preserved samples (*Eridophyllum* and *Cystiphylloides*) were imaged on a Hitachi SU6600 FEGSEM by Ivan Barker (ZapLAB, The University of Western Ontario), using backscatter scanning electron (BSE) microscopy. Both complete longitudinal edges of *Eridophyllum* and a small length of *Cystiphylloides* were scanned (Figure 4.8). Micron-scale component images were output, which required the application of image stitching methods to produce a composite of the entire scan area (Figure 4.9).
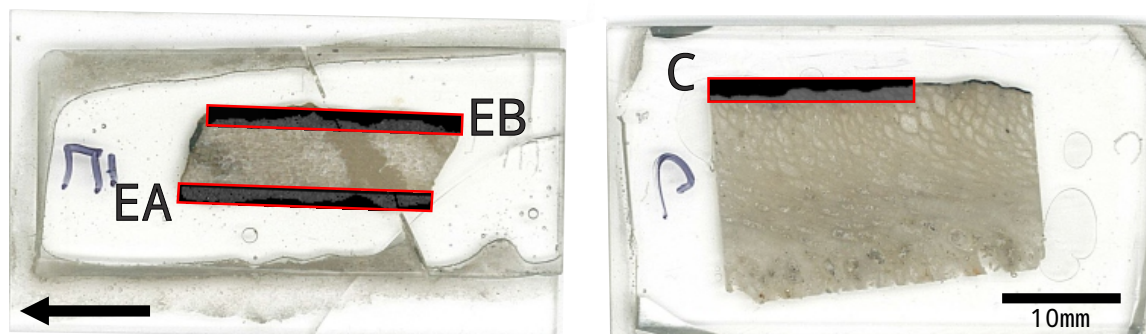
Figure 4.8: SEM scan regions of thin sections of (L) *Eridophyllum* and (R) *Cystiphylloides*.

Eridophyllum B edge SEM scan

Component images	
Number:	774
Rows:	9
Columns:	86
Component resolution:	1024 x 768
Component FOV:	250 µm

Stitched Composite	
Resolution:	85350 x76363
Dimensions:	21.40mm x 1.85mm
File size (TIF):	599 MB

5mm

EB

EB_086

100µm
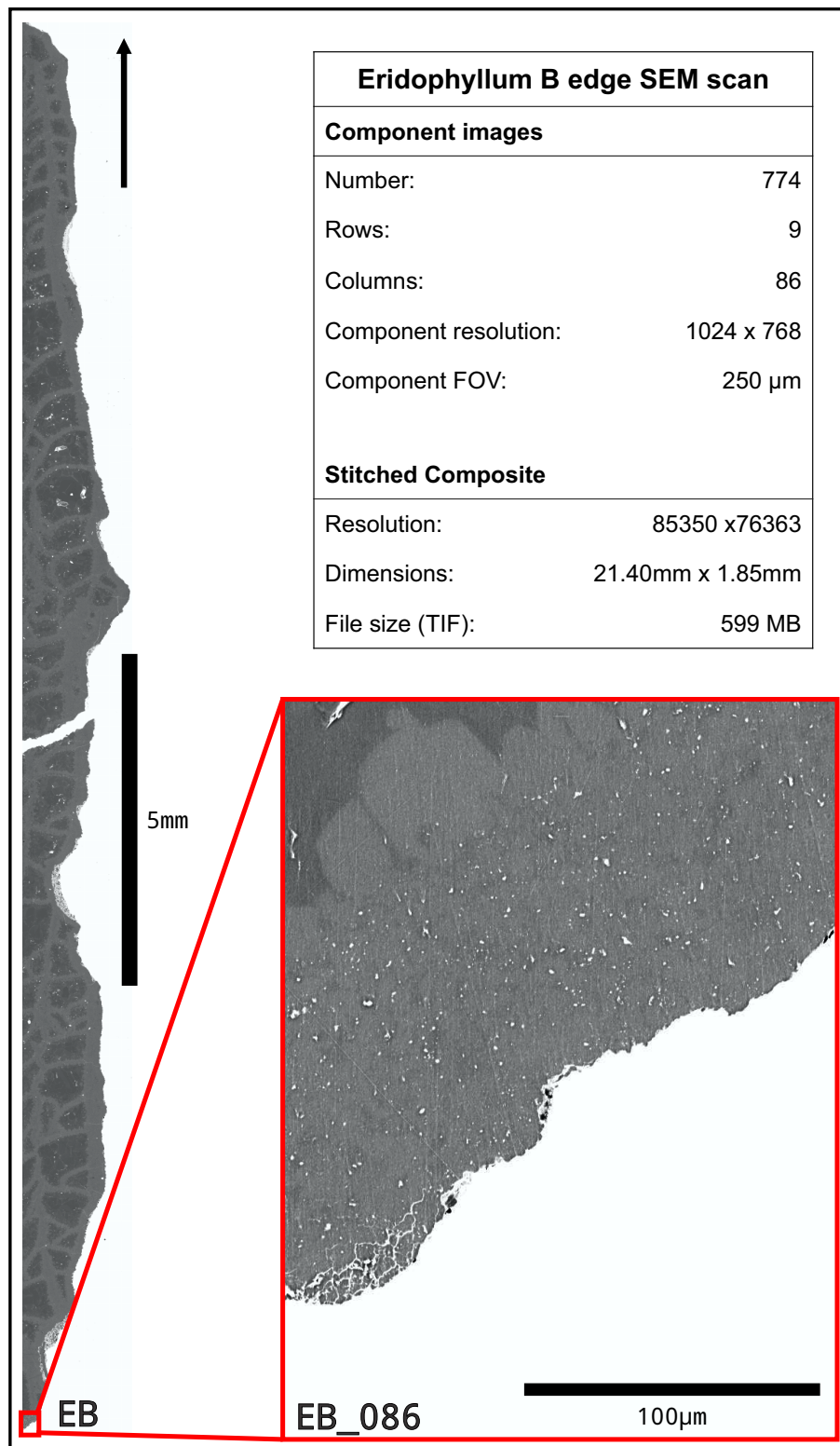
Figure 4.9: SEM component image output data, with *Eridophyllum* B component size compared to stitched composite; approximately eight months of growth represented.

4.3   Image Processing

Digital imaging captures an optical signal and stores it in a two-dimensional matrix. Each cell, known as a pixel, has an assigned intensity value based on the sensors interpretation of the real-world sample. Greyscale images are represented by a single array, or channel, of values ranging from 0 to 255, whereas colour images have three channels, red, green, and blue (Figure 4.10). This allows images to be imported as simple array structures, easily modified by mathematical operations (Burger and Burge, 2009).
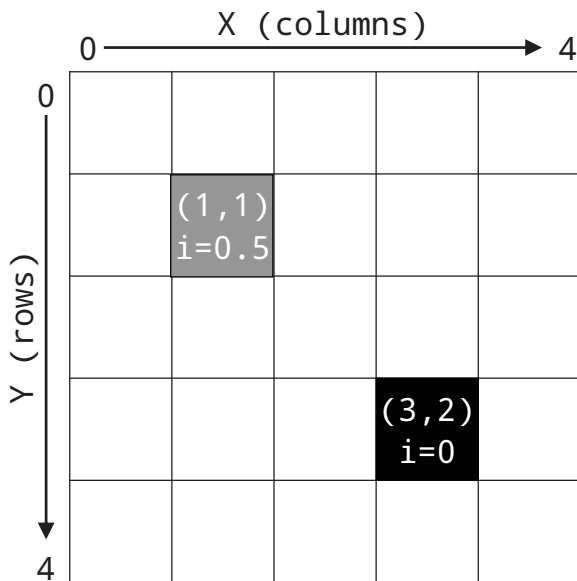
Figure 4.10: Image data structure as a two-dimensional matrix. X and Y coordinates represent width and height, and the value represents an intensity value. A greyscale image is a single array of intensities, whereas colour images are multi-channel, with an array representing each component colour value (red, green, blue), modified after Burger and Burge (2009).

Image stitching is required in digital imaging when there is a difference in scale (often an order of magnitude) between the area of interest and the field of view (FOV) of the capture device (Blattner et al., 2014). The standard method matches pixel values between two images, whereas feature detection searches for similar shapes between image pairs. Useful for standard panorama applications, images are transformed (rotated, scaled, distorted) and globally placed to produce the highest quality result (Figure 4.11). In microscopy, the sample is mounted on a motorized stage, which moves in discrete steps in X-Y space. At each step, the

sample is imaged, with a slight overlap, producing a grid of images. Due to mechanical accuracy limits, this grid is slightly skewed (Figure 4.12) (Majurski et al., 2016; Preibisch et al., 2009).
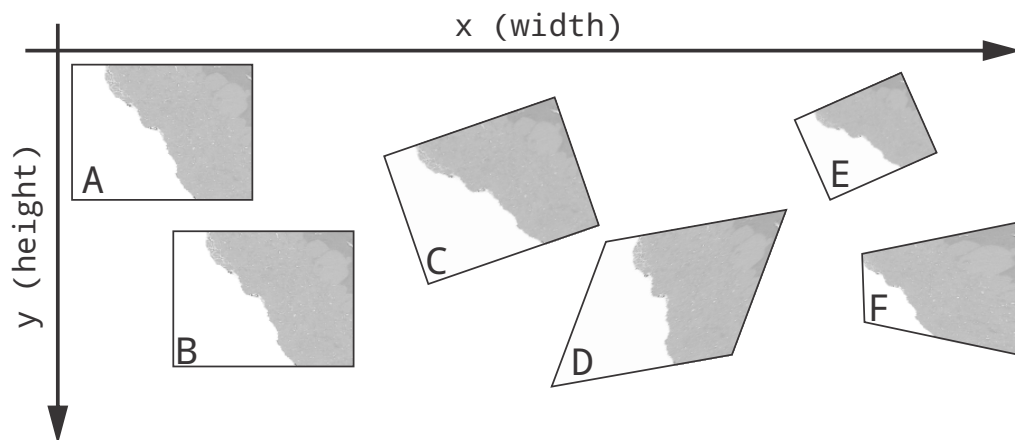
Figure 4.11: Basic two-dimensional transformations performed by image stitching software. (A) original image; (B) X-Y translation; (C) rotation, (D) affine transformation; (E) similarity; (F) perspective. As SEM stage movement is known and consistent, only translation is desired, modified after Szeliski (2006).
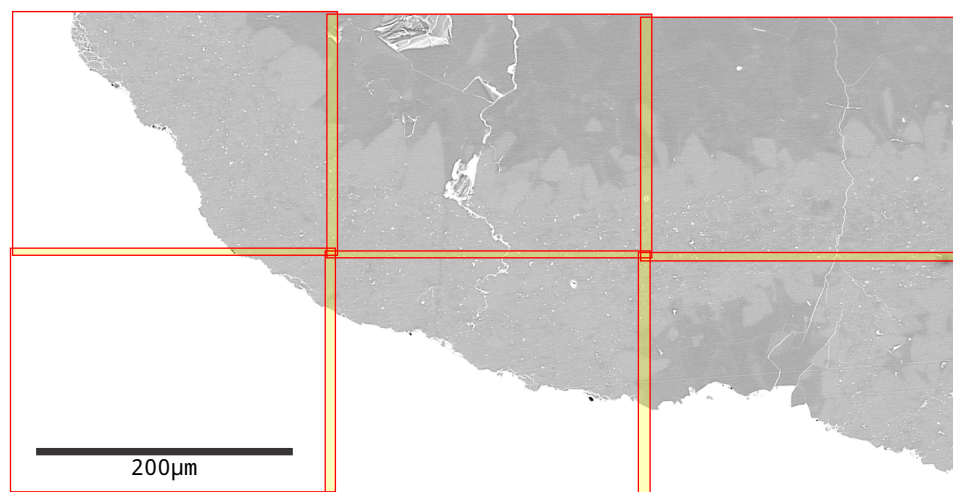
Figure 4.12: Sample *Eridophyllum* image grid output by SEM, skewed due to mechanical limitations of the motorized stage. Image boundaries are outlined in red, whereas overlapping areas are shaded yellow. Corners of 4 adjacent images do not completely match up, as in the case of a perfect grid.

4.3.1 Tools used

In this work, Fiji, an open source, scientific distribution of the Java-based ImageJ program was used for preliminary image assessment, scaling, and stitching (Schneider et al., 2012; Schindelin et al., 2012). All image processing steps were developed in the Python 3.6 programming language (Lutz, 2013). The open source computer vision library, OpenCV (Bradski, 2000) was used to process the raw images and extract an edge line, and the scientific computing library, SciPy (Jones et al., 2001), was used for signal processing. Code was written in the PyCharm Educational Edition IDE, on a Windows 10 PC with an Intel i7 6700K processor, 32GB RAM, and a 6GB Nvidia GTX-1060 graphics card. Due to the computational demand of high resolution images, the procedure was developed using smaller test sections of the composite. The method was then applied to the entire sample image in sections. All figures were produced with the matplotlib library, a Python implementation of the MATLAB plotting environment (Hunter, 2007) All code is available in Appendix B .

4.3.2 Image stitching

Initial stitching attempts with traditional stitching software such as Microsoft Image Composite Editor and the open source PanoTools, produced ghosting artefacts in the resultant composite images (Figure 4.13). These programs, designed mainly for panorama stitching, transform and globally place images, making them unsuitable for images with poor, repeating features, or repeated stage translations with small overlap (Szeliski, 2006). Manual image placement by hand, using CorelDRAW X7, proved to be time intensive and could not account for edge distortion, which led to poor matches between diagonally adjacent images.
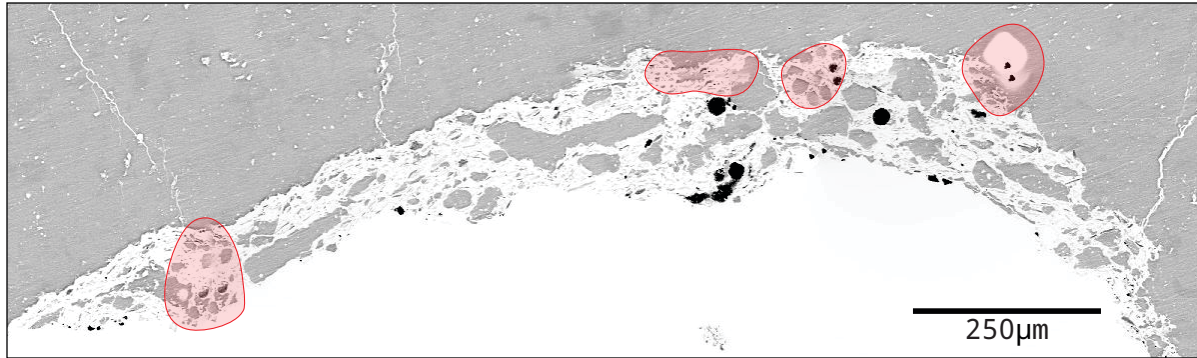
Figure 4.13: Image stitching artefacts in Microsoft Image Composite Editor output in red. Components were not aligned properly and blurred as a result.

Next, the built-in Fiji stitching plugin was tested, which uses Fourier transform phase correlation to find the best possible translation between each component image pair (Preibisch et al., 2009). It assumes an approximate grid input, but can stitch images without a known configuration as well. This can lead to issues in feature-poor images; however, as it will attempt to find a better match and globally place and transform those images, disregarding the original grid configuration. As our coral SEM scans are quite feature-poor, particularly internally, this method was unsuitable, as it produced an image with major stitching errors that did not follow the known tile configuration.

In an attempt to prevent the global relocation of images, invariant feature matching was applied to common image borders in adjacent images only, determined by the known grid configuration and overlap. The initial design stitched images in columns, then combined them to form an entire image. Included in OpenCV and developed by Lowe (2004), invariant feature matching detects keypoints in images, then assesses their match based on their properties such as direction, distance, and scale. However, this was computationally inefficient and did not account for edge distortion, which led to similar issues as the manual method. Attempts to account for distortion proved well beyond the scope of this thesis.

The final algorithm tested was the Microscopy Image Stitching Tool (MIST), by the National Institute of Standards and Technology. A MATLAB/FIJI plugin, MIST is designed to stitch two-dimensional, feature-poor, greyscale microscope images, with a known, consistent stage repeatabilty and overlap, though to date, usage has been limited within paleontological studies (Blattner et al., 2014). It uses Fourier transformations to find the relative placement of each pair of adjacent images, within the known grid configuration, preventing global displacement. Fourier transforms excel at detecting features in fairly isotropic images (Chalfoun, 2014). The three phases are: detecting image translations, optimizing them, and finally combining them into a stitched composite. Each image is assigned X-Y coordinates representing the overall placement in the stitched composite, as well as a series of relative, acceptable, translations from the nearest north and west neighbours, along with a correlation factor. These are then optimized using the estimated stage repeatability to remove the matches which do not conform to the original grid configuration (Majurski et al., 2016). As an added bonus, because each image pair is processed individually, it is computationally efficient, which is beneficial for large images (Chalfoun, 2014). This method was ideal for this thesis and produced the highest quality results, with minimal stitching artefacts (Figure 4.14).
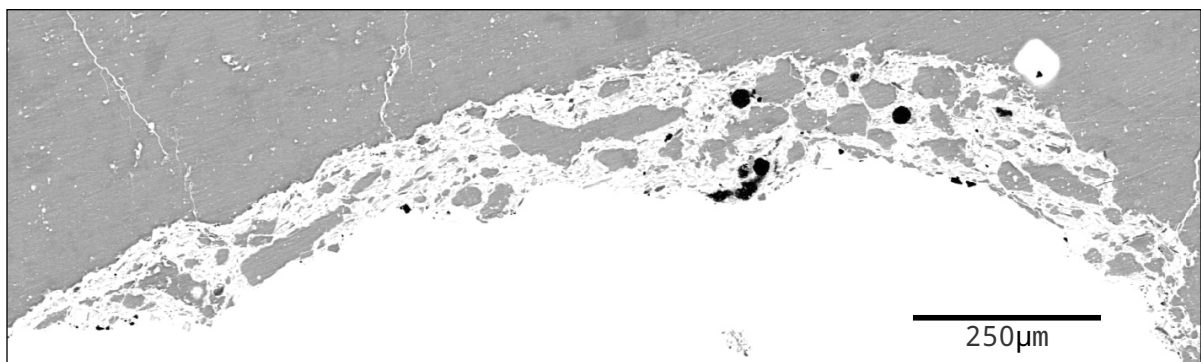
Figure 4.14: MIST produces composite images with limited stitching artefacts.

4.3.3   Image processing and coral slice edge line extraction

The goal of this stage was to extract from the composite SEM mosaic a line representing

the outline of a longitudinal cross-section of the epitheca. This allows for the application of

data analysis and statistical methods to the features of the line which represent coral growth

stages at various scales (Figure 4.15). This section details the methods, using a small sample

of *Eridophyllum* (Figure 4.16).

Image stitching	Image contouring	Median filtering
Bilateral filtering	Image thresholding	Export edge line
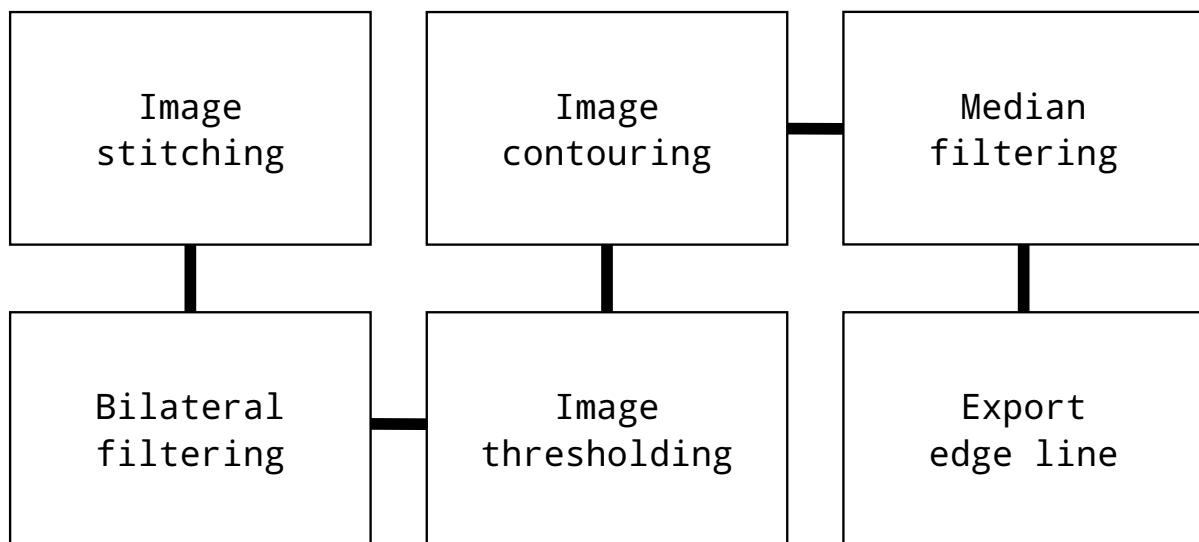
Figure 4.15: Image processing workflow.
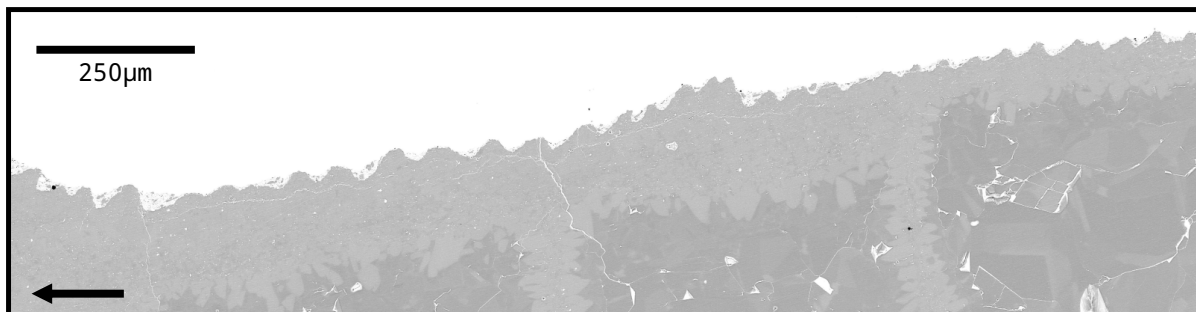
Figure 4.16: Example *Eridophyllum* B section original image.

Contrast equalization

The first step was to normalize the image contrast by widening the histogram of pixel values without changing the original edge data. This improves the image processing efficacy, as there is a wider range/distribution of values with the image histogram being spread across the entire available range of pixel values. This method retains the integrity of the original data, by essentially increasing the spacing between histogram bins without interpolating in-between (Burger and Burge, 2009). Adaptive Histogram Equalization (AHE), used heavily in medical imaging, equalizes contrast using an adjustable window to apply a correction algorithm proportional to neighbouring pixel values. In isotropic regions with a low range of pixel values, AHE will map narrow, high peaks to wider ranges, enhancing image noise, represented by small deviations in pixel values. To attempt to minimize this side effect, Contrast Limited Adaptive Histogram Equalization (CLAHE) limits contrast enhancement of high frequency values within a region, clipping high peaks in the histogram (Pizer et al., 1987). CLAHE is often applicable to SEM images, due to their wide-peaked, bimodal distribution (Figure 4.17).
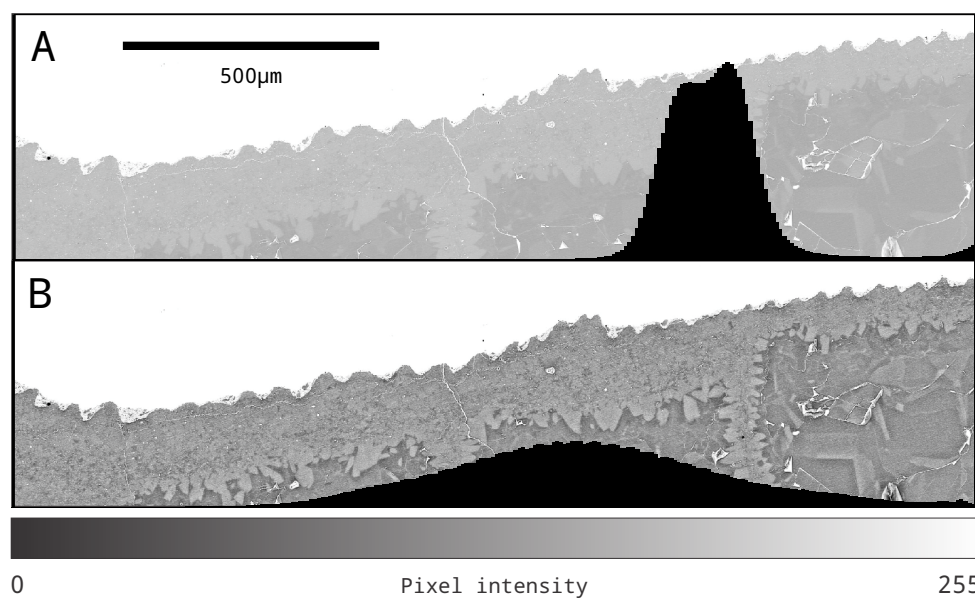
Figure 4.17: Histogram of pixel intensities for sample image (A) before and (B) after clipped adaptive histogram equalization. The histogram is equalized, but the number of bins and their frequencies remains constant.

Bilateral Filtering

As the objective of this thesis is to measure and quantify the external growth ridges, represented by an edge line in an SEM scanned image, any image processing applied must minimize edge distortion. SEM images tend to be noisy as a result of their high resolution. Pixels in an image will have a difference in pixel intensities, (σ_r), as well as a distance spatially (σ_d). These are known as similarity and closeness, respectively. Standard Gaussian algorithms are domain-only filters; pixels within the chosen kernel window are blended, purely based on spatial distance, regardless of individual pixel intensity. This method reduces noise by essentially averaging pixel intensities over a larger resolution than the noise, which makes it computationally simple, but it suffers from blurring of edge features, as typically represented by large differences in pixel intensity, making it unsuitable for this application (Tomasi and Manduchi, 1998). Various image filtering techniques were tested during the development of this method to reduce noise while best preserving the original image data (Table 4.1).

Unsharp filter	sharpened edges of image noise and artefacts; particularly poor due to JPEG compression
Gaussian filter	blurs entire image evenly, regardless of pixel intensity; reduced image noise, but blurred epithecal edge
Bilateral filter	blurs image using both spatial and pixel intensity similarity; reduced image noise while preserving edges
Median filter	assigns median value of surrounding pixels to target; reduced signal noise of epithecal edge, preserved trends mean filter
Mean filter	assigns mean value of surrounding pixels to target; assigns non-binary pixel intensities (grayscale), requires subsequent re-thresholding

Table 4.1: Various image filtering techniques considered during method development.

Bilateral filtering works in both the range and domain, blending pixel regions based on both spatial closeness and intensity similarity. More isotropic areas are blended together, whereas large differences in pixel intensity typically signal a change in region (Figure 4.18). Where pixel values are similar, it acts as a domain filter to smooth noise, but if a sufficient change is detected, the bilateral filter will not blur across the boundary. The three parameters are: kernel size, domain spread (acceptable distance between pixels), and range spread (acceptable difference between intensities) (Tomasi and Manduchi, 1998). These properties make it useful for bimodal images, where there is a large contrast between regions, such as these SEM coral scans (Figure 4.19).

Figure 4.18: Gaussian filtering blends the entire image evenly, whereas bilateral filtering blends regions based on spatial and intensity sameness, resulting in decreased noise with preserved edge features. (A) unfiltered sample region of *Eridophyllum*; (B) Gaussian (σ_d=5) filtering applied; (C) Bilateral filtering (σ_d=5, σ_r=75) applied.
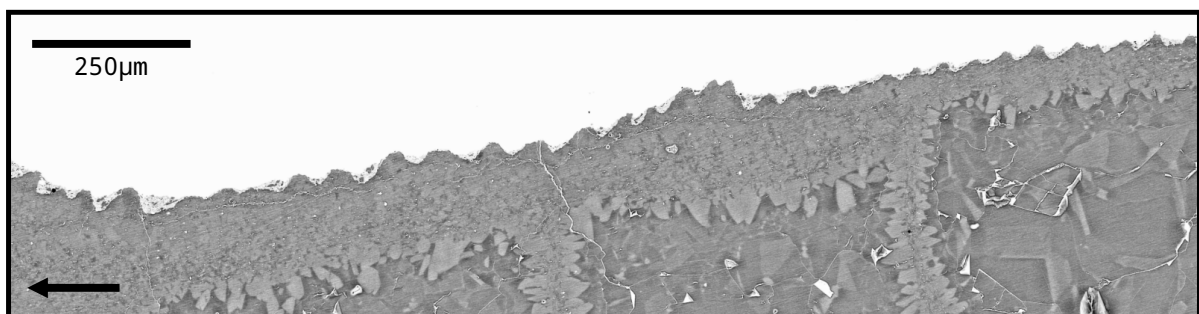
Figure 4.19: Example *Eridophyllum* B section after contrast enhancement and bilateral filtering.

Image segmentation

Image segmentation divides similar image regions into clusters (Haralick and Shapiro, 1984). The first step is image thresholding, which extracts image features from the background by converting it to binary. This is based on pixel intensity; all values above the chosen threshold are made white, whereas all below the threshold are made black. However, as mentioned in Sun et al. (2009), this value is typically chosen by visual analysis in an attempt to find a value that best represents the overall shape. As the distribution of pixel intensities increases, it becomes more difficult to define this value. Otsu's (1979) thresholding removes that uncertainty by automatically selecting an optimal threshold value in greyscale images, where histogram variation is not two clearly defined, sharp peaks. It selects the threshold value which best separates the grey classes of the image, while remaining computationally simple (Otsu, 1979) (Figure 4.20).
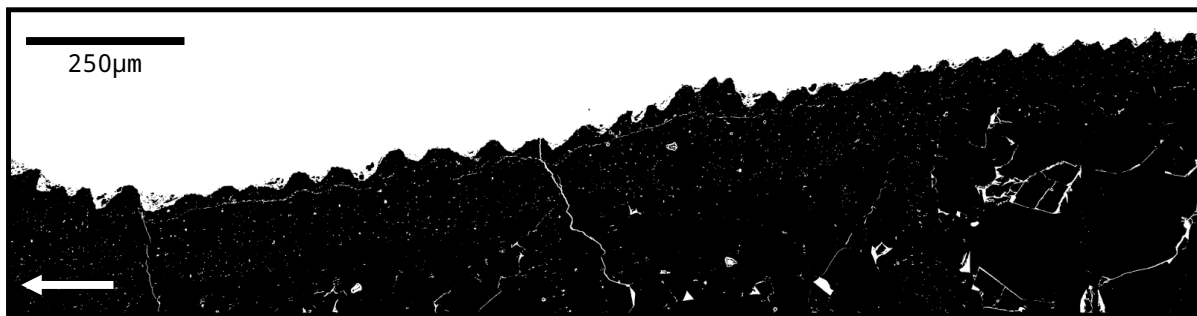
Figure 4.20: Example *Eridophyllum* B section converted to binary through Otsu's image thresholding.

Small holes in the binary image were filled by dilating then eroding the image. The image was then contoured, which records pixels adjacent to the background value to outline features as discrete shapes (Burger and Burge, 2009). As the longest contour represents the largest region in the image, these data points were isolated to extract only the main body of the coral sample (Figure 4.21).

Figure 4.21: Main coral body extracted from example *Eridophyllum* B section by contouring the image and isolating the longest object outline.

Median filtering

Due to the resolution and file type compression, the signal still has a large noise component, which must be smoothed somewhat to optimize peak detection. Median filtering, which reduces noise while preserving trends, assigns the median value of the surrounding pixels within a sizable window, to the centre target (Yin et al., 1996) (Figure 4.22).
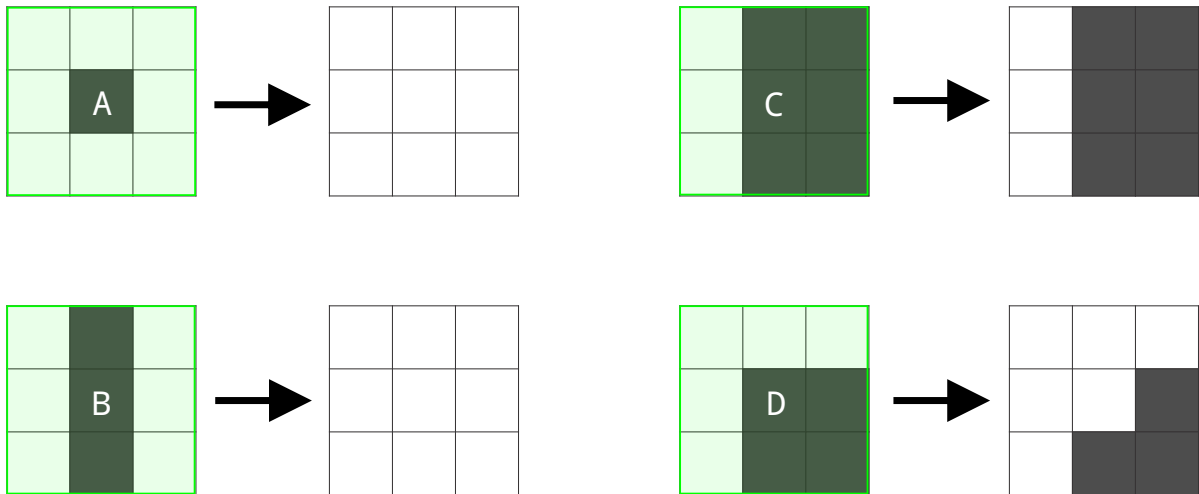
Figure 4.22: Median filtering performed on an image, illustrating how different signal types react to a 3 x 3 kernel size (shown in green). (A) single pixels are assigned the value of its neighbours; (B) thin lines are removed, assigned the median value of the surrounding pixels; (C) thick lines are preserved; (D) hard corners are smoothed, as light pixels outnumber dark pixels surrounding the centre, the target is assigned a light value, modified after Burger and Burge (2009).

In the case of images, this steps through each pixel, assigning it the median intensity of the surrounding window (Burger and Burge, 2009). Kernel size is an important factor in signal processing; to ensure minimal alteration of the overall signal. In this case, the kernel size must be smaller than the smallest scale features, the coral daily growth ridges. This is a useful tool for JPEG images, as it can smooth hard edges created by blockiness (Figure 4.23).
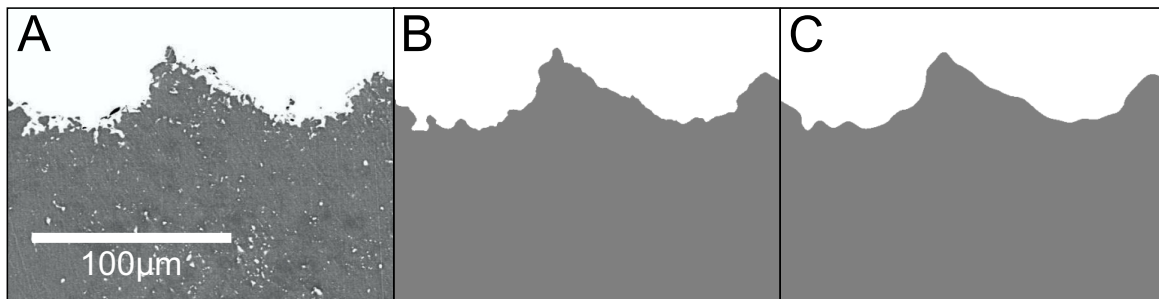
Figure 4.23: Median filtering decreases noise without distorting larger order signal trends. (A) image before thresholding; (B) coral cutout before median filtering; (C) median filtered cutout; signal noise is reduced, overall trends are preserved.

The binary cutout image was median filtered and re-contoured to extract an outline of the smoothed shape representing the solid coral body (Figure 4.24), which was then exported to a plaintext file (.csv) as a set of X-Y coordinates. This line represents the outer epithecal edge, parallel to the growth axis (Figure 4.25).
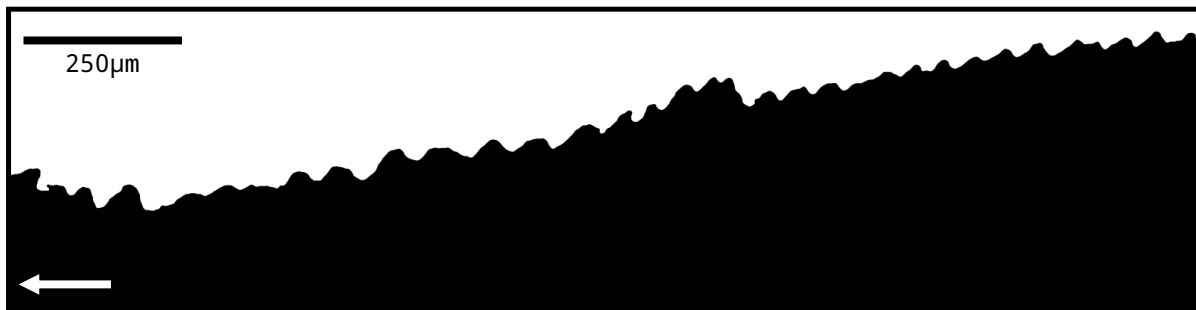
Figure 4.24: Main coral body cutout of example *Eridophyllum* B section after median filtering, to remove noise but preserve overall trends.
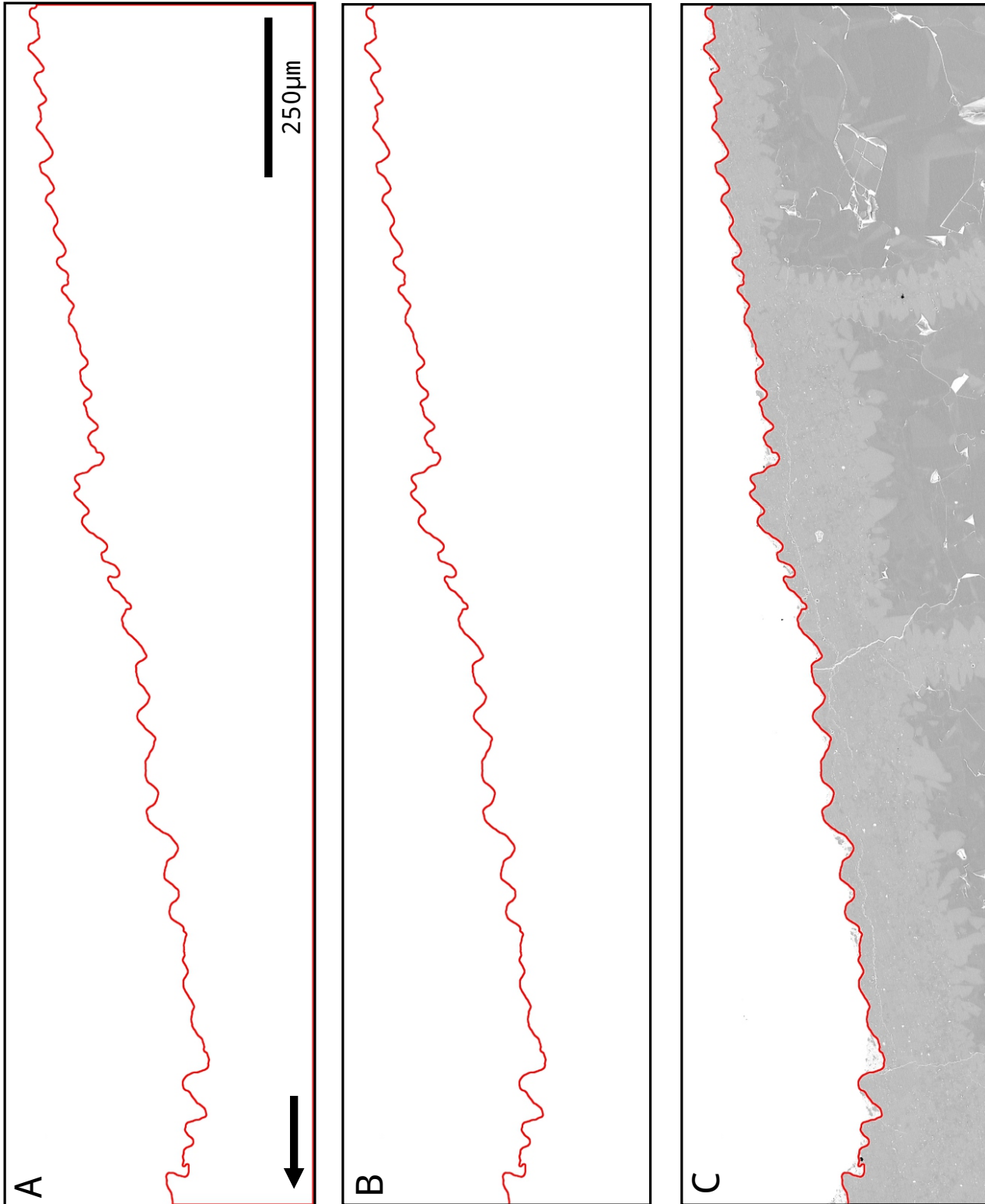
Figure 4.25: Example *Eridophyllum* B section edge line isolation. (A) main coral body outlined through image contouring, including lower rectangular image boundaries; (B) image border coordinates filtered out to extract only the epithecal edge line; (C) extracted epithecal line with original input image.

4.4   Detection of peaks and troughs

The objective of this stage is to select peaks and troughs, represented by local extrema in the edge line previously extracted from SEM images. Two methods were tested: simple local minima and maxima detection, which was heavily dependent on peak width parameters chosen by the operator, which resulted in over or under-detection, and continuous wavelet transform method, which proved adequate. Once peaks and troughs are marked, standard data analysis and geometric methods can be applied to check for patterns in the data (Figure 4.26).
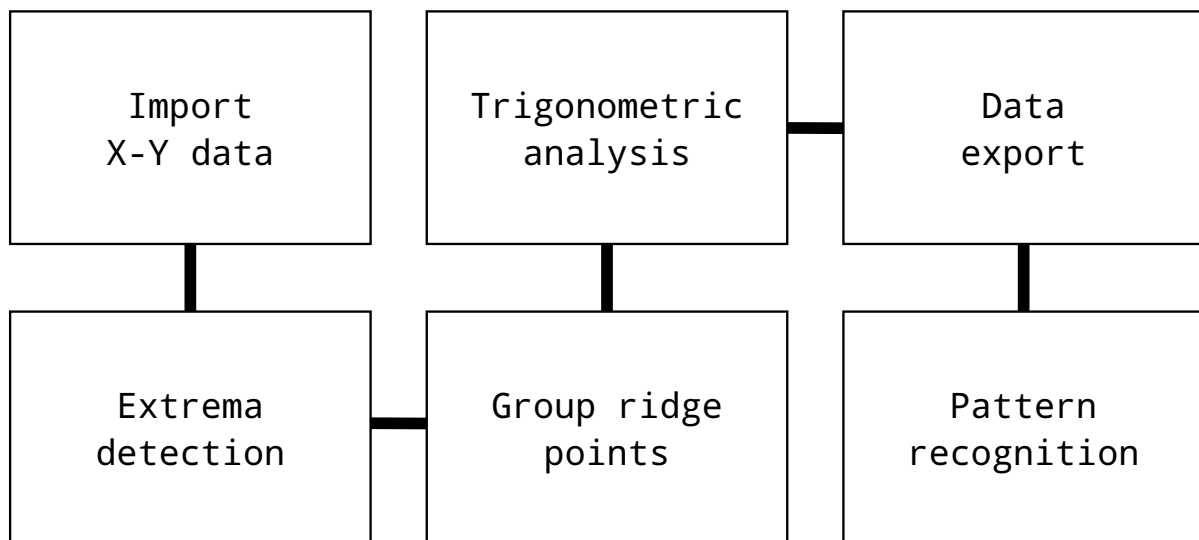
Figure 4.26: Data analysis workflow, from extracted X-Y coordinates of the epithecal edge line to pattern recognition.

The extracted epithecal edge line from the previous section was then imported as X-Y coordinates into an original Python script, developed by the author. In some cases, the text file must be rearranged before importing. Image contouring outlines objects as a closed curve. Indexing of this outline may begin at any point in the curve. When the rectangular boundaries are removed, the contour may be recorded as two line segments. This is easily fixed by transposing the second line segment, marked by a change from maximum to minimum X values, to the bottom of the .csv file, without applying any sorting techniques. This ensures a continuous record for analysis (Figure 4.27).
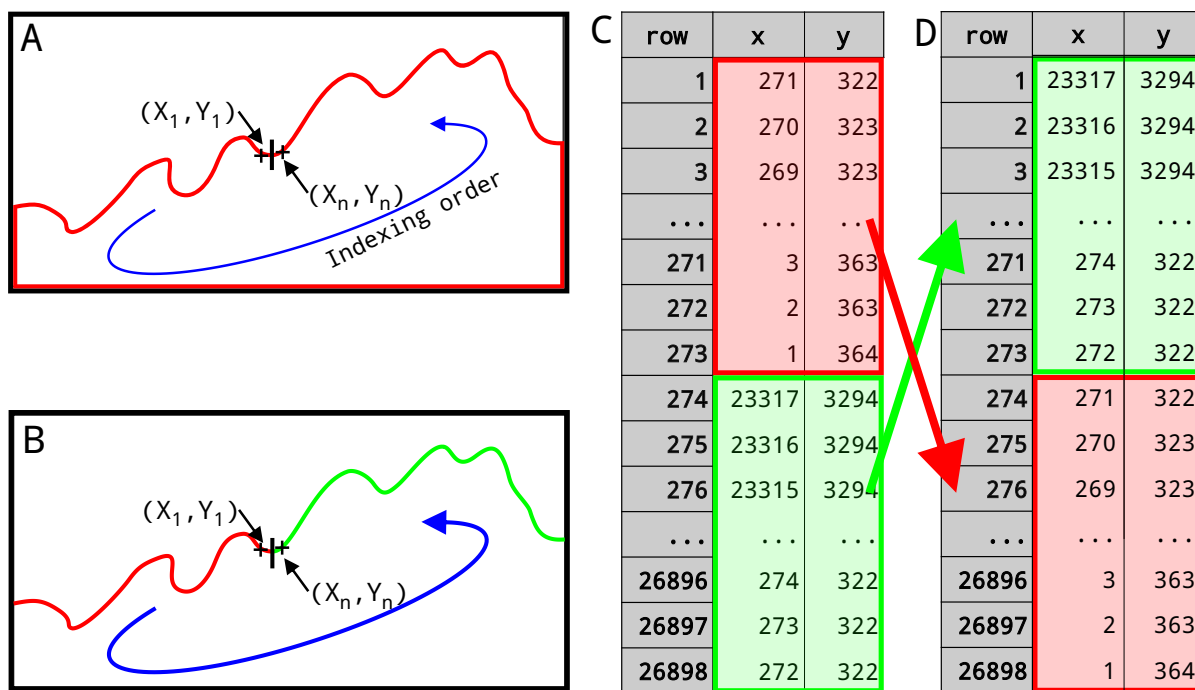
Figure 4.27: The exported line data may be recorded as two separate line segments and need to be swapped in a text editor before import, due to contouring indexing order. (A) original image contour, including image border, beginning at a random point within the line segment; (B) exported X-Y coordinates are rearranged so that they record the extracted line segment in order.

4.4.1 Relative extrema method

The first attempt at peak detection simply moved along the edge line and checked for changes in Y value. It would mark the point where the difference was greater than a constant, predetermined value. This method proved to be difficult to control due image noise. It had issues with flat portions of the image (enhanced by the JPEG compression), either not marking them, or marking them all, requiring them to be filtered out to isolate a single point representing a peak or trough. The high resolution of the images, as well the low height-to-width ratio of the ridges limited the effectiveness of this method (Figure 4.28).
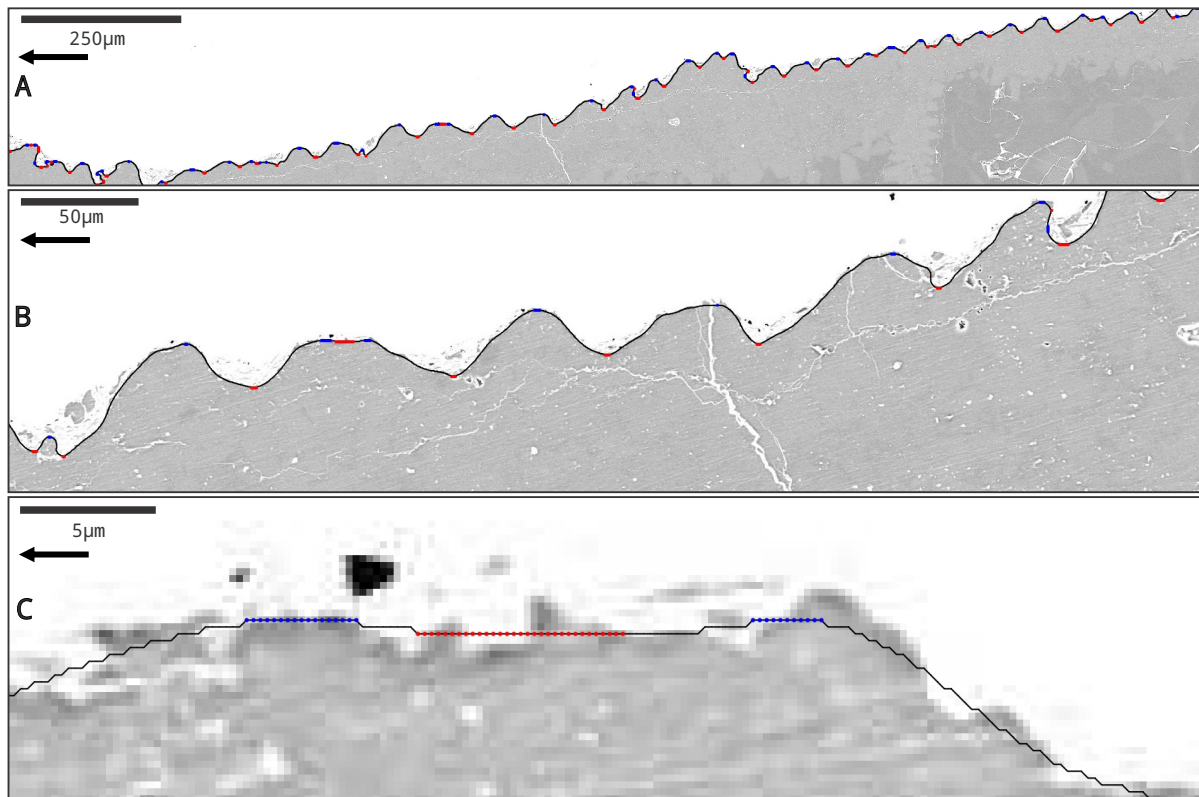
Figure 4.28: Peaks (blue) and troughs (red) marked on an *Eridophyllum* sample region, after application of relative extrema peak detection, highlighting its limitations. Efficacy is operator dependent, with detection sensitivity based on expected peak width. (A) relative extrema peak detection method applied to sample region; (B) closer inspection highlights the inconsistency within detected peaks; (C) in cases where Y values remain constant, consecutive points are marked, requiring extensive post-filtering.

4.4.2   Continuous wavelet transform method

Standard peak detection methods ignore peak shape and require intensive image processing before their use. Images must be filtered to remove noise and a baseline correction applied, which permanently alters the data and can remove, minimize, or blur legitimate signals. An optimal detection window size is set by the operator to limit under and over-detection. If the window is too large, low signals will be missed, and if too small, over-detection of noise will occur. It also does not factor in peak shape, which can be a useful tool when distinguishing signal from noise, as well as detecting peaks of different scales.

Continuous wavelet transform-based peak detection typically does not require pre-processing and is useful for signals with a range of peak scales, as wavelet transformation allows for peak shape analysis (Du et al., 2006, 2007). Due to the resolution and compression issues associated with the JPEG input, as well as peak width, some filtering was required. As it only detects local maxima, the algorithm was reapplied to the reverse data to detect the troughs. This produced two lists of data indices: peak and trough X,Y locations, which, when combined, allow for the representation of each growth ridge as a simplified triangle (Figure 4.29).
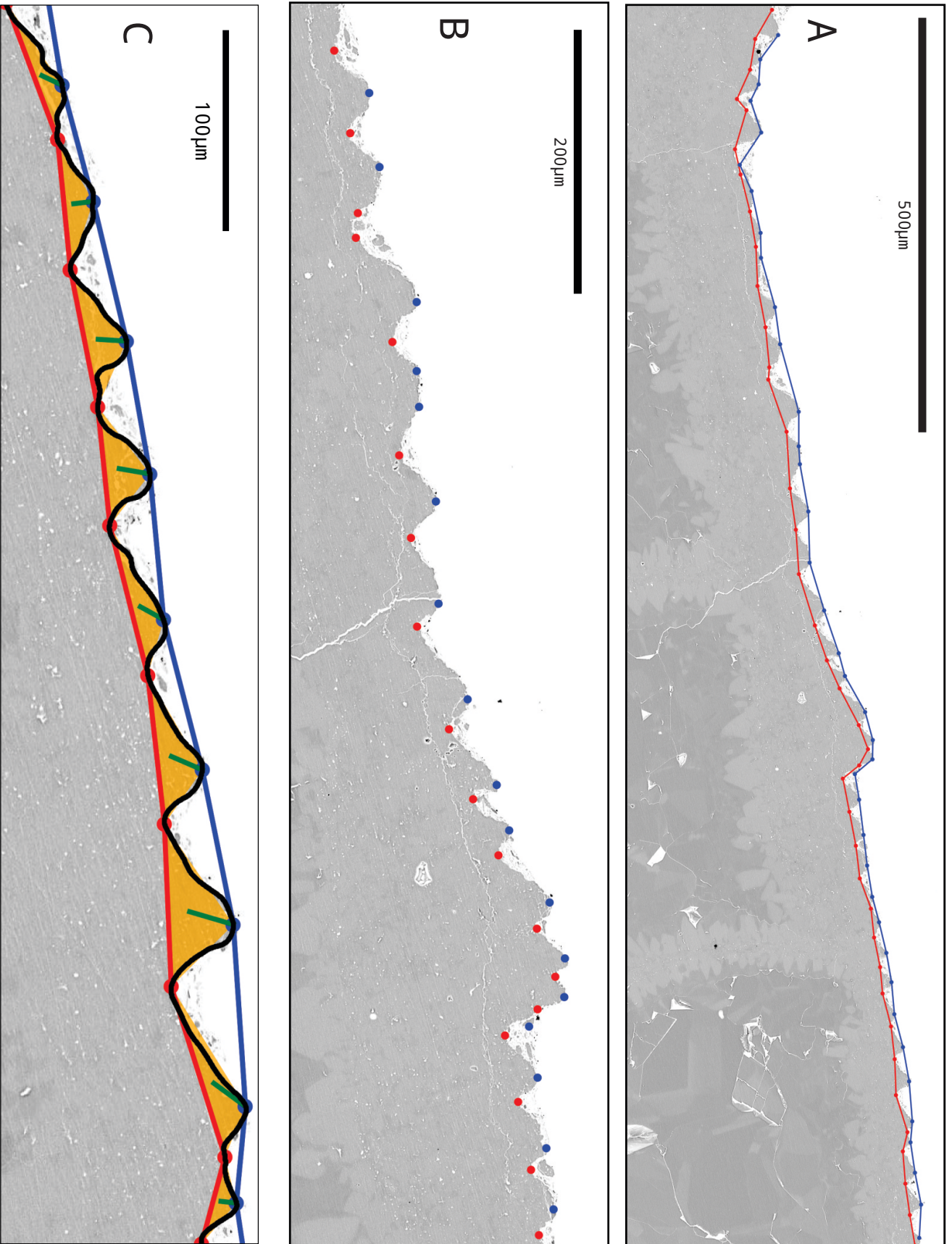
Figure 4.29: Continuous wavelet transform-based peak detection applied to an *Eridophyllum* sample region. (A) peaks (blue) and troughs (red) are selected and an envelope is drawn, connecting them; (B) some filtering is required, where the detected points do not alternate between peaks and troughs across the image; (C) simplified triangles (orange) representing growth ridges as trough-peak-trough sets.

4.5   Ridge geometry

As an ideal, simplified ridge can be represented as successive peak-trough-peak points the data sets were combined by interleaving the data and marking triangles every trough-peak-trough set. 'If' statements were used to check for regions where peaks and troughs did not alternate, and corrected this issue by advancing the list index (Figure 4.30). This produced a list of coordinates representing the vertices of each ridge, grouped in sets of 3, allowing for standard trigonometric methods to be applied (Figure 4.29C).
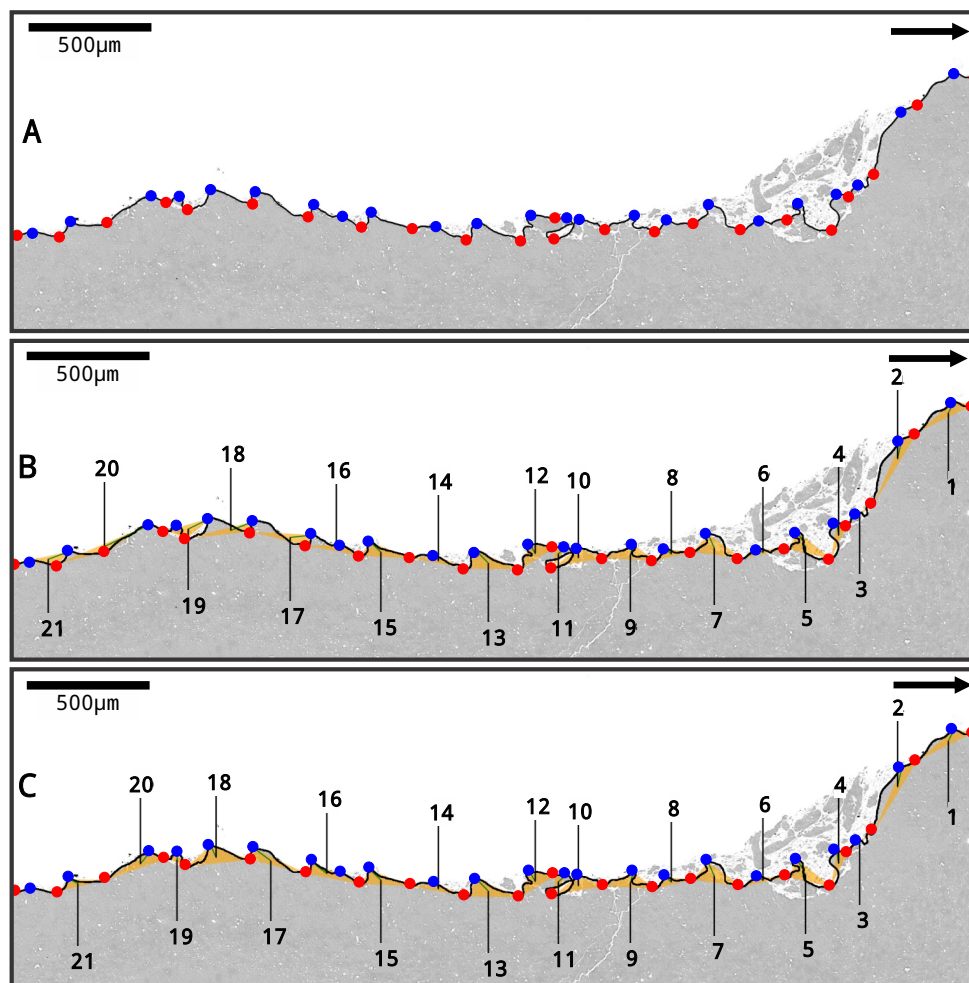
Figure 4.30: Extrema filtering during grouping (A) extracted edge line included fracture debris in centre of image; (B) alternating peak-trough-peak sets become disordered after line curves back on itself; (C) 'if' statement checks included to advance the extrema indices to record subsequent ridge sets properly.

With three known points, trigonometric equations can be used to find the approximate

properties of the ridges. As an image is simply a 2D matrix, these directly correspond to the

sample (Glassner, 1990). The following geometric measurements were made for each trough-

peak-trough set: side lengths (Equation 4.1), angles between sides (Equation 4.2), centroid

(Figure 4.3), and triangle area (Equation 4.4).

$$sidelength\ AB = \sqrt{\frac{(A_x + B_x + C_x)^2}{(A_y + B_y + C_y)^2}} \tag{4.1}$$

$$angle\ AB = cos^{-1}\frac{b^2 + c^2 - a^2}{2\,b\,c} \tag{4.2}$$

$$centroid\ ABC = \frac{A_x + B_x + C_x}{3}, \frac{A_y + B_y + C_y}{3} \tag{4.3}$$

$$area\ ABC = \frac{|A_x(B_y - C_y) + B_x(C_y - A_y) + C_x(A_y - B_y)|}{2} \tag{4.4}$$

These geometric properties were calculated for each growth ridge detected and exported to a text (.csv) file for each sample image. (Figure 4.31)
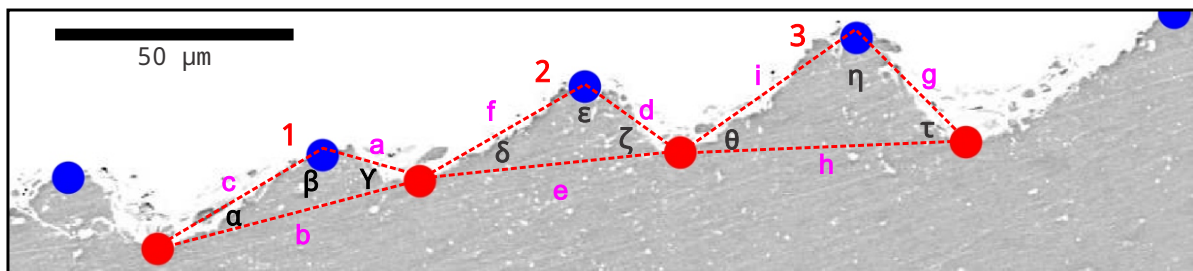
ID	Area (μm²)	Centroid (X,Y)	Vertices (X,Y)	Lengths (μm)	Angles (°)
1	247.57	(989,186)	A: (1080,176) B: (1006,155) C: (881,226)	a: 19.28 b: 51.44 c: 36.04	α: 15.49 β: 134.56 γ: 29.95
2	359.28	(1187,144)	D: (1277,154) E: (1205,104) F: (1080,176)	d: 21.98 e: 49.69 f: 36.16	δ: 23.57 ε: 115.28 ζ: 41.15
3	577.17	(1393,120)	G: (1492,145) H: (1410,63) I: (1277,154)	g: 29.07 h: 53.95 i: 40.40	θ: 31.98 η: 100.62 τ: 47.39

Figure 4.31: Sample geometric data from ridges extracted from *Eridophyllum*.

Chapter 5

Results

The methods described in the previous chapter were applied to three composite images: both epithecal edges of *Eridophyllum* (A and B) and one of *Cystiphylloides* (C). They were subsampled into relatively continuous subsections, divided by natural fractures in the edge line. For each subsection, a line representing the epithecal edge (referred to hereafter as the 'epithecal edge line' was extracted and exported as a set of X-Y coordinates, then saved to a plaintext ('sample_line.csv') file.

Each dataset was then imported for continuous wavelet transformation peak detection and data analysis. Local extrema were interpreted as peaks and troughs within growth ridges of the epithecal edge, identified as indices of the original dataset. These were grouped into alternating trough-peak-trough sets to produce simplified triangles representing detected growth ridges. In cases of two adjacent peaks or troughs, the algorithm advanced to the next extrema. The X-Y coordinates of each trough-peak-trough set were used to calculate geometric data for each triangle, such as area, side lengths, and angles between sides. These geometric values may be related to coral growth and potentially growth cycles in an attempt to quantify coral growth rate (Figure 5.1, Table 5.1).
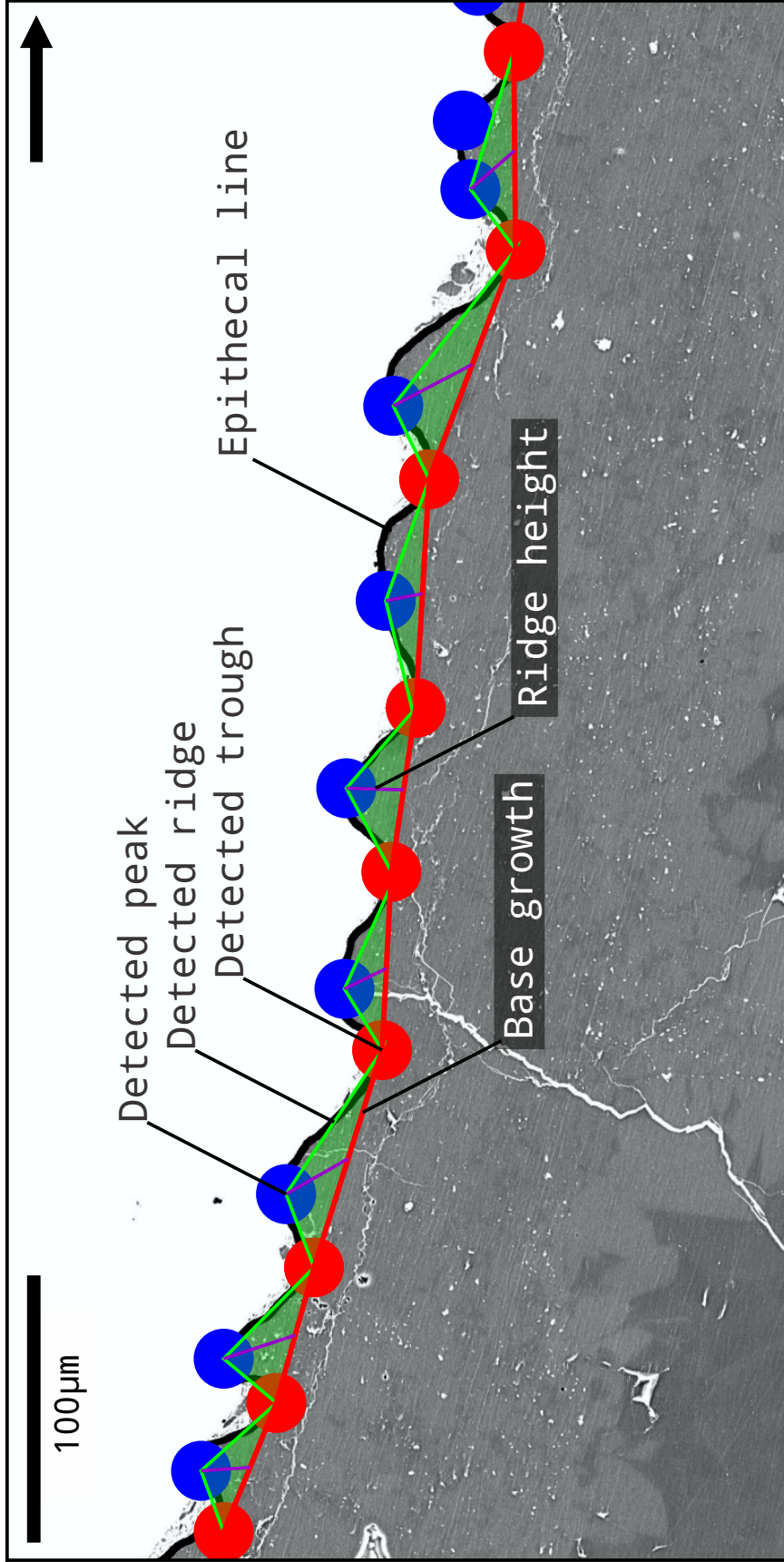
Figure 5.1: Quantities measured from extracted epithecal edge line (arrow indicates growth direction).

Extrema	local maxima and minima, found using peak detection methods applied to the epithecal edge line
Detected peak	local maxima detected within epithecal edge line, representing local maximum polyp expansion and skeletal diameter.
Detected trough	local minima detected within epithecal edge line, representing local maximum polyp constriction and skeletal diameter. Line represents coral resting state.
Detected ridge	set of three consecutive detected trough-peak-trough points, representing an interval of growth where the polyp transitioned from maximum constriction, to maximum expansion, then returned to maximum constriction.
Ridge area	area (μm^2) of a trough-peak-trough triangle representation of a growth ridge. A quantifiable measure of coral growth for a particular growth interval.
Ridge length	distance (μm) from trough-trough, for a given ridge, beginning at and returning to maximum polyp constriction for a growth interval
Ridge height	distance (μm) from peak to trough-trough centre point, for a given ridge, representing growth along the longitudinal axis for a given growth interval.
Ridge ratio	Proportionality of ridge height to ridge length (ridge height / ridge length)
Base growth length	length (μm) of line connecting all trough points, for a given image section. Records maximum coral polyp constriction for for growth intervals and may represent a continuous record of daily vertical growth
Epithecal length	actual length (μm) of the epithecal edge line extracted from an image section
Growth ratio	Total deviation from maximum constriction (trough-trough line), potentially representing growth from a polyp's daily resting state (base growth length / epithecal length)
Section length	Total coral specimen SEM image length (mm).

Table 5.1: Description of quantitative terms used.

These measurements were exported to a second text file for each sample ('sample_tri_data.csv'), with properties for each detected ridge in the subsampled area, scaled to microns using the original image metadata. Summary data for all specimens (Tables 5.2, 5.3), as well as subsampled regions of *Cystiphylloides* (Figure 5.2, Tables 5.4, 5.5) and *Eridophyllum* side A (Figure 5.3, Tables 5.6, 5.7) and side B (Figure 5.4, Tables 5.8, 5.9) are displayed below. All individual datasets are reportable in .csv files for each subsampled region.

Specimen name	Section length	Sections sampled	Base length	Epithecal length	Growth ratio
Cystiphylloides	16930 μm	9	17706 μm	20866 μm	0.8486
Eridophyllum A	20330 μm	6	20736 μm	28174 μm	0.7360
Eridophyllum B	20060 μm	6	18528 μm	24211 μm	0.7653

Table 5.2: Lengths summary table for 3 specimens: *Cystiphylloides*, *Eridophyllum* side A, and *Eridophyllum* side B.

Specimen name	Ridges detected	Ridge area (Mean ± SD)	Ridge length (Mean ± SD)	Ridge height (Mean ± SD)	Ridge ratio (Mean ± SD)
Cystiphylloides	244	331.17 μm^2 ± 383.92	68.31 μm ± 26.03	18.56 μm ± 15.94	0.2708 ± 0.2200
Eridophyllum A	481	169.90 μm^2 ± 161.08	41.50 μm ± 18.74	12.88 μm ± 9.01	0.3254 ± 0.2258
Eridophyllum B	390	215.25 μm^2 ± 226.30	45.20 μm ± 19.47	14.71 μm ± 11.29	0.3342 ± 0.2489

Table 5.3: Ridge properties summary table for 3 specimens: *Cystiphylloides*, *Eridophyllum* side A, and *Eridophyllum* side B.

Figure 5.2: *Cystiphylloides* study sections.
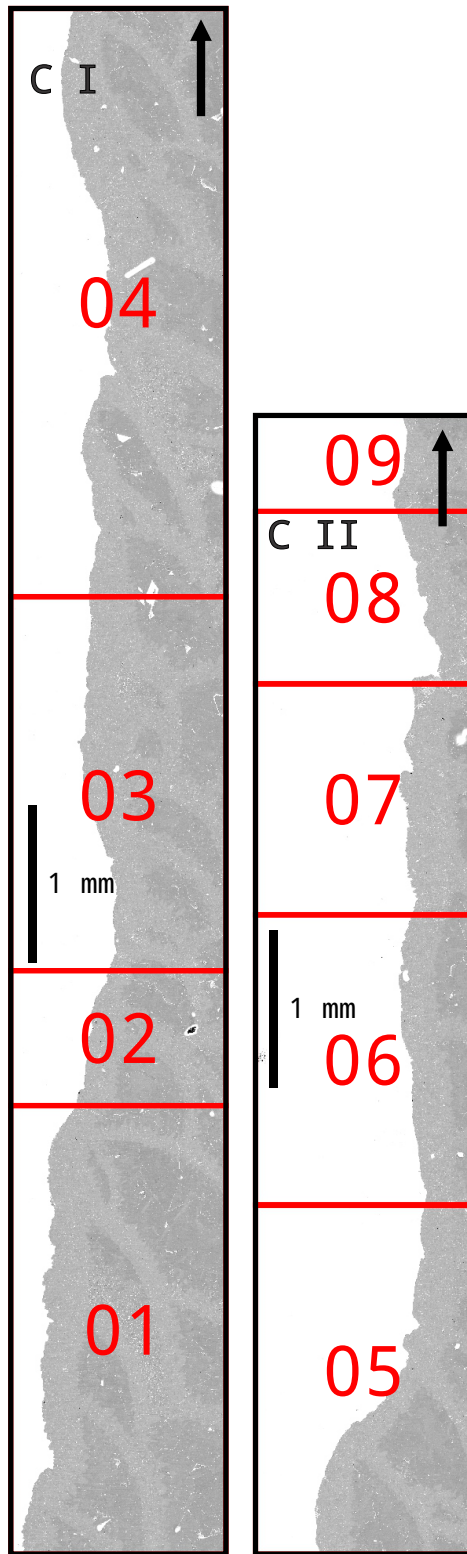
Section	Base Length	Epithecal Length	Growth Ratio
C_01	2998 μm	3624 μm	0.8274
C_02	878 μm	1003 μm	0.8761
C_03	2415 μm	2781 μm	0.8685
C_04	3781 μm	4451 μm	0.8495
C_05	2321 μm	2891 μm	0.8028
C_06	1778 μm	2129 μm	0.8352
C_07	1522 μm	1952 μm	0.7796
C_08	1119 μm	1349 μm	0.8299
C_09	450 μm	686 μm	0.6559

Table 5.4: *Cystiphylloides* length analysis.

Section name	Ridges detected	Ridge area (Mean ± SD)	Ridge length (Mean ± SD)	Ridge height (Mean ± SD)	Ridge ratio (Mean ± SD)
C_01	41	393.38 μm^2 ± 301.76	68.71 μm ± 25.30	23.87 μm ± 19.65	0.3505 ± 0.2807
C_02	12	460.04 μm^2 ± 564.38	73.20 μm ± 34.90	12.27 μm ± 10.06	0.1500 ± 0.0575
C_03	35	256.14 μm^2 ± 223.63	66.74 μm ± 26.48	16.62 μm ± 9.88	0.2473 ± 0.1338
C_04	48	387.17 μm^2 ± 513.09	74.21 μm ± 30.42	24.52 μm ± 23.12	0.3404 ± 0.3345
C_05	31	305.88 μm^2 ± 396.28	72.81 μm ± 21.64	18.09 μm ± 12.86	0.2354 ± 0.1191
C_06	29	213.01 μm^2 ± 140.29	59.50 μm ± 18.84	13.38 μm ± 7.03	0.2281 ± 0.1318
C_07	26	345.32 μm^2 ± 462.18	58.54 μm ± 23.31	15.01 μm ± 9.45	0.2630 ± 0.1329
C_08	16	385.63 μm^2 ± 310.87	69.95 μm ± 18.83	14.22 μm ± 8.61	0.1970 ± 0.0792
C_09	6	133.32 μm^2 ± 103.88	75.02 μm ± 23.14	12.96 μm ± 10.84	0.1697 ± 0.1048

Table 5.5: *Cystiphylloides* ridge geometry.

Figure 5.3: *Eridophyllum* A side study sections.
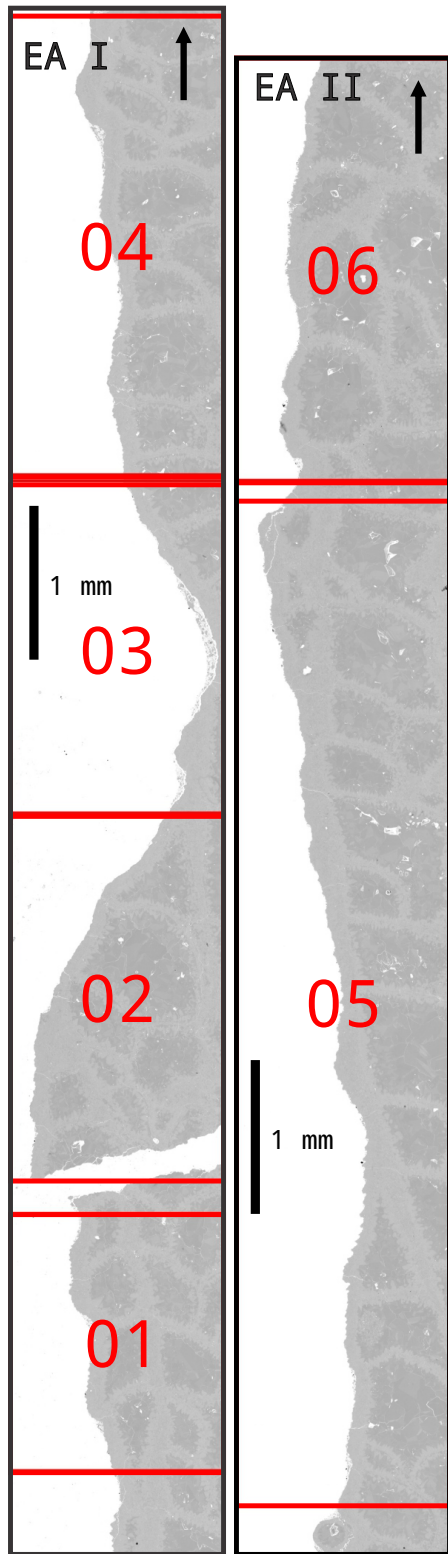
Section	Base Length	Epithecal Length	Growth Ratio
EA_01	1867 μm	2535 μm	0.7362
EA_02	2766 μm	3388 μm	0.8166
EA_03	2512 μm	3132 μm	0.8021
EA_04	3139 μm	4144 μm	0.7573
EA_05	7428 μm	10390 μm	0.7149
EA_06	3025 μm	4585 μm	0.6598

Table 5.6: *Eridophyllum* side A length analysis.

Section name	Ridges detected	Ridge area (Mean ± SD)	Ridge length (Mean ± SD)	Ridge height (Mean ± SD)	Ridge ratio (Mean ± SD)
EA_01	41	393.38 μm^2 ± 301.76	68.71 μm ± 25.30	23.87 μm ± 19.65	0.3505 ± 0.2807
EA_02	12	460.04 μm^2 ± 564.38	73.20 μm ± 34.90	12.27 μm ± 10.06	0.1500 ± 0.0575
EA_03	35	256.14 μm^2 ± 223.63	66.74 μm ± 26.48	16.62 μm ± 9.88	0.2473 ± 0.1338
EA_04	48	387.17 μm^2 ± 513.09	74.21 μm ± 30.42	24.52 μm ± 23.12	0.3404 ± 0.3345
EA_05	31	305.88 μm^2 ± 396.28	72.81 μm ± 21.64	18.09 μm ± 12.86	0.2354 ± 0.1191
EA_06	29	213.01 μm^2 ± 140.29	59.50 μm ± 18.84	13.38 μm ± 7.03	0.2281 ± 0.1318

Table 5.7: *Eridophyllum* side A ridge geometry.

Figure 5.4: *Eridophyllum* B side study sections.
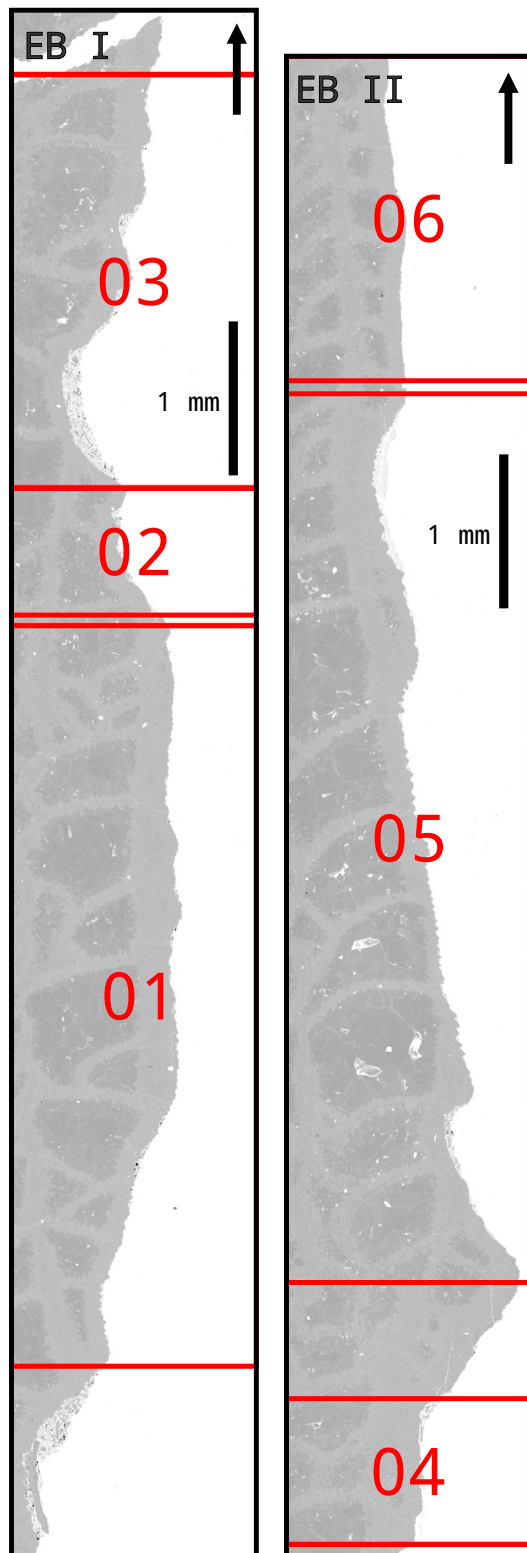
Section	Base Length	Epithecal Length	Growth Ratio
EB_01	5107 μm	6423 μm	0.7952
EB_02	910 μm	1170 μm	0.7773
EB_03	3254 μm	4384 μm	0.7422
EB_04	910 μm	1179 μm	0.7714
EB_05	6265 μm	8441 μm	0.7422
EB_06	2083 μm	2614 μm	0.7967

Table 5.8: *Eridophyllum* side B length analysis.

Section name	Ridges detected	Ridge area (Mean ± SD)	Ridge length (Mean ± SD)	Ridge height (Mean ± SD)	Ridge ratio (Mean ± SD)
EB_01	108	189.55 μm^2 ± 168.09	44.27 μm ± 18.20	14.77 μm ± 12.34	0.3390 ± 0.2776
EB_02	22	105.05 μm^2 ± 86.87	41.36 μm ± 13.90	9.98 μm ± 7.45	0.2411 ± 0.1512
EB_03	71	195.14 μm^2 ± 223.63	42.50 μm ± 21.66	15.45 μm ± 8.26	0.4216 ± 0.2933
EB_04	22	120.73 μm^2 ± 513.09	41.34 μm ± 14.65	10.35 μm ± 6.71	0.2400 ± 0.1095
EB_05	118	335.52 μm^2 ± 311.56	51.38 μm ± 21.10	17.76 μm ± 12.78	0.3387 ± 0.1913
EB_06	49	103.33 μm^2 ± 77.04	39.78 μm ±	10.26 μm 14.35 ± 8.90	0.2702 ± 0.2676

Table 5.9: *Eridophyllum* side B ridge geometry.

The values extracted from the coral epithecal edge line are highly variant, commonly with standard deviations larger than the mean values. These results, as well as their reliability, will be discussed in the next chapter.

Chapter 6

Discussion

6.1   Critique of method

The original aim of this thesis was to quantify coral growth features and recognize growth cycles in order to interpret changes in paleoenvironmental conditions at the time of growth. With no background in digital image processing and analysis, the majority of time was spent researching image processing theory and, through a process of trial-and error, determining the steps (and parameters) to extract the most representative data from epithecal slices. Consequently, traditional, reportable results are limited.

The key scientific contribution of this thesis is the development of a method to extract coral growth data, beginning with a whole coral specimen. Scanning electron microscopy was used to image the epithecal edge of a specimen, sectioned along its longitudinal growth axis. Image processing techniques were then applied to the output to extract a set of X-Y coordinates representing the epithecal edge line. Peak detection was applied to detect local extrema, which represent peaks and troughs within the epithecal surface. Extrema were then grouped into trough-peak-trough sets to represent growth ridges as simplified triangles. This allowed for the calculation of geometric properties, which may be used as measures of growth.

6.1.1 Section selection

Though this method accurately extracts data from a coral epithecal edge line, it is difficult to determine its quality, as there is no way to confirm that the fossil specimen originally recorded continuous growth at regular intervals. When dealing with a record of unknowable accuracy, it is important to ensure any methods applied to that record limit the introduction of more uncertainty. The most important step in this process is the selection of the coral epithecal slice that best represents coral growth.

Extracting two-dimensional measurements from a slice of a three-dimensional object presents a set of challenges. The resultant geometry of the two-dimensional slice is dependent on the location chosen (Figure 6.1). Though attempts were made to slice along the approximate growth axis, the calice of the coral exhibits some degree of rotation and tilt in the long axis of growth in three dimensions. It is difficult to determine if the calice is leaning toward, or away from the observer in a two-dimensional slice as this information is permanently lost when the thin section is produced. Any deviations from an absolutely straight direction of longitudinal growth will result in any ridges appearing somewhat distorted in two-dimensions.

Rugose corals appear to have been able to right themselves in order to maintain a horizontal calice, which enhances their survival potential, particularly after toppling events due to physical disturbance by storms or predation attempts (Berkowski, 2011). The polyp achieved this by varying the rate of skeletal growth on each side of the growth axis until stability was achieved; extreme changes in growth direction are commonly observed in elbow-like geniculations in solitary rugose corals (Scrutton, 1997). Coral polyps may have continuously ad-

justed their growth direction during regular conditions, simply as a result of sediment shifting or changes in current. This can increase the difficulty of isolating a single slice representative of the full length of a coral specimen. These localized changes in growth rate can also influence the detection of ridges and their resultant measurements. Decreased growth within the inside of a curve may result in ridges too fine to detect, while the increased growth on the outside surface of the curve will feature exaggerated ridges (Figure 6.2).
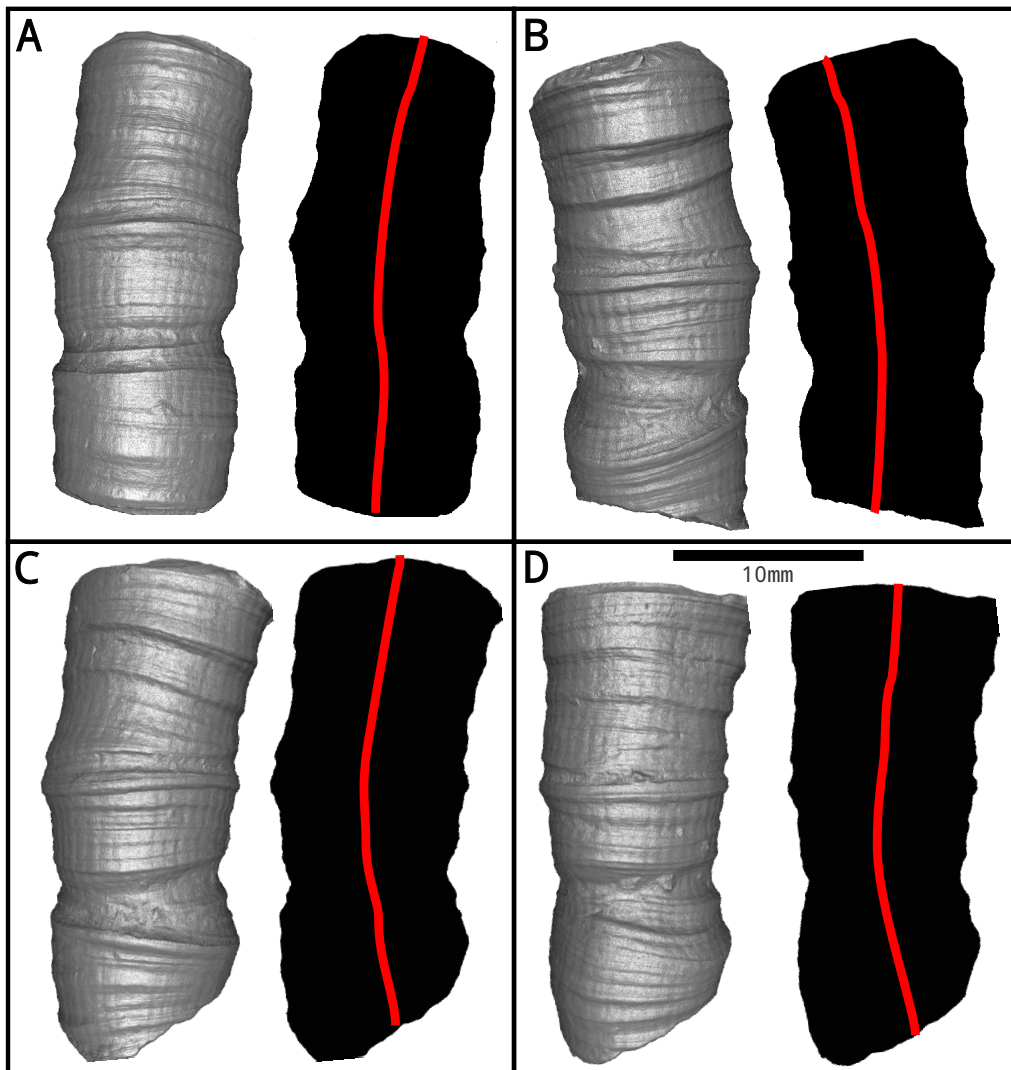
Figure 6.1: Orientation and location of longitudinal slice may have a large effect on ridge geometry extracted from a two-dimensional slice. Shown, 3D Micro-CT rendering of *Eridophyllum*, rotated on the longitudinal axis (L) and the resultant 2D outline (R). (A) 8°rotation; (B) 97°rotation; (C) 194°rotation; (D) 324°rotation.
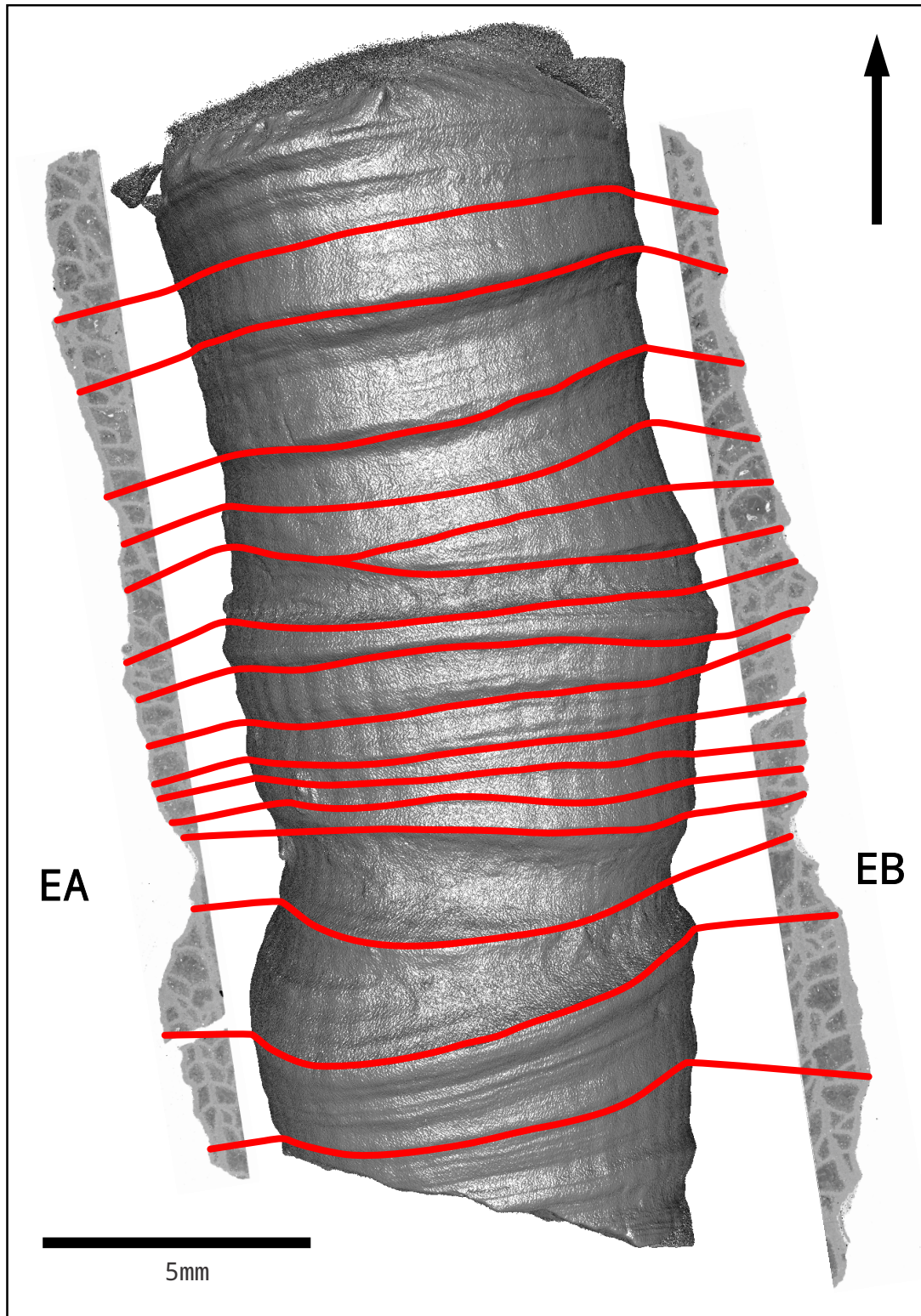
Figure 6.2: Select growth ridges marked in red on 3D rendering of *Eridophyllum*, linked to ridges within SEM images, highlighting the difficulties related to comparing both edges of a two-dimensional slice. The distance between two lines represents the same growth interval on each side, but due to changes in growth direction, actual measurements may be quite different.

6.1.2 SEM imaging

Potential issues can also arise during SEM imaging in cases when the upper and lower

(depth) surface widths of the specimen are not equal. SEM signal output is altered by edge

geometry and may scan the edge of both the upper and a portion of the lower surface. When

section thickness varies along the sample, the output image will not accurately represent the

specimen. As it is not possible to obtain an ideal, infinitely thin specimen, some degree of dis-

tortion will be added, which is difficult to quantify and its correction requires computationally

intensive deconvolution (Figure 6.3) (Nyyssonen, 1988).
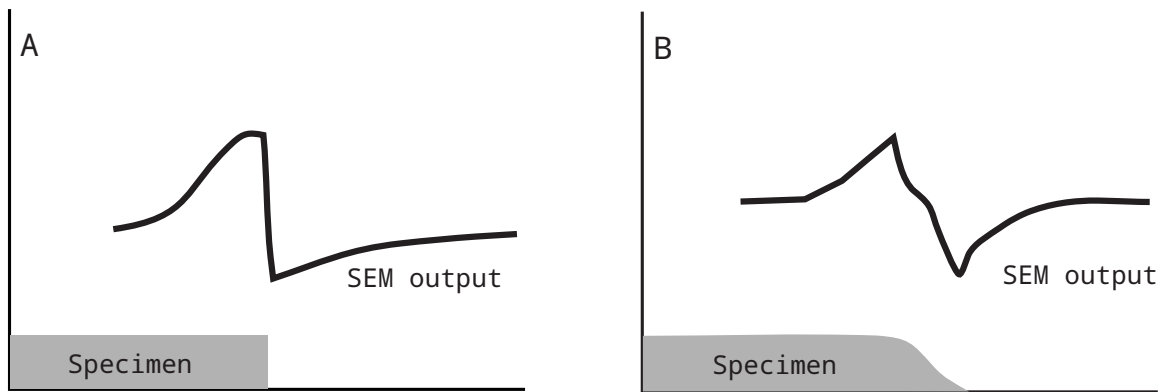
Figure 6.3: Effect of edge geometry on SEM output. (A) uniform sample width produces a hard edge,
easily captured by SEM imaging; (B) non-uniform sample thickness introduces distortion
in SEM output, as the angled surface between the top and bottom is also recorded, making
it computationally difficult to produce an actual representation of the edge, modified after
Nyyssonen (1988).

As the specimen size decreases, the thickness of the section slice is a larger proportion of the section width, amplifying this effect. As seen in *Eridophyllum*, a portion of the outer skeletal surface was scanned, along with the epithecal edge upper surface edge. This is even more apparent within constricted areas, where there is a greater difference between top and bottom surface widths. The apparent constriction of skeletal diameter is exaggerated in these sections, complicating line extraction. Filtering often blends edge artefacts into the coral edge, distorting the output (Figure 6.4).
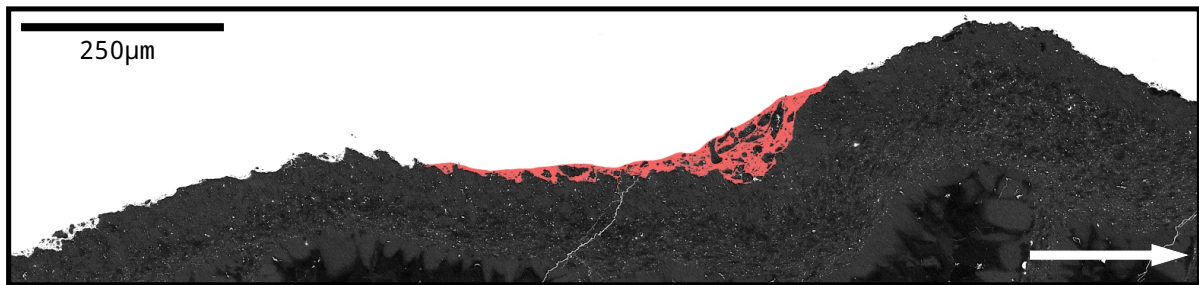
Figure 6.4: Possible exaggeration of skeletal constriction (red) within *Eridophyllum* as a result of SEM edge output distortion.

Though the number of growth ridges is consistent, their dimensions will be proportionate to the edge line of the lower specimen surface. Some of the edge artefacts seen outside the coral body in *Eridophyllum* appear to be a portion of the corallite face or matrix that was dislodged and floated to the epoxy surface during preparation, as growth ridges are occasionally faintly seen in their outline. The method developed in this thesis detects these smaller ridges, though any measurements obtained from them cannot be directly related to other sections (Figure 6.5).
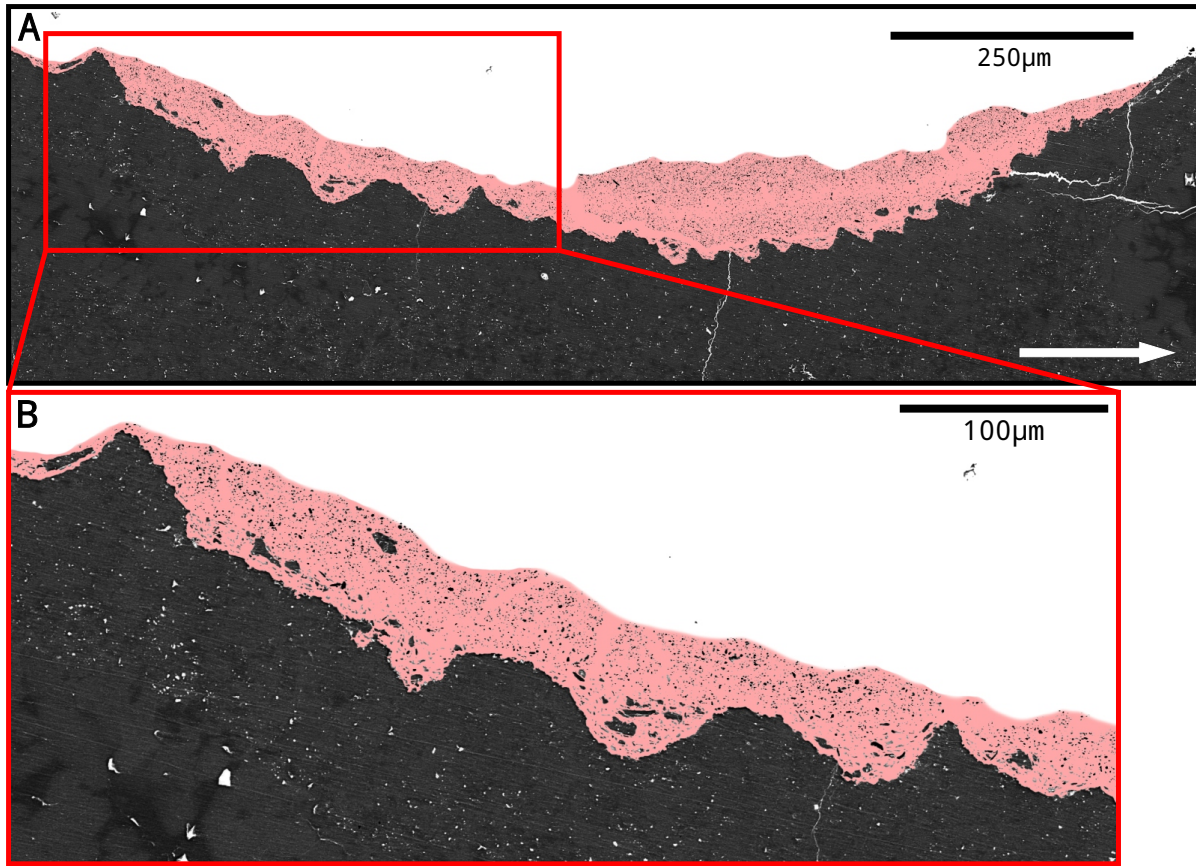
Figure 6.5: *Eridophyllum* SEM edge output distortion, shaded in red. Faint growth ridge outlines can be seen in the 'debris' along the edge, suggesting that some component of the curved coral face is being imaged, along with the top surface. These artefacts may be a direct image, or loose matrix material that has risen to the surface during epoxy setting.

6.1.3   Image processing

Edge detection extracts a set of pixel coordinates representing boundaries of features within a digital image. The general procedure begins with contrast normalization, denoising, and thresholding, which produces a binary image of the desired feature to be traced (Chapter 4: Methods). Each of these steps requires a degree of operator input, such as which regions of the image are searched, or which pixel intensity values best represent the target feature. In effect, these are arbitrarily chosen numbers based on visual observation of the images to pro-

vide the best digital representation of the data, according to the operator (Sun et al., 2009). Though an attempt has been made to automate the process for this thesis by choosing locally adaptive algorithms where possible and limiting image pre-processing, ultimately, some operator bias is unavoidable. All algorithms were chosen to ultimately extract what was believed to be the highest quality representation of the coral edge line, according to the author.

Yamaguchi and Komuro (2003) explored the quantification Line Edge Roughness (LER) in SEM image analysis. Typically used with linear features, LER quantifies departures in the extracted data from an ideal line in an image. The operator must find the best thresholding value to optimize a smooth line, while still accurately representing feature geometry. The smoothest line does not always represent the best quality data, as too much or too little of the image may be removed in the process, essentially 'cutting outside of the lines'. Poor image resolution or file compression can compound this issue, if compressed regions are larger than image details. Though LER is not quantifiable in non-linear curves, particularly in organic specimens subjected to diagenesis, where the 'ideal curve' is unknown, it describes the challenge of extracting the most representative numeric data from SEM images (Figure 6.6).
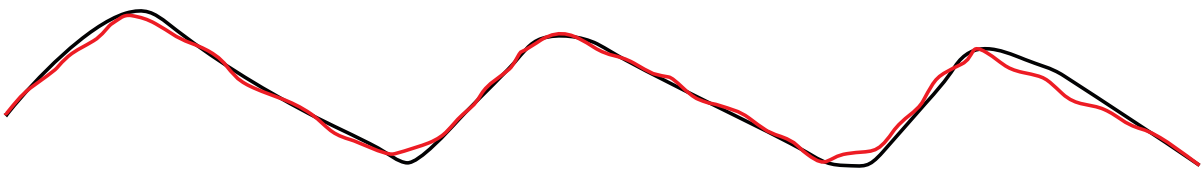
Figure 6.6: Line Edge Roughness attempts to quantify the accuracy of data extracted from a digital image by measuring deviations from a straight line. While only attempted with linear features, the concept can be broadly applied to curves, as shown. The black line represents the ideal edge feature as interpreted by the operator, whereas the red line represents the extracted data. A balance must be struck between best representing the overall shape, while limiting deviations from the outline (Yamaguchi and Komuro, 2003).

6.1.4   Uncertainty within fossil records

When examining skeletal growth records in fossil organisms, there is always a degree of uncertainty associated the completeness of the record. Ultimately, if a growth interval is missing, it cannot be measured. Pannella et al. (1968) discussed the difficulties of using fossils as paleoenvironmental records, stating that precision is partially controlled by 'random' environmental events. The lack of living individuals to study complicates the determination of growth patterns. Growth increments may not have been recorded for a particular time period due to some external factor, or they may have been lost through diagenetic alteration or destruction. There is no way to account for these gaps in the record. They suggest using multiple organisms from different taxa, such as bivalves, to develop a complete record and cross-check results (Figure 6.7) (Pannella et al., 1968).
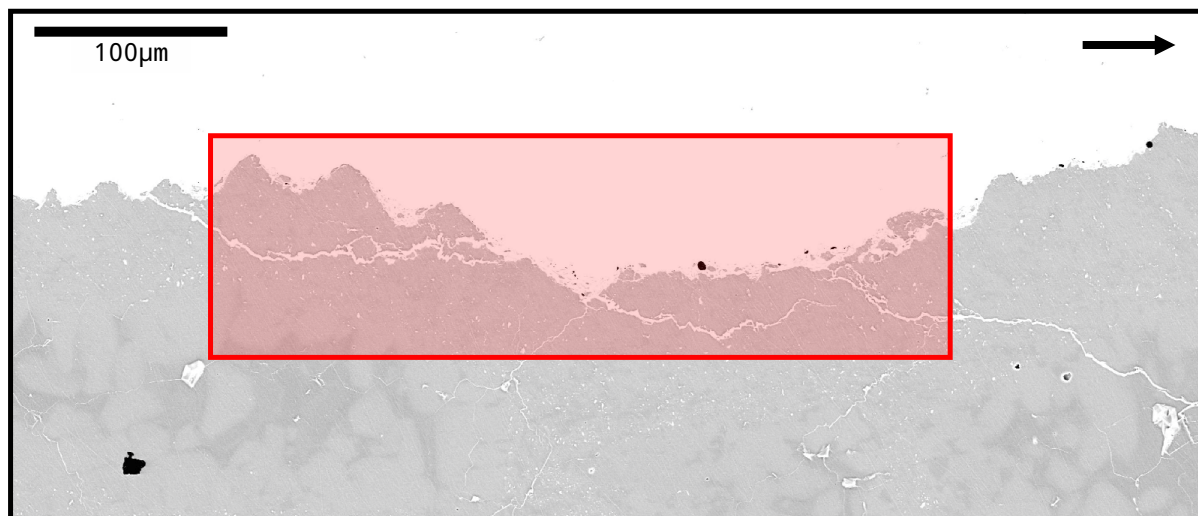
Figure 6.7: The accuracy of paleontological records always have a degree of uncertainty. Highlighted area shows permanently missing growth information, which may have either not been recorded, or lost through diagenesis or fracturing, with no way to 'fill in the blanks'.

6.2   Pattern recognition

As the main goal of this thesis was to determine the influence of paleoenvironmental cy-

cles on coral growth, multiple attempts were made to automatically detect suspected lunar

(monthly) and annual bundles of growth ridges, as per Scrutton (1964), using larger scale

continuous wavelet transformation peak detection. This was attempted with the original ep-

ithecal edge line, as well as the list of detected trough points (Figure 6.8). As they are less

likely to be broken or abraded, troughs may be more reliable than peaks as markers of growth

ridges. These troughs represent the coral polyp's maximum constriction for each growth

ridge. Limitations of coral preservation also decreased the success rate; if a growth interval

is missing from a fossil record, it cannot be counted.
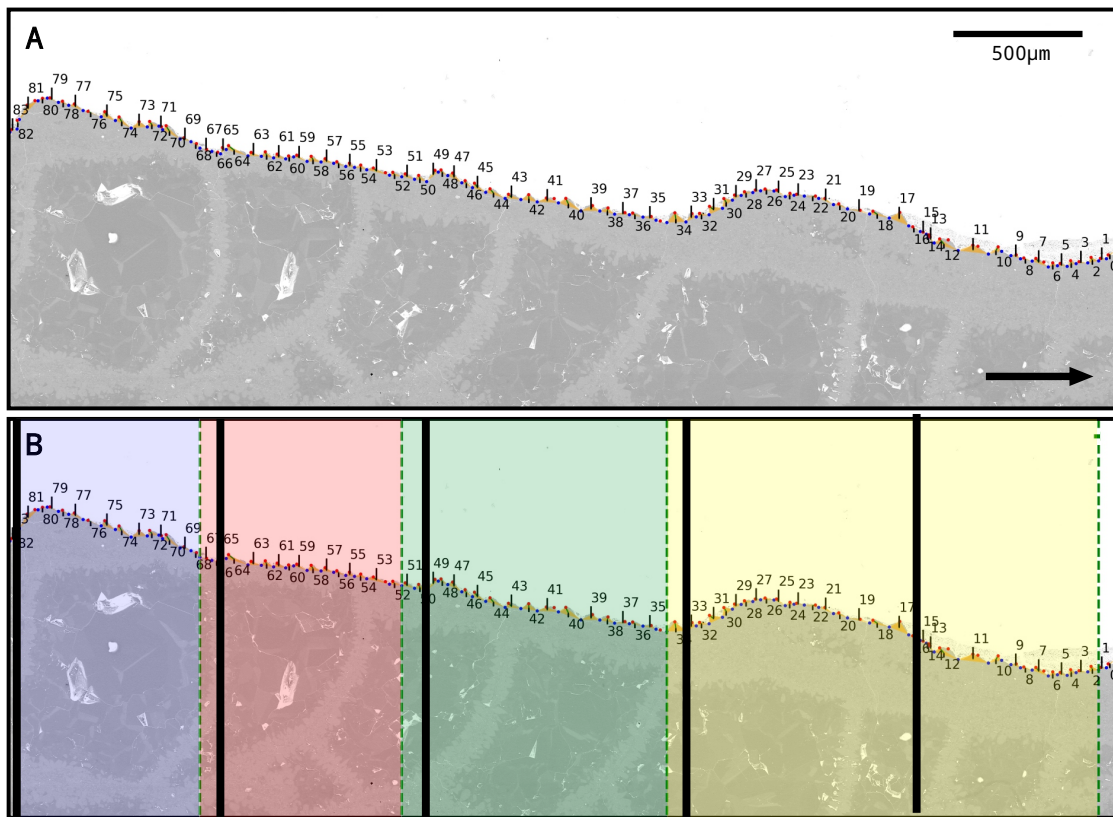
Figure 6.8: (A) Detection of larger scale bundles of ridges was ultimately unsuccessful; (B) detected groupings highlighted in colour, patterns recognized by eye divided by black lines.

6.2.1 Observations

Due to the reasons listed previously, it is difficult to compare the measurements extracted from the coral specimens with absolute confidence, as demonstrated by the large variance in values, often having standard deviations equal to or greater than the mean values.

Fine growth ridges, tens of microns across, are visible within the coral specimens, as in previous work (Scrutton, 1964; Wells, 1963). Due to poor specimen quality, continuous records were limited, as a result, larger scale 'monthly' ridges were difficult to assess. Larger 'monthly' bundles can be seen in microCT, also in accordance with Scrutton (1964), though poor preservation of the fine-scale ridges limits their ability to be consistently counted. The most well-defined region, *Eridophyllum* side B, section 05, shows what appear to be daily ridges grouped into bundles of ∼ 15-17 (Figure 6.9). These bundles are rare within the specimens and not seen in *Cystiphylloides*, perhaps due to the susceptibility of its larger ridges' to physical damage, or imaging resolution limitations. There is rarely a continuous, unaltered record and some extrapolation between ridges must be used, due to either a lack of deposition, or data lost to diagenesis.
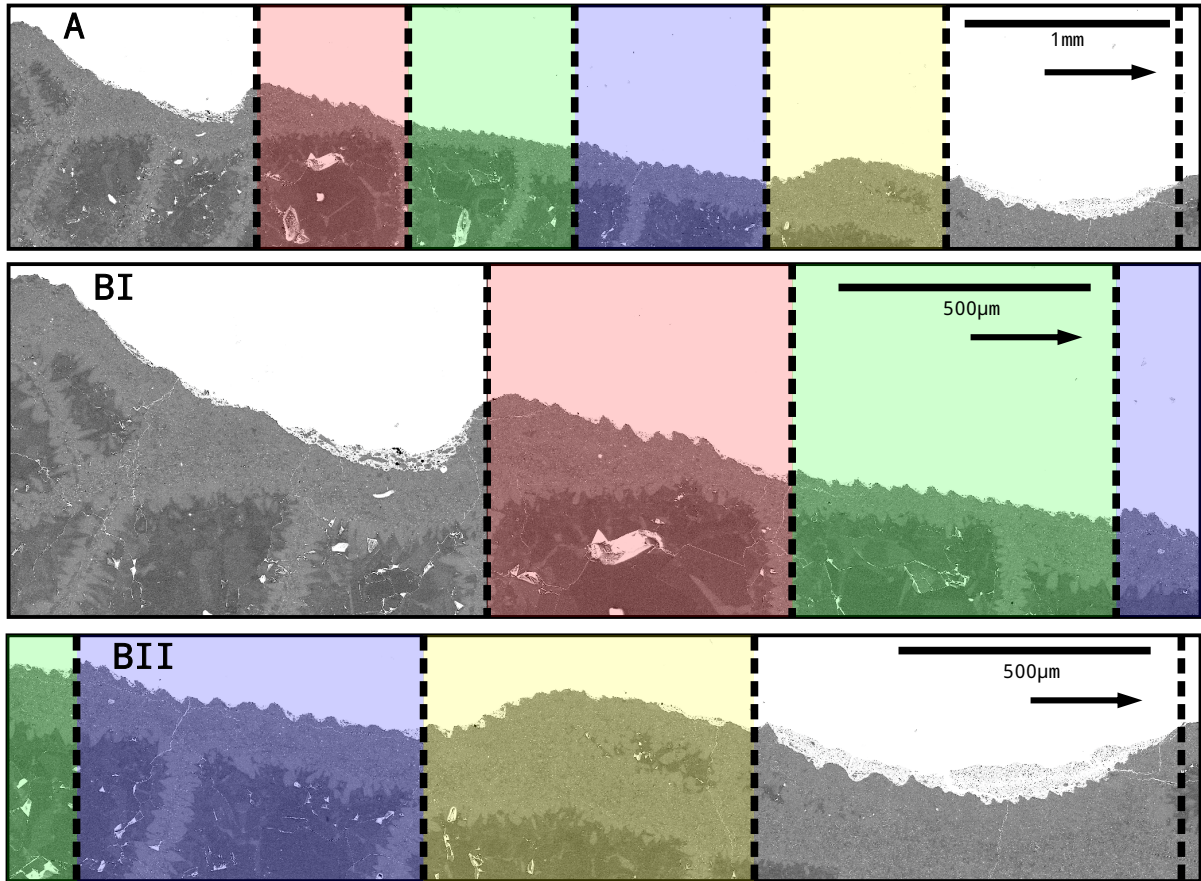
Figure 6.9: Four consecutive sub-monthly growth increments of ~15-17 ridges, each shaded a different colour, within *Eridophyllum* B. (A) full sub-section length; (B) 2X magnification.

The results show high variability, with standard deviations commonly larger than the mean values. This appears to be driven in part by the difference in scale of legitimate, detected ridges (Figure 6.10), though some outliers are due to defects in the coral specimen, falsely detected as ridges. Post-processing, particularly filtering out 'unacceptable' ridges, may be required to remove poor quality matches, but while developing this method, output filtering was limited to demonstrate its objectivity.
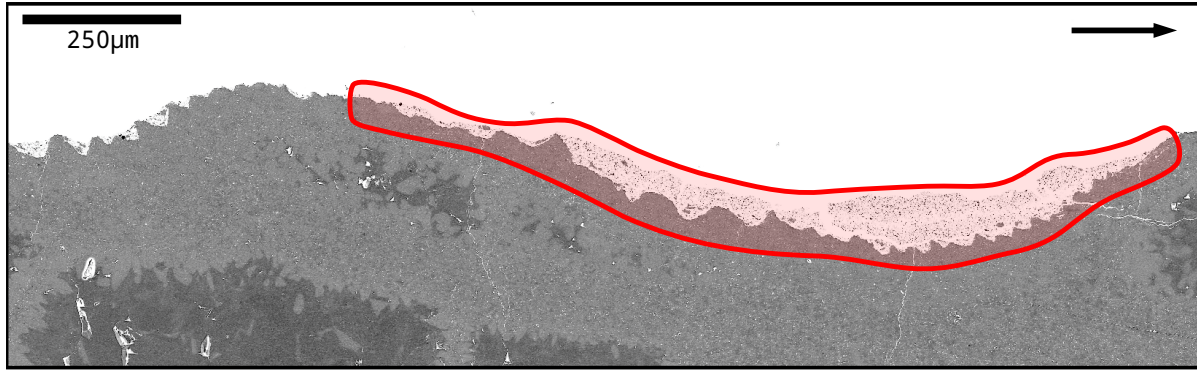
Figure 6.10: The differing scale of growth ridges detected with this method creates large variance within the resultant data. As seen in the shaded region of an *Eridophyllum* section above, the scale of ridges appears to be related to the overall curvature of the skeleton, though future analysis would be required to confirm this.

If the extracted data is representative of true coral growth, the results appear to show a rhythmic increase/decrease cycle for both ridge area and ridge ratio (Figures 6.11 - 6.16). The area of detected ridges may be related to coral growth as triangular cross-sections through previous calicular positions. Ridge ratio, the proportion of ridge base length to ridge height, may give an approximation of vertical skeletal extension as compared to skeletal diameter, with values closer to zero representing more equilateral ridges. This could indicate a small-scale, monthly perhaps, cycle of increasing and decreasing growth. This could also be a product of larger-scale changes in growth direction, which would have resulted in the 'daily' ridges being deposited on a curve, distorting their shape. Additional samples would need to be examined in order to determine the reliability of any patterns and attempt to isolate them.
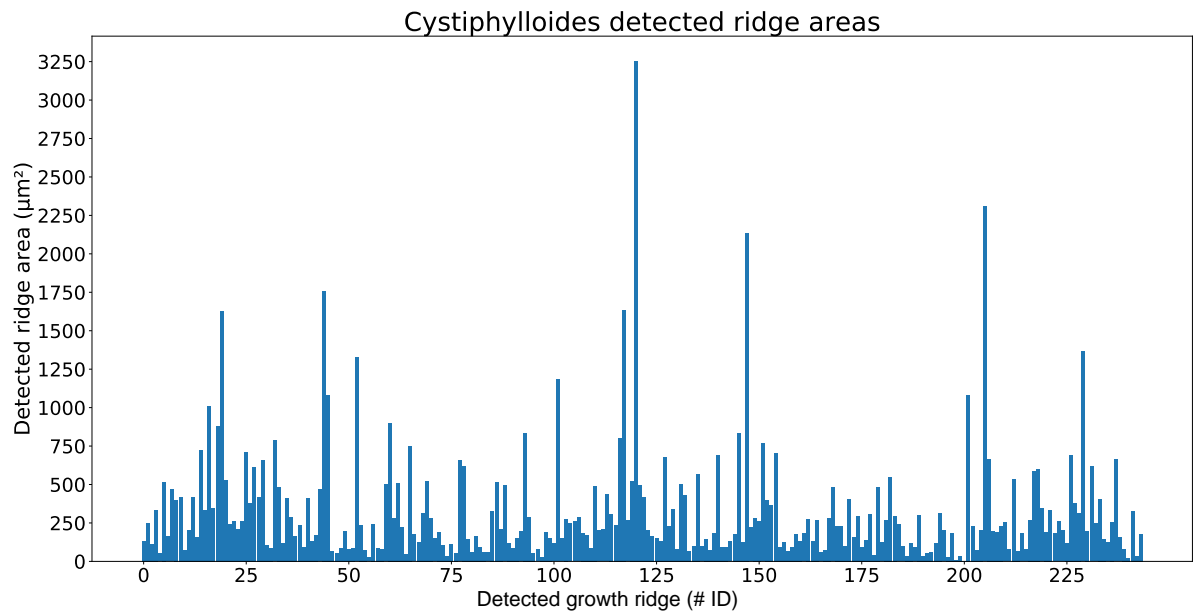
Figure 6.11: Detected ridge area plot for *Cystiphylloides*.
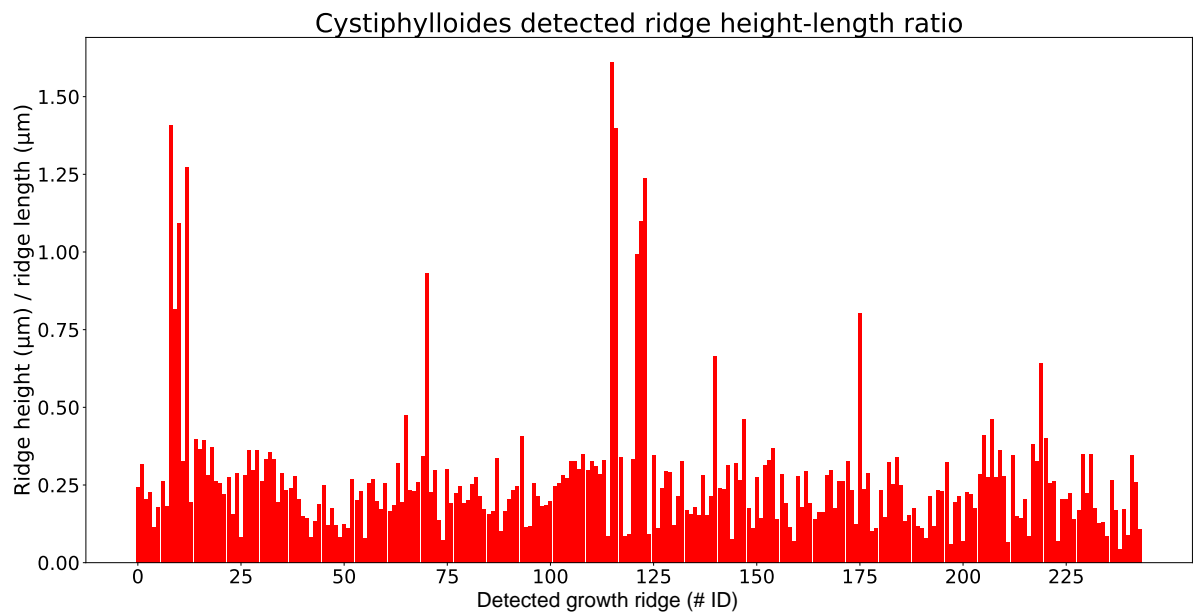
Figure 6.12: Detected ridge ratio (ridge height/length) plot for *Cystiphylloides*.
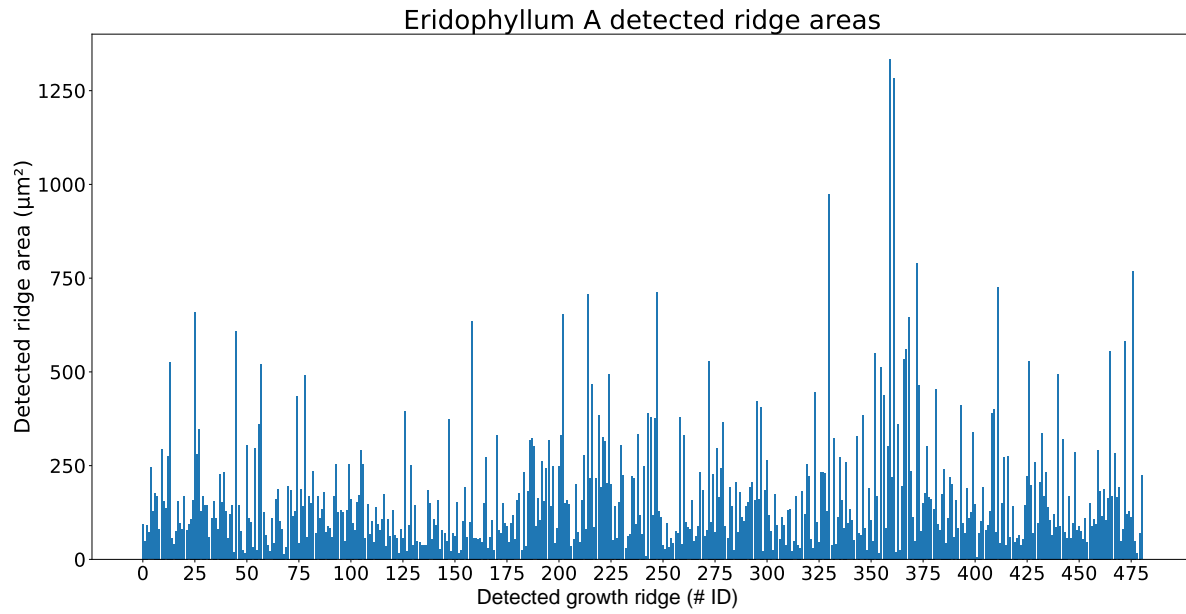
Figure 6.13: Detected ridge area plot for *Eridophyllum* A.
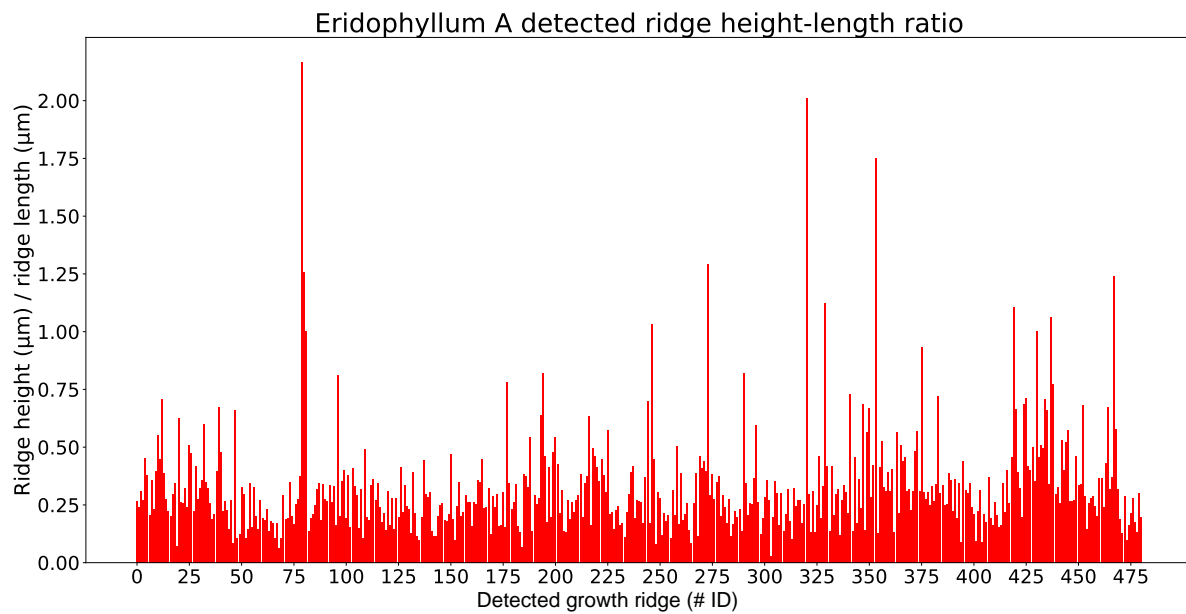
Figure 6.14: Detected ridge ratio (ridge height/length) plot for *Eridophyllum* A.
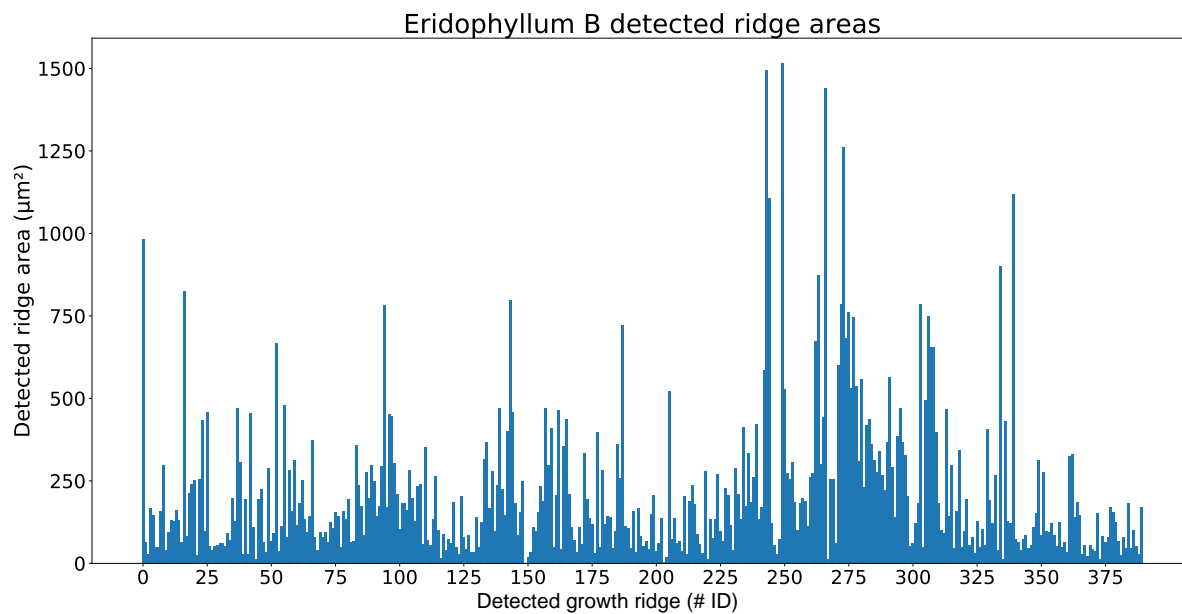
Figure 6.15: Detected ridge area plot for *Eridophyllum* B.
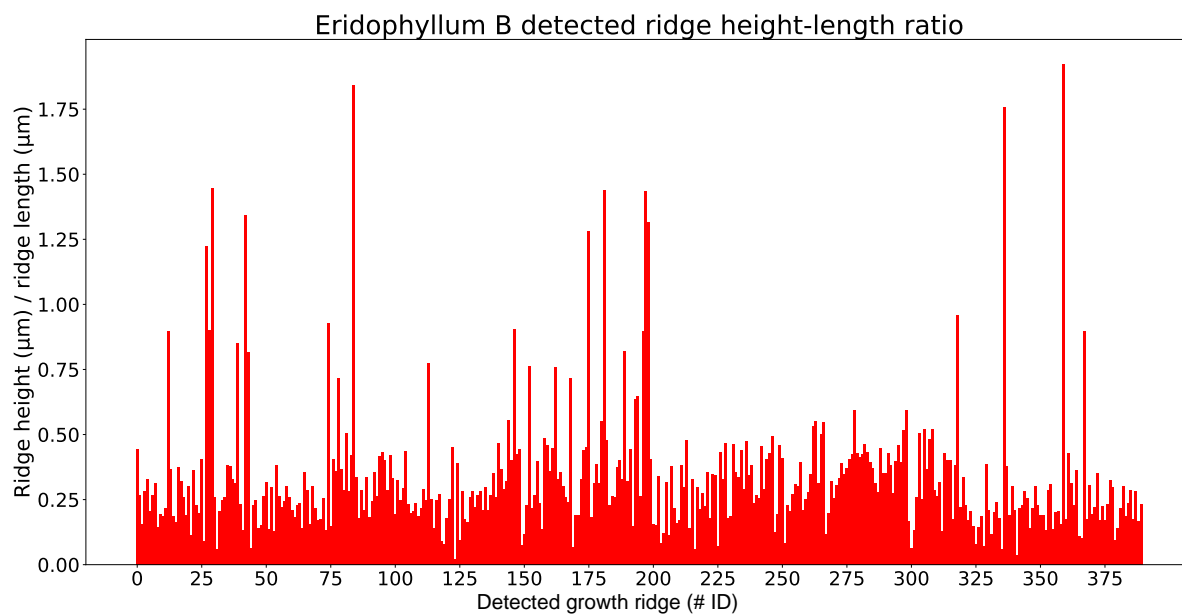
Figure 6.16: Detected ridge ratio (ridge height/length) plot for *Eridophyllum* B.

6.3   Interpretation

Sub-monthly bundles of ~15-17 daily ridges suggests that a semi-monthly environmental control influenced coral growth, suggesting a lunar or tidal component, as moonlight and tidal amplitudes reach a maximum or minimum half-way through each lunar month, the time required for Moon to make one full orbit around Earth (Kronfeld-Schor et al., 2013). This could provide an explanation for both 'monthly' and 'daily' growth increments.

6.3.1   Influence of moonlight on corals

The metabolic processes in many organisms are partially tied to a circadian rhythm, corresponding to the daily light-dark cycle. Specialized DNA photoreceptor proteins, known as cryptochromes, respond to specific wavelengths of light to optimally use the light available within their environment (Figure 6.17) (Gorbunov and Falkowski, 2002; Levy et al., 2007). Various studies have shown that corals are sensitive to blue light (~480 nm), which is most available under the clear, oligotrophic waters that they occupy. Studies have noted that that expression of the photoreceptive genes *cry1* and *cry2*, follow the daily light-dark cycle (Levy et al., 2007). In particular, *cry2* expression is increased during night (Levy et al., 2007).
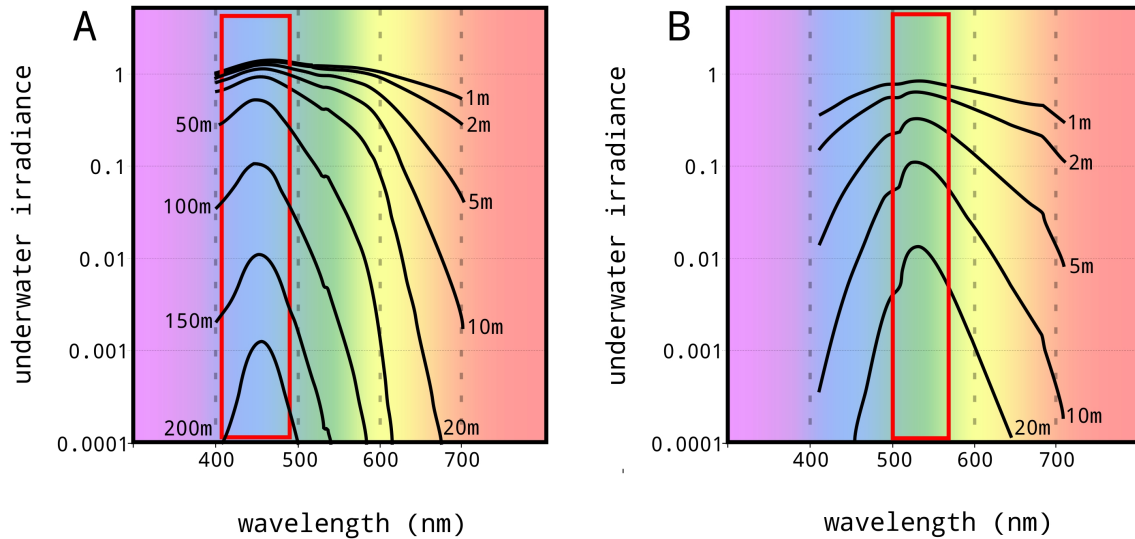
Figure 6.17: Irradiance under seawater at various depths in (A) clear, oligotrophic waters and (B) plankton-rich, eutrophic waters. Marine organisms in these settings have adapted to optimally respond to the most available wavelength of light, modified after Wozniak and Dera (2007).

As many corals have photosynthetic symbionts, early workers were uncertain if these proteins were located within the coral polyp, or side-effects of photosymbiotic activity. Gorbunov and Falkowski (2002) noted that corals commonly expand at night and have a lunar breeding periodicity. They studied the effect of moonlight on modern photosynthetic corals and found that moonlight directly influences coral polyp morphology. They shone targeted blue and red light sources on coral polyps and used laser scattering to measure slight contraction and expansion, to determine whether the photoreceptors responsible for corals' response to moonlight were contained within the coral polyp or the photosymbionts. When blue light was applied to a polyp, they detected a slight contraction. By targeting different parts of the coral, they were able to determine that the photoreceptors were located within the tentacles of the corals, as no other part of the coral body elicited a response. They also determined that the photosynthetic symbionts within are more sensitive to longer (red) wavelengths of light and

thus, are not active at night (Gorbunov and Falkowski, 2002). This suggests that coral lunar periodicity is genetically encoded, regardless of the presence of photosymbionts.

Modern corals expand at dusk for feeding, though the driver for this diurnal cycle has not been confirmed (Barnes, 1972). If the major control on skeletal diameter are lunar cycles, fine-scale daily ridges may be created as the polyp opens and closes based on moon light, in a small-scale version of constriction and expansion (Berkowski, 2011; Dubinsky and Falkowski, 2011). Kronfeld-Schor et al. (2013) studied the interference of solar and lunar cycles and found that due to the slightly different periodicities, it is difficult to isolate either sun or moonlight as controls of 'daily' cycles, as they may be masked by each other (Kronfeld-Schor et al., 2013). The variability (~15-17) of the number of 'daily' ridges within 'monthly' sub-bundles may be a result of sunlight and moonlight cycles interacting, altering the number of growth increments per month.

Chapter 7

Conclusions and future work

The goal of this thesis was to quantify longitudinal growth in fossilized rugose corals from Devonian strata at Hungry Hollow in an attempt to interpret changes in paleoenvironmental conditions during growth. A method was developed to objectively detect and measure epithecal growth ridges from two dimensional longitudinal slices of specimens: First, image processing and filtering were used to trace the epithecal edge line of SEM scanned images and export it to a set of X-Y coordinates. Then, continuous wavelet transformation peak detection was used to mark local maxima and minima, representing peaks and troughs within the epithecal surface. These were then grouped into sets of triangles, representing model growth ridges. Simple geometric properties were measured (area, lengths) to be interpreted as coral growth.

Due to the large time investment required to develop this method, as there was limited previous research upon which to build, reportable results are limited to two example specimens, one each of Eridophyllum and Cystiphylloides. A further effort to develop an autonomous method for large-scale ridge bundle detection was unsuccessful. The results nevertheless show a potential sub-monthly (~15-17 day) bundling pattern, not previously observed in the literature, in one length of continuous growth, although well-preserved sections were

limited. This sub-monthly bundling could provide evidence of a lunar or tidal influence on coral growth, beyond its role in periodic breeding.

Future work should apply this method to multiple specimens to better understand variations in scale of daily growth ridges in fossil rugose coral, in order to determine the required amount of post-processing applied to the output. In all future research, the emphasis should be on sample preparation. A more precise slicing method, perhaps using computer-aided laser cutting, guided by three-dimensional imaging should give the ability to follow the corals' growth axis more closely. Sectioning the specimens before cleaning may reduce the risk of removal of ridge definition while scrubbing.

Coral specimens may also need to be cut into smaller lengths with a similar growth direction to minimize the impact of large-scale growth changes on the individual ridge measurements. Finally, the extracted epithecal line could prove useful as a way to isolate longer-term environmental changes from daily, cyclic growth cycles, particularly when compared to growth records from other organisms, such as bivalves and brachiopods, within the same paleoenvironment.

References

Palaeozoic corals: their evolution and palaeoecology. 15.

Abram, N. J., Webster, J. M., Davies, P. J., and Dullo, W. C., 2001. Biological response of coral reefs to sea surface temperature variation: evidence from the raised Holocene reefs of Kikai-jima (Ryukyu Islands, Japan). Coral Reefs, 20.3, 221–234.

Ahern, J. L. and Dikeou, P. J., 1989. Evolution of the lithosphere beneath the Michigan Basin. Earth and Planetary Science Letters, 95.1, 73–84.

Airi, V., Gizzi, F., Falini, G., Levy, O., Dubinsky, Z., and Goffredo, S., 2014. Reproductive Efficiency of a Mediterranean Endemic Zooxanthellate Coral Decreases with Increasing Temperature along a Wide Latitudinal Gradient. PLoS ONE, 9.3, .

Allemand, D., Ferrier-Pags, C., Furla, P., Houlbrque, F., Puverel, S., Reynaud, S., Tambutt, r., Tambutt, S., and Zoccola, D., 2004. Biomineralisation in reef-building corals: from molecular mechanisms to environmental control. Comptes Rendus Palevol, 3.6-7, 453–467.

Armstrong, D. K. and Carter, T. R. The subsurface Paleozoic stratigraphy of Southern Ontario, volume no. 7 of Special volume. Ontario Geological Survey, Sudbury, 2010.

Baars, C., Ghobadi Pour, M., and Atwood, R. C., 2013. The earliest rugose coral. Geological Magazine, 150.02, 371–380.

Baird, G. C. and Brett, C. E., 1983. Regional Variation and Paleontology of Two Coral Beds in the Middle Devonian Hamilton Group of Western New York. Journal of Paleontology, 57.3, 417–446.

Baker, P. A. and Weber, J. N., 1975. Coral growth rate: variation with depth. Physics of the Earth and Planetary Interiors, 10.2, 135–139.

Barnes, D. J., 1970. Coral Skeletons: An Explanation of Their Growth and Structure. Science, 170.3964, 1305–1308.

Barnes, D. J., 1972. The Structure and Formation of Growth-Ridges in Scleractinian Coral Skeletons. Proceedings of the Royal Society of London. Series B, Biological Sciences, 182 .1068, 331–350.

Barnes, D. J. and Crossland, C. J., 1980. Diurnal and Seasonal Variations in the Growth of a Staghorn Coral Measured by Time-Lapse Photography. Limnology and Oceanography, 25 .6, 1113–1117.

Bartholomew, A. J. and Brett, C. E., 2007. Correlation of Middle Devonian Hamilton Group-equivalent strata in east-central North America: implications for eustasy, tectonics and faunal provinciality. Geological Society, London, Special Publications, 278.1, 105–131.

Bartholomew, A. J., Brett, C. E., DeSantis, M., Baird, G. C., and Tsujita, C., 2006. Sequence stratigraphy of the Middle Devonian at the border of the Michigan Basin; correlations with New York and implications for sea-level change and paleogeography. Northeastern Geology and Environmental Sciences, 28.1, 2–33.

Berkowski, B., 2011. Life Strategies and Function of Dissepiments in Rugose Coral *Catactotoechus instabilis* from the Lower Devonian of Morocco. Acta Palaeontologica Polonica, 57.2, 391–400.

Berkowski, B. and Belka, Z., 2008. Seasonal growth bands in Famennian rugose coral *Scruttonia kunthi* and their environmental significance. Palaeogeography, Palaeoclimatology, Palaeoecology, 265.1-2, 87–92.

Blattner, T., Keyrouz, W., Chalfoun, J., Stivalet, B., Brady, M., and Zhou, S. A Hybrid CPU-GPU System for Stitching Large Scale Optical Microscopy Images. In 2014 43rd International Conference on Parallel Processing, pages 1–9, 2014.

Bradski, G., 2000. The OpenCV Library. Dr. Dobb's Journal of Software Tools.

Brett, C. E., Baird, G. C., Bartholomew, A. J., DeSantis, M. K., and Ver Straeten, C. A., 2011. Sequence stratigraphy and a revised sea-level curve for the Middle Devonian of eastern North America. Palaeogeography, Palaeoclimatology, Palaeoecology, 304.12, 21–53.

Brosche, P. and Sündermann, J., editors. Tidal Friction and the Earths Rotation. Springer Berlin Heidelberg, Berlin, Heidelberg, 1978.

Burger, W. and Burge, M. J., 2009. Principles of Digital Image Processing: Fundamental Techniques. Springer eBooks.

Burgess, P. M., 2008. Chapter 2 Phanerozoic Evolution of the Sedimentary Cover of the North American Craton. Sedimentary Basins of the World, 531–63.

Chalfoun, J., 2014. A power stitching tool. SPIE Newsroom.

Clark, G. R., 1974. Growth lines in invertebrate skeletons. Annual Review of Earth and Planetary Sciences, 2.1, 77–99.

Clarkson, E. N. K. Invertebrate palaeontology and evolution. Blackwell Science, Oxford ; Malden, MA, 4th ed edition, 1998.

Cocks, L. R. M. and Torsvik, T. H., 2011. The Palaeozoic geography of Laurentia and western Laurussia: A stable craton with mobile margins. Earth-Science Reviews, 106.1-2, 1–51.

Cohen, A. L. and McConnaughey, T. A., 2003. Geochemical perspectives on coral mineralization. Reviews in mineralogy and geochemistry, 54.1, 151–187.

Comboul, M., Emile-Geay, J., Evans, M. N., Mirnateghi, N., Cobb, K. M., and Thompson, D. M., 2014. A probabilistic model of chronological errors in layer-counted climate proxies: applications to annually banded coral archives. Climate of the Past, 10.2, 825–841.

Donato, S. Paleoecology of the Middle Devonian Leiorhynchus Shale and coral biostrome of the Hungry Hollow Formation in Southwestern Ontario. MSc. thesis, Dept. of Earth Sciences, University of Western Ontario, London, ON, 2003.

Du, P., Kibbe, W. A., and Lin, S. M., 2006. Improved peak detection in mass spectrum by incorporating continuous wavelet transform-based pattern matching. Bioinformatics, 22.17, 2059–2065.

Du, P., Kibbe, W. A., and Lin, S. M. Using the MassSpecWavelet package, 2007.

Dubinsky, Z. and Falkowski, P. Light as a Source of Information and Energy in Zooxanthellate Corals. In Dubinsky, Z. and Stambler, N., editors, Coral Reefs: An Ecosystem in Transition, pages 107–118. Springer Netherlands, 2011.

Edinger, E. N., Copper, S. P., Risk, M. J., and Atmojo, W., 2002. Oceanography and reefs of recent and Paleozoic tropical epeiric seas. Facies, 47.1, 127–149.

Fagerstrom, J. A., 1994. The history of Devonian-Carboniferous reef communities: Extinctions, effects, recovery. Facies, 30.1, 177–191.

Fedorowski, J., 1978. Some aspects of coloniality in rugose corals. Palaeontology, 21.1, 177–224.

Fisher, J. H., Barratt, M. W., Droste, J. B., and Shaver, R. H., 1988. Michigan basin. The Geology of North America, 2361–382.

Flude, L. I. Geniculation and growth banding in rugose corals of the Middle Devonian Hungry Hollow Formation of Southwestern Ontario. BSc. thesis, Dept. of Earth Sciences, University of Western Ontario, London, ON, 2005.

Glassner, A. S. Graphics gems. Academic Press, Boston, 1990.

Google Earth,. Arkona, Ontario region, 2017.

Gorbunov, M. Y. and Falkowski, P. G., 2002. Photoreceptors in the cnidarian hosts allow symbiotic corals to sense blue moonlight. Limnology and Oceanography, 47.1, 309–315.

Haralick, R. M. and Shapiro, L. G., 1984. Image segmentation techniques. Computer Vision, Graphics, and Image Processing, 27.3, 389.

Howell, P. D. and Pluijm, B. A.van der, 1990. Early history of the Michigan basin: Subsidence and Appalachian tectonics. Geology, 18.12, 1195–1198.

Howell, P. D. and Pluijm, B. A.van der, 1999. Structural sequences and styles of subsidence in the Michigan basin. Geological Society of America Bulletin, 111.7, 974–991.

Hunter, J. D., 2007. Matplotlib: A 2d Graphics Environment. Computing in Science Engineering, 9.3, 90–95.

Isern, A. R., McKenzie, J. A., and Feary, D. A., 1996. The role of sea-surface temperature as a control on carbonate platform development in the western Coral Sea. Palaeogeography, Palaeoclimatology, Palaeoecology, 124.3-4, 247–272.

Jacques, T. G., Marshall, N., and Pilson, M. E. Q., 1983. Experimental ecology of the temperate scleractinian coral Astrangia danae. Marine Biology, 76.2, 135–148.

Jakubowicz, M., Berkowski, B., Lpez Correa, M., Jarochowska, E., Joachimski, M., and Belka, Z., 2015. Stable Isotope Signatures of Middle Palaeozoic Ahermatypic Rugose Corals Deciphering Secondary Alteration, Vital Fractionation Effects, and Palaeoecological Implications. PLOS ONE, 10.9, .

Johnson, J. G., Klapper, G., and Sandberg, C. A., 1985. Devonian eustatic fluctuations in Euramerica. Geological Society of America Bulletin, 96.5, 567–587.

Jones, E., Oliphant, T., Peterson, P., and others,. SciPy: Open source scientific tools for Python, 2001.

Kronfeld-Schor, N., Dominoni, D., Iglesia, H. d. l., Levy, O., Herzog, E. D., Dayan, T., and Helfrich-Forster, C., 2013. Chronobiology by moonlight. Proceedings of the Royal Society of London B: Biological Sciences, 280.1765, .

Kuhnert, H., Ptzold, J., Hatcher, B., Wyrwoll, K.-H., Eisenhauer, A., Collins, L. B., Zhu, Z. R., and Wefer, G., 1999. A 200-year coral stable oxygen isotope record from a high-latitude reef off Western Australia. Coral Reefs, 18.1, 1–12.

Kushmaro, A., Rosenberg, E., Fine, M., Haim, Y. B., and Loya, Y., 1998. Effect of temperature on bleaching of the coral Oculina patagonica by Vibrio AK-1. Marine Ecology Progress Series, 171131–137.

Lee, S. C., Kim, H. K., Chun, I. K., Cho, M. H., Lee, S. Y., and Cho, M. H., 2003. A flat-panel detector based micro-CT system: performance evaluation for small-animal imaging. Physics in Medicine and Biology, 48.24, 4173–4185.

Levy, O., Appelbaum, L., Leggat, W., Gothlif, Y., Hayward, D. C., Miller, D. J., and Hoegh-Guldberg, O., 2007. Light-Responsive Cryptochromes from a Simple Multicellular Animal, the Coral Acropora millepora. Science, 318.5849, 467–470.

Lough, J. M. and Barnes, D. J., 2000. Environmental controls on growth of the massive coral Porites. Journal of Experimental Marine Biology and Ecology, 245.2, 225–243.

Lowe, D. G., 2004. Distinctive image features from scale-invariant keypoints. International journal of computer vision, 60.2, 91–110.

Lutz, M. Learning Python: Powerful Object-Oriented Programming. O'Reilly Media, Beijing, 5 edition edition, 2013.

Ma, T. Y. H. On the seasonal change of growth in a reef coral, Favia speciosa (Dana), and the water-temperature of the Japanese seas during the latest geological times. In Proc. Imp. Acad. Tokyo, volume 10, pages 353–356, 1934.

Majurski, M., Blattner, T., Chalfoun, J., and Keyrouz, W. MIST Algorithm Documentation, 2016.

Moyer, R. P. and Grottoli, A. G., 2011. Coral skeletal carbon isotopes (13c and 14c) record the delivery of terrestrial carbon to the coastal waters of Puerto Rico. Coral Reefs, 30.3, 791.

Naqvi, S. A. S., 1994. Seasonal variation in an annually-banded coral Porites: a scanning electron microscopy investigation. Marine geology, 118.3-4, 187–194.

Neuman, B. E. E., 1988. Some aspects of life strategies of Early Palaeozoic rugose corals. Lethaia, 21.2, 97–114.

Nie, B., Chen, T., Liang, M., Wang, Y., Zhong, J., and Zhu, Y., 1997. Relationship between coral growth rate and sea surface temperature in the northern part of South China Sea during the past 100 a. Science in China Series D: Earth Sciences, 40.2, 173–182.

Nyyssonen, D. A New Approach To Image Modeling And Edge Detection In The SEM. In Integrated Circuit Metrology, Inspection and Process Control II, volume 921, pages 48–56, 1988.

Otsu, N., 1979. A threshold selection method from gray-level histograms. IEEE transactions on systems, man, and cybernetics, 9.1, 62–66.

Pandolfi, J. M. The Paleoecology of Coral Reefs. In Dubinsky, Z. and Stambler, N., editors, Coral Reefs: An Ecosystem in Transition. Springer Netherlands, 2011.

Pannella, G., MacClintock, C., and Thompson, M. N., 1968. Paleontological Evidence of Varitions in Length of Synodic Month since Late Cambrian. Science, 162.3855, 792–796.

Pizer, S. M., Amburn, E. P., Austin, J. D., Cromartie, R., Geselowitz, A., Greer, T., Haar Romeny, B.ter, Zimmerman, J. B., and Zuiderveld, K., 1987. Adaptive histogram equalization and its variations. Computer Vision, Graphics, and Image Processing, 39.3, 355–368.

Pol, J. C. Quantitative imaging methods of Devonian coral growth cycles. BSc. thesis, Dept. of Earth Sciences, University of Western Ontario, London, ON, 2014.

Postek, M. T., 1988. SEM Imaging and Applications. Integrated Circuit Metrology, Inspection, and Process Control, .2, 47.

Postek, M. T. The Scanning Electron Microscope. In Handbook of Charged Particle Optics, pages 363–394. CRC Press, USA, 1997.

Preibisch, S., Saalfeld, S., and Tomancak, P., 2009. Globally optimal stitching of tiled 3d microscopic image acquisitions. Bioinformatics, 25.11, 1463–1465.

Prior, D. J., Boyle, A. P., Brenker, F., Cheadle, M. C., Day, A., Lopez, G., Peruzzo, L., Potts, G. J., Reddy, S., Spiess, R., and others,, 1999. The application of electron backscatter diffraction and orientation contrast imaging in the SEM to textural problems in rocks. American Mineralogist, 84.11-12, 1741–1759.

Rosic, N., Kaniewska, P., Chan, C.-K. K., Ling, E. Y. S., Edwards, D., Dove, S., and Hoegh-Guldberg, O., 2014. Early transcriptional changes in the reef-building coral Acropora aspera in response to thermal and nutrient stress. BMC genomics, 15.1, 1052.

Rozhnov, S. V., 2014. Bilateral symmetry in ontogeny and regeneration of solitary Rugosa (Cnidaria; Paleozoic). Paleontological Journal, 48.11, 1183–1193.

Rubio-Portillo, E., Vzquez-Luis, M., Valle, C., Izquierdo-Muoz, A., and Ramos-Espl, A. A., 2014. Growth and bleaching of the coral Oculina patagonica under different environmental conditions in the western Mediterranean Sea. Marine Biology, 161.10, 2333–2343.

Schindelin, J., Arganda-Carreras, I., Frise, E., Kaynig, V., Longair, M., Pietzsch, T., Preibisch, S., Rueden, C., Saalfeld, S., Schmid, B., Tinevez, J.-Y., White, D. J., Hartenstein, V., Eliceiri, K., Tomancak, P., and Cardona, A., 2012. Fiji: an open-source platform for biological-image analysis. Nature Methods, 9.7, 676–682.

Schneider, C. A., Rasband, W. S., and Eliceiri, K. W., 2012. NIH Image to ImageJ: 25 years of image analysis. Nature Methods, 9.7, 671–675.

Scrutton, C. T., 1964. Periodicity in Devonian coral growth. Palaeontology, 7.4, 552–558.

Scrutton, C. T. Periodic Growth Features in Fossil Organisms and the Length of the Day and Month. In Brosche, P. D. P. and Sndermann, P. D. J., editors, Tidal Friction and the Earths Rotation. Springer Berlin Heidelberg, 1978.

Scrutton, C. T., 1996. Ecophenotypic variation in the early Silurian rugose coral *Palaeocyclus porpita*. Proceedings of the Yorkshire Geological and Polytechnic Society, 51.1, 1–8.

Scrutton, C. T., 1997. The Palaeozoic corals, I: origins and relationships. Proceedings of the Yorkshire Geological and Polytechnic Society, 51.3, 177–208.

Scrutton, C. T., 1998. The Palaeozoic corals, II: structure, variation and palaeoecology. Proceedings of the Yorkshire Geological and Polytechnic Society, 52.1, 1–57.

Sloss, L. L., editor. Sedimentary cover, North American Craton, U.S. Number v. D-2 in Geology of North America. Geological Society of America, Boulder, Colo, 1988.

Smith, S. V., 1978. Coral-reef area and the contributions of reefs to processes and resources of the world's oceans. Nature, 273.5659, .

Sorauf, J. E., 2001. External morphology and paleobiology of *Heliophyllum halli* (Zoantharia, Rugosa), from the Middle Devonian Hamilton Group of New York State. Journal of Pale-ontology, 75.1, 24–33.

Stanley, G. D. and Helmle, K. P., 2010. Middle Triassic coral growth bands and their implica-tion for photosymbiosis. PALAIOS, 25.12, 754–763.

Stauber, M. and Müller, R. Micro-Computed Tomography: A Method for the Non-Destructive Evaluation of the Three-Dimensional Structure of Biological Specimens. In Osteoporosis, Methods In Molecular Biology, pages 273–292. Humana Press, 2008.

Sun, D., Liu, Y., and Tan, M., 2002. Digital image analysis of palaeoenvironmental records and applications. Chinese Science Bulletin, 47.23, 1957–1963.

Sun, W., Romagnoli, J. A., Tringe, J. W., Letant, S. E., Stroeve, P., and Palazoglu, A., 2009. Line edge detection and characterization in SEM images using wavelets. IEEE Transac-tions on Semiconductor Manufacturing, 22.1, 180–187.

Szeliski, R., 2006. Image Alignment and Stitching: A Tutorial. Foundations and Trends in Computer Graphics and Vision, 2.1, 1–104.

Tanner, J. E., 1996. Seasonality and lunar periodicity in the reproduction of pocilloporid corals. Coral Reefs, 15.1, 59–66.

Tomasi, C. and Manduchi, R. Bilateral filtering for gray and color images. In Computer Vision, 1998. Sixth International Conference on, pages 839–846. IEEE, 1998.

Veron, J. C. E. N. Coral Taxonomy and Evolution. In Dubinsky, Z. and Stambler, N., editors, Coral Reefs: An Ecosystem in Transition, pages 37–45. Springer Netherlands, 2011.

Webb, G. E. and Yancey, T. E., 2010. Skeletal repair of extreme damage in rugose corals, Pella Formation (Mississippian, Iowa, USA). Palaeoworld, 19.34, 325–332.

Wells, J. W., 1963. Coral Growth and Geochronometry. Nature, 197948–950.

Winter, A. and Sammarco, P. W., 2010. Lunar banding in the scleractinian coral *Montastraea faveolata* : Fine-scale structure and influence of temperature. Journal of Geophysical Re-search, 115.G4, .

Wozniak, B. and Dera, J., 2007. Introduction: Absorption of Sunlight in the Ocean. Light Ab-sorption in Sea Water, pages 1–10.

Wright, J. D. and Wright, E. P., 1961. A Study of the Middle Devonian Widder Formation of Southwestern Ontario. Contributions from the Museum of Paleontology, The University of Michigan, 16.5, 287–300.

Yamaguchi, A. and Komuro, O., 2003. Characterization of Line Edge Roughness in Resist Patterns by Using Fourier Analysis and Auto-Correlation Function. Japanese Journal of Applied Physics, 42.6S, 3763–3770.

Yin, L., Yang, R., Gabbouj, M., and Neuvo, Y., 1996. Weighted median filters: a tutorial. IEEE Transactions on Circuits and Systems II: Analog and Digital Signal Processing, 43 .3, 157–192.

Young, G. A. and Kershaw, S., 2005. Classification and controls of internal banding in Palaeozoic stromatoporoids and colonial corals. Palaeontology, 48.3, 623–651.

Zhang, W., 2009. Daily and lunar growth features in Carboniferous and Devonian corals from Xinjiang: information about ancient Earths rotation and climate. Acta Geologica Sinica. Under revision.

Zhang, W., 2010. Discussion on physical meaning in our palaeontological research of coral fossils from Xinjiang. Acta Geologica Sinica. Under revision.

Appendix A

Additional Micro-CT scan information

A.1   Micro-CT scan parameters

kV = 125

uA = 110

Minimize rings mode

2 frames per projection

1 hr 40 minute scan

10 micron voxels

3141 projections

500 msec exposure

Tungsten reflection target

A.2   Micro-CT related software

Inspect X - capture software

CT Pro - volume reconstruction software

VG Studio Max 2.2 - initial visualization and export to 8bit dicom slices

GE Microview - Dicom visualization

ImageVis3D - three-dimensional rendering

Appendix B

Python Code

B.1   Image processing and line extraction

This script inputs longitudinal rugose coral slices and uses image processing and filtering to export a line in X-Y coordinate form, which represents the outer epithecal edge, for subsequent analysis.

```python
""" LineExtraction.py
Andrew Thomson, MSc. Geology thesis project, Western University

This script inputs longitudinal rugose coral slices and
uses image processing and filtering to export a line in X–Y
coordinate form, which represents the outer epithecal edge,
for subsequent analysis"""

import cv2
import numpy as np
import matplotlib.pyplot as plt
from matplotlib_scalebar.scalebar import ScaleBar, SI_LENGTH

def import_image(filename):
    """Import SEM image of study area.
    If image is sectioned, will have to run multiple times."""
    im = cv2.imread(str(filename), 0)
    h, w = im.shape[:2]
    return im, h, w


def fill_holes_binary_image(image):
    """Fill holes in binary image to create a solid cutout shape."""
```

```python
24        im_floodfill = image.copy()
25        mask = np.zeros((H + 2, W + 2), np.uint8)
26        cv2.floodFill(im_floodfill, mask, (0, 0), 255)
27        im_floodfill_inv = cv2.bitwise_not(im_floodfill)
28        im_holes_filled = image | im_floodfill_inv
29
30        im_list = [mask, im_floodfill, im_floodfill_inv, im_holes_filled]
31        im_list_names = ['mask', 'im_floodfill', 'im_floodfill_inv',
32                         'im_holes_filled']
33
34    # Display successive hole filling steps.
35        for i in range(len(im_list)):
36                display_fig(im_list[i], 'holes_filled_' +
37                            str(i).zfill(2) + '_' + im_list_names[i])
38
39        # Return solid cutout shape of coral body.
40      return im_holes_filled
41
42
43  def find_longest_contour(cnt):
44      """Get length of each countour detected in the image and return the
45      longest, outlining the largest shape in the image."""
46      longest_contour = 0
47      for i in range((len(cnt))):
48          if cv2.arcLength(cnt[i], True) > \
49                  cv2.arcLength(cnt[longest_contour], True):
50              longest_contour = i
51          else:
52              continue
53      return longest_contour
54
55
56  def remove_outer_boundary(image):
57      # remove rectangular image boundary coordinates
58      image[0, :] = 0
59      image[:, 0] = 0
60      image[0, :] = 0
61      image[:, 0] = 0
62      image[:, W - 1] = 0
63      image[H - 1, :] = 0
64      return image
65
66
```

```python
67  def write_cont_to_txt(cont, filename):
68      # write contour XY points to csv file
69      with open(folder + 'line_csv/' + specimen + '_' + file +
70                      '_data.csv', 'w+') as f:
71          f.write('x,y\n')
72          for i in range(len(cont[:])):
73              x = cont[:][i][0][0]
74              y = cont[:][i][0][1]
75              if 0 < x < (W-1):
76                  if 0 < y < (H-1):
77                      f.write('{0},{1}\n'.format(x, y))


80  def display_fig(figure, name):
81      # display and save figures
82      fig = plt.figure(frameon = False)
83      plt.imshow(figure, aspect = 'equal', cmap='gray_r')
84      plt.xticks([]), plt.yticks([])

86      # https://pypi.python.org/pypi/matplotlib-scalebar
87      # https://matplotlib.org/api/font_manager_api.html
88      scalebar = ScaleBar(1/scale, ' m ', SI_LENGTH,
89                          length_fraction = 0.1, color = "black",
90                          box_alpha = 0, location = scalebar_loc,
91                          border_pad = 2.0)

93      plt.gca().add_artist(scalebar)
94      plt.tight_layout(pad = 0)
95      plt.show()

97      # save figure to file
98      fig.savefig(folder + 'line_extraction/' + specimen + '_' +
99                  file + '-' + name + '.jpg', format = 'jpg',
100                 bbox_inches = 'tight', pad_inches = 0, dpi = 300)
101     plt.close()


104 # ==================================================
105 specimen = '_____'
106 folder = '_____' + specimen + '/'
107 file = '_____'
108 fmt = '_____'
109 scalebar_loc = 'upper left'
```

```
110  file = "_____" # image section filename
111
112  # image scale taken from specimen SEM images
113  # c scale = 2.380 pixels / micron
114  # e scale = 3.989 pixels / micron
115  scale = 3.989    # image scale in pixels per micron
116
117  # =====================================
118  # Import study area image – tif for analysis , compressed jpg to reduce
         output image file size
119  print('line extraction: ' + specimen + '_' + file)
120  im, H, W = import_image(folder + 'sections/' + file + fmt)
121  im_ut , _, _ = import_image(folder + 'sections/' + file + '.jpg')
122
123  # =====================================
124  # use CLAHE to normalize contrast
125  # http://docs.opencv.org/3.1.0/d5/daf/
126  # tutorial_py_histogram_equalization.html
127  clahe = cv2.createCLAHE(clipLimit = 5, tileGridSize = (80, 80))
128  im_clahe = clahe.apply(im)
129
130  # =====================================
131  # plot histogram of image
132  hist = cv2.calcHist([im],[0],None,[256],[0,256])
133  plt.hist(im.ravel(),256,[0,256]); plt.show()
134
135  # =====================================
136  # apply bilateral filter to imported image
137  # http://docs.opencv.org/3.0-beta/modules/imgproc/doc/filtering.html
138  im_clahe_bilat = cv2.bilateralFilter(im_clahe, 9, 100, 50)
139
140  # =====================================
141  # threshold to convert to binary
142  # http://docs.opencv.org/3.0-beta/doc/py_tutorials/py_imgproc
143  # /py_thresholding/py_thresholding.html
144  ret , im_clahe_bilat_otsu = cv2.threshold(
145                     im_clahe_bilat , 0, 255,
146                     cv2.THRESH_BINARY + cv2.THRESH_OTSU)
147
148  # =====================================
149  # fill holes in binary image
150  im_clahe_bilat_otsu_fill = fill_holes_binary_image(
151                     im_clahe_bilat_otsu)
```

```python
152
153  # ========================================
154  # find and draw contours
155  im_cutout = np.zeros_like(im)
156  im_cutout_all = np.zeros_like(im)
157  im_line = np.zeros_like(im)
158  im_cutout_med = np.zeros_like(im)
159
160  _, original_im_contours, _ = cv2.findContours(
161                  im_clahe_bilat_otsu_fill,
162                  cv2.RETR_LIST, cv2.CHAIN_APPROX_NONE)
163
164  coral_cutout = find_longest_contour(original_im_contours)
165
166  cv2.drawContours(im_cutout, original_im_contours, coral_cutout,
167          (255, 255, 255), thickness = cv2.FILLED)
168
169  cv2.drawContours(im_cutout_all, original_im_contours, -1,
170          (255, 255, 255), thickness = cv2.FILLED)
171
172  # median filter main coral body cutout
173  im_clahe_bilat_otsu_fill_med = cv2.medianBlur(im_cutout, 27)
174
175  # contour previous image to extract new edge line
176  _, cutout_median_contours, _ = cv2.findContours(
177                  im_clahe_bilat_otsu_fill_med,
178                  cv2.RETR_LIST, cv2.CHAIN_APPROX_NONE)
179
180  # get length of image contour and save to file
181  coral_outline = find_longest_contour(cutout_median_contours)
182
183  length_w_borders = cv2.arcLength(cutout_median_contours
184                  [coral_outline], True)
185  print(length_w_borders)
186
187  with open(folder + 'line_lengths/' + specimen + '_' +
188          file + '_data.csv', 'w+') as f:
189    f.write(str("L: " + str(length_w_borders) +
190          " H: " + str(H) + " W: " + str(W)))
191
192  # draw extracted line
193  cv2.drawContours(im_line, cutout_median_contours, coral_outline,
194          (255, 255, 255), thickness = 10)
```

```python
195
196  cv2.drawContours(im_cutout_med, cutout_median_contours, -1,
197          (255, 255, 255), thickness = cv2.FILLED)
198
199  cv2.drawContours(im, cutout_median_contours, coral_outline,
200          (255, 255, 255), thickness = 10)
201
202  cont = (cutout_median_contours[coral_outline])
203
204  #remove rectangular bounding points
205  ext_line = remove_outer_boundary(im_line)
206  im_ext_line = remove_outer_boundary(im)
207
208  # save contour xy coordinates to text file
209  write_cont_to_txt(cont, file)
210
211  # save images
212  im_list = [im_ut, im_clahe, im_clahe_bilat, im_clahe_bilat_otsu,
213          im_clahe_bilat_otsu_fill, im_cutout,
214          im_clahe_bilat_otsu_fill_med, im_cutout_med,
215          ext_line, im_ext_line]
216
217  im_list_names = ['im_UT', 'im_clahe', 'im_clahe_bilat',
218          'im_clahe_bilat_otsu',
219          'im_clahe_bilat_otsu_fill', 'im_cutout',
220          'im_clahe_bilat_otsu_fill_med',
221          'im_cutout_med', 'ext_line', 'im_ext_line']
222
223  for i in range(len(im_list)):
224    display_fig(im_list[i], str(i).zfill(2) + '_' + im_list_names[i])
225    plt.close()
```

B.2   Peak detection and ridge identification

This script inputs a previously extracted rugose coral epithecal edge line (X-Y coordinates in .csv format) to detect local extrema using Continuous Wavelet Transformation peak detection in order to identify growth intervals. Adjacent trough-peak-trough pairs are grouped into triangles, representing simplified growth ridges. This allows for basic geometric analysis to ba applied in an attempt to quantify changes in coral growth rate. All geometric measurements and statistical analysis (mean, standard deviation) are exported to .csv files. An attempt has been made to detect patterns and isolate larger groupings of ridges, though it ultimately proved unsuccessful due to data quality.

```python
1  """ PeakDetection.py
2  Andrew Thomson, MSc. Geology thesis project, Western University
3
4  This script inputs a previously extracted rugose coral epithecal edge line
       (X-Y coordinates in .csv format) to detect local extrema using
       Continuous Wavelet Transformation peak detection in order to identify
       growth intervals. Adjacent trough-peak-trough pairs are grouped into
       triangles, representing simplified growth ridges. This allows for basic
        geometric analysis to ba applied in an attempt to quantify changes in
       coral growth rate. An attempt has been made to detect patterns and
       isolate larger groupings of ridges, though it ultimately proved
       unsuccessful due to data quality. """
5
6  import numpy as np
7  import matplotlib.pyplot as plt
8  import scipy.signal as sig
9  from math import sqrt, acos, degrees
10 from matplotlib_scalebar.scalebar import ScaleBar, SI_LENGTH
11
12 def peak_detect(dat):
13     win_min = 15  # minimum expected width of peaks of interest
14     win_max = 100  # maximum expected width of peaks of interest
15     widths = np.arange(win_min, win_max)
16
17     return sig.find_peaks_cwt(dat, widths,
18                               min_length = None,
19                               # default cwt.shape[0]/4: 1/4 len(widths)
20                               noise_perc = 80,  # default: 10
```

```python
                                    max_distances = (widths/4),
                                    # default: 1/4 widths
                                    gap_thresh=None,   # default: 2
                                    wavelet=None,
                                    )
def peak_detect_large(dat):
    win_min = 2    # minimum expected width of peaks of interest
    win_max = 50 # maximum expected width of peaks of interest
    widths = np.arange(win_min, win_max)

    ext = sig.find_peaks_cwt(dat, widths,
                                    min_length = 3,
                                    # default: 1/4 len(widths)
                                    noise_perc = 10,   # default: 10
                                    max_distances = (widths/2),
                                    # default: 1/4 widths
                                    gap_thresh = None,   # default: 2
                                    wavelet = None,
                                    )
    return ext, dat[ext]


def log_triangles(t, p):
    ridges = []
    peak_no = 0
    trough_no = 0

    while trough_no < (len(t)) and peak_no < (len(p)):
            if trough_no < len(t) - 1 \
                    and p[peak_no] > t[trough_no + 1]:
                trough_no += 1

            if p[peak_no] < t[trough_no]:
                peak_no += 1

            if peak_no < len(p) - 1 \
                    and trough_no < len(t) - 1 \
                    and p[peak_no + 1] < t[trough_no+1]:
                peak_no += 1

            # if data[t[trough_no+1], 0] > data[p[peak_no], 0]:
            #     trough_no += 1

            else:
```

```
64                        ridges.append([t[trough_no],
65                                       p[peak_no],
66                                       t[trough_no + 1]])
67                    peak_no += 1
68                    trough_no += 1
69
70        return ridges
71
72
73  def tri_area(data, tri_list):
74      tri_data = []
75      for i in range(len(tri_list)):
76          one = (data[tri_list[i][0]])   # trough
77          two = (data[tri_list[i][1]])   # peak
78          three = (data[tri_list[i][2]])   # trough
79
80          cent = [(one[0] + two[0] + three[0]) / 3,
81                  (one[1] + two[1] + three[1]) / 3]
82
83          a = sqrt(((one[0] - two[0]) ** 2) + ((one[1] - two[1]) ** 2))
84          b = sqrt(((one[0] - three[0]) ** 2) + ((one[1] - three[1]) ** 2))
85          c = sqrt(((two[0] - three[0]) ** 2) + ((two[1] - three[1]) ** 2))
86
87          alpha = degrees(acos((b**2 + c**2 - a**2) / (2 * b * c)))
88          beta = degrees(acos((c ** 2 + a ** 2 - b ** 2) / (2 * c * a)))
89          gamma = degrees(acos((a**2 + b**2 - c**2) / (2 * a * b)))
90
91          # find area of a triangle with 3 known points.
92          area = abs(((one[0] * (two[1] - three[1])) +
93                     (two[0] * (three[1] - one[1])) +
94                     (three[0] * (one[1] - two[1])))/2)
95
96      a /= im_scale
97          b /= im_scale
98          c /= im_scale
99          area /= im_scale ** 2
100         if area >= exc_area:
101             tri_data.append([area, cent,
102                             (one, two, three),
103                             (a, b, c),
104                             (alpha, beta, gamma)])
105
106     return tri_data
```

```python
107
108
109  def write_tri_data_to_csv(tridata, file):
110      id = 0
111      with open(folder + 'tri_data/' + specimen + '_' + file +
112                '_tri_data''.csv', 'w+') as f:
113
114          f.write('id, area, centX, centY, ptA_x, ptA_y, ptB_x, ptB_y,'
115                  'ptC_x, ptC_y, sla, slb, slc, alpha, beta, gamma, ptD_x,
        ptD_y, height, hw_rat\n')
116
117          for i in range(len(tridata)):
118              area = tridata[i][0]
119
120              cent_x, cent_y = tridata[i][1]
121
122              pt_a_x, pt_a_y = tridata[i][2][0]
123              pt_b_x, pt_b_y = tridata[i][2][1]
124              pt_c_x, pt_c_y = tridata[i][2][2]
125
126              cent_x = int(round(cent_x))
127              cent_y = int(round(cent_y))
128              pt_a_x = int(round(pt_a_x))
129              pt_a_y = int(round(pt_a_y))
130              pt_b_x = int(round(pt_b_x))
131              pt_b_y = int(round(pt_b_y))
132              pt_c_x = int(round(pt_c_x))
133              pt_c_y = int(round(pt_c_y))
134
135              pt_dx = int(round(tridata[i][5][0]))
136              pt_dy = int(round(tridata[i][5][1]))
137
138              sl_a = tridata[i][3][0]
139              sl_b = tridata[i][3][1]
140              sl_c = tridata[i][3][2]
141
142              height = tridata[i][6]
143
144              alpha = tridata[i][4][0]
145              beta = tridata[i][4][1]
146              gamma = tridata[i][4][2]
147
148              hw_ratio = height / sl_b
```

```
149
150                 f.write('{0},{1},{2},{3},{4},{5},{6},{7},{8},'
151                         '{9},{10},{11},{12},{13},{14},{15},{16},{17},{18},{19}\
     n'
152                         .format(specimen + file + "_" + str(id), round(area, 2)
     , cent_x, cent_y,
153                                  pt_a_x, pt_a_y, pt_b_x, pt_b_y, pt_c_x, pt_c_y,
      round(sl_a, 2),
154                                  round(sl_b, 2), round(sl_c, 2), round(alpha, 2)
     , round(beta, 2),
155                                  round(gamma, 2), pt_dx, pt_dy, round(height, 2)
     , round(hw_ratio, 4)))
156                 id += 1
157         f.close()
158
159 def display_triangles():
160     id = 0
161     for i in range(len(tri_geom)):
162         area = tri_geom[i][0]
163         centroid = tri_geom[i][1]
164         pts = tri_geom[i][2]
165         side_lengths = tri_geom[i][3]
166         deg = tri_geom[i][4]
167
168         if area >= exc_area:
169             t1 = plt.Polygon(tri_geom[i][2],
170                                 closed = True, facecolor = 'orange')
171             t1.set_alpha(0.6)
172
173             if i % 2 == 0:
174                 plt.annotate(id, centroid,
175                 xytext = (centroid[0], centroid[1]+250),
176                 fontsize=16,
177                 arrowprops = dict(facecolor = 'black',
178                             width = 1,
179                             headlength = 1,
180                             headwidth = 1,),)
181
182             else:
183                 plt.annotate(id, centroid,
184                 xytext = (centroid[0], centroid[1]-250),
185                 fontsize=16,
186                 arrowprops = dict(facecolor = 'black',
```

```
187                                    width = 1,
188                                    headlength = 1,
189                                    headwidth = 1,),)
190                plt.gca().add_patch(t1)
191
192                # print triangle geometric properties to console
193                print("Triangle # ", id)
194                print("Area: ", round(area, 2), " m ")
195                print("Vertices: ", "A =", pts[0],
196                        "B =", pts[1], "C =", pts[2])
197                print("Lengths: ",
198                        "a =", (side_lengths[0]/im_scale), " m ,",
199                        "b =", (side_lengths[1]/im_scale), " m ,",
200                        "c =", (side_lengths[2]/im_scale), " m ")
201                print("Angles: ", u"\u03B1 =", deg[0],
202                                   u"\u03B2 =", deg[1],
203                                   u"\u03B3 =", deg[2])
204                print()
205
206                plt.plot((centroid[0], pts[1][0]),
207                          (centroid[1], pts[1][1]),
208                          color='g')
209                id += 1
210
211     plt.plot(data[:, 0][troughs], data[:, 1][troughs],
212              marker = '.', markersize = 6,
213              linestyle = 'None', color = 'blue')
214
215     plt.plot(data[:, 0][peaks], data[:, 1][peaks],
216              marker = '.', markersize = 6,
217              linestyle = 'None', color = 'red')
218
219 def write_trough_data_to_csv(tridata, file):
220     i = 0
221     with open(folder + 'extrema_data/' + specimen + '_' + file +
222              '_trough_data''.csv', 'w+') as f:
223
224         f.write('trough_x, trough_y\n')
225         while i < (len(tridata) - 1):
226         #for i in range(len(tridata)):
227             pt_a_x, pt_a_y = tridata[i][2][0]
228             pt_c_x, pt_c_y = tridata[i][2][2]
229             pt_a2_x, pt_a2_y = tridata[i+1][2][0]
```

```
230
231                    i += 1
232                    if pt_a2_x == pt_c_x and pt_a2_y == pt_c_y:
233                        f.write('{0},{1}\n'.format(pt_a_x, pt_a_y))
234                        continue
235
236                    else:
237                        f.write('{0},{1}\n'.format(pt_a_x, pt_a_y))
238                        f.write('{0},{1}\n'.format(pt_c_x, pt_c_y))
239
240            pt_a2_x, pt_a2_y = tridata[-1][2][0]
241            pt_c2_x, pt_c2_y = tridata[-1][2][2]
242
243            f.write('{0},{1}\n'.format(pt_a2_x, pt_a2_y))
244            f.write('{0},{1}\n'.format(pt_c2_x, pt_c2_y))
245
246            f.close()
247
248  def write_peak_data_to_csv(tridata, file):
249      with open(folder + 'extrema_data/' + specimen + '_' + file +
250                '_peak_data''.csv', 'w+') as f:
251
252          f.write('peak_x, peak_y\n')
253
254          for i in range(len(tridata)):
255              pt_b_x, pt_b_y = tridata[i][2][1]
256
257              f.write('{0},{1}\n'.format(pt_b_x, pt_b_y))
258          f.close()
259
260  def stats_analysis(tridata, file):
261      list_area = []
262      list_sla = []
263      list_slb = []
264      list_slc = []
265      list_height = []
266      list_alpha = []
267      list_beta = []
268      list_gamma = []
269      list_hw_ratio = []
270      trough_line_length = 0
271      peak_line_length = 0
272
```

```python
273    trough_data = np.loadtxt((folder + 'extrema_data/' + specimen +
274                              '_' + file + '_trough_data.csv'),
275                             delimiter = ',', usecols = (0, 1),
276                             skiprows = 1, dtype = int)

278    peak_data = np.loadtxt((folder + 'extrema_data/' + specimen +
279                           '_' + file + '_peak_data.csv'),
280                          delimiter = ',', usecols = (0, 1),
281                          skiprows = 1, dtype = int)

283    for i in range(len(tridata)):
284        list_area.append(tridata[i][0])

286        list_sla.append(tridata[i][3][0])
287        list_slb.append(tridata[i][3][1])
288        list_slc.append(tridata[i][3][2])

290        list_height.append(tridata[i][6])

292        list_alpha.append(tridata[i][4][0])
293        list_beta.append(tridata[i][4][1])
294        list_gamma.append(tridata[i][4][2])

296        list_hw_ratio.append(tridata[i][7])

298    avg_area = np.mean(list_area)
299    sd_area = np.std(list_area)

301    avg_sla = np.mean(list_sla)
302    sd_sla = np.std(list_sla)
303    avg_slb = np.mean(list_slb)
304    sd_slb = np.std(list_slb)
305    avg_slc = np.mean(list_slc)
306    sd_slc = np.std(list_slc)

308    avg_height = np.mean(list_height)
309    sd_height = np.std(list_height)

311    avg_alpha = np.mean(list_alpha)
312    sd_alpha = np.std(list_alpha)
313    avg_beta = np.mean(list_beta)
314    sd_beta = np.std(list_beta)
315    avg_gamma = np.mean(list_gamma)
```

```python
316        sd_gamma = np.std(list_gamma)

317

318        avg_hw_ratio = np.mean(list_hw_ratio)
319        sd_hw_ratio = np.std(list_hw_ratio)

320

321        ridge_cnt = len(tridata)

322

323        j = 0
324        while j < (len(trough_data[:, 0]) - 1):
325            a = sqrt(
326                ((trough_data[j][0] - trough_data[j + 1][0]) ** 2) + ((
    trough_data[j][1] - trough_data[j + 1][1]) ** 2))
327            a /= im_scale
328            # print('Trough line ' + str(trough_data[j]) + str(trough_data[j +
    1]) + ": " + str(a) + "  m")
329            trough_line_length += a
330            j += 1
331        # print("Total trough length " + specimen + "_" + file + ": " + str(
    trough_line_length) + "  m")

332

333        k = 0
334        while k < (len(peak_data[:, 0]) - 1):
335            a = sqrt(
336                ((peak_data[k][0] - peak_data[k + 1][0]) ** 2) + ((peak_data[k
    ][1] - peak_data[k + 1][1]) ** 2))
337            a /= im_scale
338            # print('Peak line ' + str(peak_data[k]) + str(peak_data[k + 1]) +
    ": " + str(a) + "  m")
339            peak_line_length += a
340            k += 1
341        # print("Total peak length " + specimen + "_" + file + ": " + str(
    peak_line_length) + "  m")

342

343        tr_len = trough_line_length
344        pk_len = peak_line_length

345

346        with open(folder + 'stats_analysis/' + specimen + '_' + file +
347                  '_stats''.csv', 'w+') as f:

348

349            f.write('sample, ridges, tr_len, pk_len, area_avg, area_SD, sla_avg
    , sla_SD, slb_avg, slb_SD, slc_avg, slc_SD, '
350                    'height_avg,'
```

```
351                        'height_SD, alpha_avg, alpha_SD, beta_avg, beta_SD,
         gamma_avg, gamma_SD, hw_avg, hw_SD\n')
352
353          f.write('{0},{1},{2},{3},{4},{5},{6},{7},{8},'
354                       '
         {9},{10},{11},{12},{13},{14},{15},{16},{17},{18},{19},{20},{21}\n'
355                       .format(specimen + file, ridge_cnt, round(tr_len, 2), round
         (pk_len, 2), round(avg_area, 2),
356                                 round(sd_area, 2),
357                                 round(avg_sla, 2), round(sd_sla, 2), round(avg_slb,
          2),
358                                 round(sd_slb, 2), round(avg_slc, 2), round(sd_slc,
         2),
359                                 round(avg_height, 2), round(sd_height, 2), round(
         avg_alpha, 2),
360                                 round(sd_alpha, 2), round(avg_beta, 2), round(
         sd_beta, 2),
361                                 round(avg_gamma, 2), round(sd_gamma, 2),
362                                 round(avg_hw_ratio, 4), round(sd_hw_ratio, 4)))
363      f.close()
364
365
366 def write_groups_to_csv(large_extrema, file):
367     with open(folder + 'groups/' + specimen + '_' + file
368         + '_group_pts''.csv', 'w+') as g:
369         g.write('id, X, Y\n')
370
371         for i in range(len(large_extrema)):
372             id = large_extrema[i]
373             x = data[:, 0][large_extrema][i]
374             y = data[:, 1][large_extrema][i]
375
376             g.write('{0},{1},{2}\n'.format(id, x, y))
377             id += 1
378
379 def display_fig(save_path):
380     #  display and save figures
381
382     # https://pypi.python.org/pypi/matplotlib-scalebar
383     # https://matplotlib.org/api/font_manager_api.html
384     scalebar = ScaleBar(1 / im_scale, ' m', SI_LENGTH,
385                         length_fraction = 0.1, color = "black",
386                         box_alpha = 0, location = scalebar_loc,
```

```
387                              border_pad = 2.0)
388
389     plt.gca().add_artist(scalebar)
390     plt.annotate(specimen + '_' + file, (40, h - 100),
391         color = 'black', fontsize = 18)
392     plt.xticks([]), plt.yticks([])
393     plt.tight_layout(pad = 0)
394     plt.show()
395
396     # save figure to file
397     fig.savefig(save_path, bbox_inches = 'tight',
398         pad_inches = 0, dpi = 300)
399
400 #======================================================================
401 specimen = '_____'
402 folder = '_____' + specimen + '/'
403 file = '_____'
404 fmt = '_____'
405
406 # image scale taken from specimen SEM images
407 # c scale = 2.380 pixels / micron
408 # e scale = 3.989 pixels / micron
409 scale = 3.989   # image scale in pixels per micron
410
411 # =====================================
412 # load csv file
413 data = np.loadtxt((folder + 'line_csv/' + specimen +
414         '_' + file + '_data.csv'),
415         delimiter = ',', usecols = (0, 1),
416         skiprows = 1, dtype = int)
417
418 # =====================================
419 exc_area = 25  # area limit to exclude clearly false ridges, in   m
420 scalebar_loc = 'upper right'
421
422 print('peak detection: ' + specimen + '_' + file)
423
424 data = np.loadtxt((folder + 'line_csv/' + specimen +
425         '_' + file + '_data.csv'),
426         delimiter = ',', usecols = (0, 1),
427         skiprows = 1, dtype = int)
428
429 troughs = peak_detect(data[:, 1])
```

```
430  peaks = peak_detect((data[:, 1] * −1))
431
432  # attempted large scale bundle detection
433  bundle_troughs, y1_vals = peak_detect_large(data[:, 1][troughs])
434  bundle_peaks, y2_vals = peak_detect_large((data[:, 1][troughs])*−1)
435  large_extrema = np.concatenate((bundle_peaks, bundle_troughs))
436  large_extrema = np.sort(large_extrema)
437
438  write_groups_to_csv(bundle_troughs, file)
439
440  # process detected triangles and export to .csv
441  tri_list = log_triangles(troughs, peaks)
442  tri_geom = tri_area(data, tri_list)
443  write_tri_data_to_csv(tri_geom, file)
444  write_groups_to_csv(bundle_troughs, file)
445  write_peak_data_to_csv(tri_geom, file)
446  write_trough_data_to_csv(tri_geom, file)
447  write_tri_data_to_csv(tri_geom, file)
448  stats_analysis(tri_geom, file)
449
450
451  fig = plt.figure(frameon = False)
452  im = plt.imread(folder + 'sections/' + file + '_inv.jpg')
453  h, w = im.shape[:2]
454  plt.imshow(im, cmap = 'gray')
455
456  plt.plot(data[:, 0][troughs], data[:, 1][troughs],
457      marker = '.', markersize = 6,
458      linestyle = 'None', color = 'red')
459
460  plt.plot(data[:, 0][peaks], data[:, 1][peaks],
461      marker = '.', markersize = 6,
462      linestyle = 'None', color = 'blue')
463
464  # save figure to file
465  save_path = str(folder + 'extrema/' + specimen
466      + '_' + file + '_extrema' + '.jpg')
467  display_fig(save_path)
468
469  fig = plt.figure(frameon = False)
470  plt.imshow(im, cmap = 'gray')
471  display_triangles()
472
```

```python
473  # save figure to file
474  save_path = str(folder + 'extracted_triangles/' + specimen
475          + '_' + file + '_triangles' + '.jpg')
476  display_fig(save_path)
477
478  # divide ridges into larger bundles
479  # draw large scale extrema as vertical dashed lines
480
481  fig = plt.figure(frameon = False)
482  plt.imshow(im, cmap = 'gray')
483  display_triangles()
484
485  for i in range(0, len(bundle_troughs)):
486    mark_x = [(data[:, 0][troughs][bundle_troughs][i])
487          ,(data[:, 0][troughs][bundle_troughs][i])]
488    mark_y = [0, h-1]
489    plt.plot(mark_x, mark_y,
490        marker = 'None', color = 'green',
491        linestyle = '--', linewidth = 3)
492
493  for i in range(0, len(bundle_peaks)):
494      mark_x2 = [(data[:, 0][troughs][bundle_peaks][i])
495          ,(data[:, 0][troughs][bundle_peaks][i])]
496      mark_y2 = [0, h-1]
497      plt.plot(mark_x2, mark_y2,
498              marker = 'None', color = 'purple',
499        linestyle = '--', linewidth = 3)
500
501  # save figure to file
502  save_path = str(folder + 'bundle_detect/' + specimen
503          + '_' + file + '_bundles' + '.jpg')
504  display_fig(save_path)
505  plt.close()
```

Curriculum Vitae

Name: Andrew Thomson

Post-Secondary   The University of Western Ontario
Education and   London, Canada
Degrees: 2009 - 2014 BSc. Specialization in Geology (4 yr)

           The University of Western Ontario
           London, Canada
           2014 - Present MSc. Geology

Honours and   3rd Place, Imperial Barrel Award, Canada Region
Awards: 2015

           Dean's Honor List
           2012 - 2014

           Robert and Ruth Lumsden Scholarship in Science
           2013

Related Work   Teaching Assistant
Experience: The University of Western Ontario
           2014 - 2016